FACULTY
OF MATHEMATICS
AND PHYSICS
Charles University

DOCTORAL THESIS

Daniel Staško

Crystallographic and electronic properties of rare-earth $A_2B_2O_7$ oxides under extreme conditions

Department of Condensed Matter Physics

Supervisor of the doctoral thesis: RNDr. Milan Klicpera, Ph.D.
Study programme: Physics of Condensed Matter and Materials Research
Study branch: P4F3

Prague 2024

I declare that I carried out this doctoral thesis independently, and only with the cited sources, literature and other professional sources. It has not been used to obtain another or the same degree.

I understand that my work relates to the rights and obligations under the Act No. 121/2000 Sb., the Copyright Act, as amended, in particular the fact that the Charles University has the right to conclude a license agreement on the use of this work as a school work pursuant to Section 60 paragraph 1 of the Copyright Act.

In .... date ....

Author's signature

Here, I would like to thank all the people who supported me during my doctoral studies, which led to the creation of this surely very beautiful thesis.

The biggest gratitude goes to my supervisor RNDr. Milan Klicpera, Ph.D., who has always actively guided me throughout these years and has been my personal scientific role model.

I thank all of the colleagues who helped me with measurements and taught me how to measure, analyse, and understand what I have been doing here. Namely: doc. RNDr. Jiří Prchal, Ph.D. for helping me perform high-pressure experiments safely, which led to zero explosions during my experiments; Dr. Ross H. Colman and RNDr. Andrej Kancko for performing a synchrotron experiment in the UK without me when I mistakenly thought I did not have a valid passport; Mgr. Petr Proschek for helping me with measurements in the Troja labs in exchange for occasionally closing a valve on the 20 T cryomagnet on Sundays; and many others.

I thank all the people who helped me think about things other than the present work. Namely, my two M.B. friends, the tabletop game club, my volleyball group, my lazy DnD group, and the "student lunch break" group (Jirka, Andrej, Petr, Petr, Petr, Andrej, Tereza, Eliška, and Karol).

Finally, I would like to thank my family for supporting me despite the fact that I moved so far away from home. I dedicate this work to my two cute godchildren, Amélia and Charlotte.

Title: Crystallographic and electronic properties of rare-earth $A_2B_2O_7$ oxides under extreme conditions

Author: Daniel Staško

Department: Department of Condensed Matter Physics

Supervisor: RNDr. Milan Klicpera, Ph.D., Department of Condensed Matter Physics

Abstract: This work presents a systemic study of rare-earth $A_2B_2O_7$ oxides, focussing on the B = Ir iridate series. The structural, electrical transport, and magnetic properties of most $A_2Ir_2O_7$ iridates were investigated under extreme conditions, namely down to low temperatures, up to high magnetic fields, and under high external pressure. Both polycrystalline and single-crystalline samples were synthesised and characterised. Presented synchrotron study of the compressibility of the pyrochlore structure, stable at temperatures down to 4 K, at pressures of up to 20 GPa and with A substitution, pave the way for understanding the electronic and magnetic properties of $A_2Ir_2O_7$ iridates. The magnetic phase transition and concomitant semiconductor-insulator transition were followed in the heavy-rare-earth part of the series. Importantly, the nature of the semiconductor-insulator transition is ascribed to the Slater-type mechanism (opening of the insulating gap due to the antiferromagnetic ordering of magnetic moments) without Brillouin-zone folding, based on the electrical resistivity and magnetisation data. Applied external pressure enhances both the insulating and antiferromagnetic phases, as demonstrated for the $Lu_2Ir_2O_7$ end-member. Magnetic properties of these materials are shown to be strongly dependent on the antiferromagnetic domain structure, especially on the small ferromagnetic component pinned at the domains' interfaces. Theoretical calculations predicting the dimensions of the domains were performed.

Keywords: $A_2B_2O_7$ oxides, pyrochlore structure, metal-insulator transition, domain walls

Název: Krystalografické a elektronové vlastnosti vzácnozeminných $A_2B_2O_7$ oxidů v extrémních podmínkách

Autor: Daniel Staško

Katedra: Katedra fyziky kondenzovaných látek

Vedoucí dizertační práce: RNDr. Milan Klicpera, Ph.D., Katedra fyziky kondenzovaných látek

Abstrakt: Táto práca prezentuje systematickú štúdiu vzácnozeminných $A_2B_2O_7$ oxidov, sústrediac sa na sériu B = Ir iridátov. Štruktúrne, elektro-transportné a magnetické vlastnosti väčšiny $A_2Ir_2O_7$ iridátov boli skúmané v extrémnych podmienkach, menovite v nízkych teplotách, vo vysokých magnetických poliach, a pod vysokým externým tlakom. Polykryštalické aj monokryštalické vzorky boli syntetizované a charakterizované. Prezentovaná synchrotronová štúdia stlačiteľnosti pyrochlórovej štruktúry, stabilnej v teplotách dolu do 4 K, v tlakoch do 20 GPa, a so substitúciou A, vydláždʼujú cestu pre pochopenie elektrónových a magnetických vlastností $A_2Ir_2O_7$ iridátov. Magnetický fázový prechod a pridružený prechod polovodič-izolátor boli pozorované v ťažkovzácnozeminnej časti série. Charakter prechodu je pripísaný mechanizmu Slaterovho typu (tvorba gapu kvôli antiferromagnetickému usporiadaniu magnetických momentov) bez skladania Brillouinovej zóny, na základe dát elektrického odporu a magnetizácie. Aplikácia externého tlaku zosilňuje izolujúcu aj antiferromagnetickú fázu, čo je demonštrované na $Lu_2Ir_2O_7$. Je ukázané, že magnetické vlastnosti týchto materiálov sú vysoko závislé na antiferromagnetickej doménovej štruktúre, teda hlavne na malej ferromagnetickej komponente zaseknutej na hraniciach domén. Teoretické výpočty predpovedajú veľkosti magnetických domén.

Klíčová slova: $A_2B_2O_7$ oxidy, pyrochlórová štruktúra, prechod kov-izolátor, doménové steny

Contents

Introduction

$A_2B_2O_7$ oxides, where A is a rare-earth element and B stands for a 4*d* or 5*d* transition metal, have been an attractive subject for the condensed matter community due to their frequently complex ground states, including spin-liquid states [1] or spin-ice with magnetic monopole-like states [2]. Most of $A_2B_2O_7$ oxides crystallise in the ordered cubic structure of the pyrochlore-type with A^{3+} and B^{4+} ions forming two independent interpenetrating sublattices of corner-sharing tetrahedra [3,4]. The pyrochlore crystal lattice therefore promotes a 3D geometrical frustration of magnetic moments of magnetic A^{3+} or/and B^{4+} cations. Simultaneously, the cations are surrounded by deformed cubic and octahedral cages of oxygen anions, respectively, mediating the magnetic interactions and creating the crystal field acting on magnetic cations.

Among the B elements, the 5*d* transition metal B = Ir presents an intriguing case. Strong relativistic spin-orbit coupling and electron correlations of similar strength in this 5*d* element bring forth complex electronic and conducting states, including e.g., Weyl semimetal [5], topological insulator [6], axion insulator [7], or topological Mott insulator [8]. In addition, the Ir sublattice impacts the magnetic A sublattice and vice versa through the molecular field or *d-f* exchange, leading to, e.g., Ir-sublattice-induced magnetic ordering of rare-earth sublattice [9,10]. All in all, a confluence of a strong SOC, comparably strong electron correlations, *d-f* exchange between Ir^{4+} and A^{3+} moments, crystal field effects, and exchange magnetic interactions on a geometrically frustrated lattice lead to many predicted and reported novel phenomena (dozens of recent publications).

The present work focuses on the structural, transport, and magnetic properties of the rare-earth $A_2Ir_2O_7$ iridates, in both polycrystalline and single crystalline forms. In addition to the systematics within the whole rare-earth series, the main experimental interest is aimed at the heavy-rare-earth members (A = Dy – Lu), which have been understudied compared to the light-rare-earth part of the series. Measurements at low temperatures and in high magnetic fields are enriched by the application of high external pressure in selected cases. For the interpretation of magnetic and conductive properties under pressure, the structural properties of $A_2Ir_2O_7$ are investigated by employing multiple synchrotron radiation experiments. The nature of the semiconductor-insulator transition is studied and discussed in the framework of the Mott and Slater models. Finally, the magnetic properties of selected single crystals are revealed. A robust ferromagnetic component in the antiferromagnetically ordered iridates is interpreted within the domain wall model.

The presented study consists of:

1. A theoretical section focused on electron and magnetic properties of geometrically frustrated pyrochlore $A_2Ir_2O_7$, physics of metal-insulator transition, and materials' compressibility.
2. An experimental section overviewing the apparatus and techniques employed for sample synthesis and investigation (X-ray and synchrotron diffraction, electron

microscopy, electrical resistivity, heat capacity, magnetisation, AC magnetic susceptibility, and high-pressure techniques).
3. An overview of the previous results on $A_2B_2O_7$ oxides and especially $A_2Ir_2O_7$ iridates most relevant to the present study.
4. A section encompassing the main results of this study, spanning from synthesis and basic characterisation to the stability of the crystal structure in extreme conditions, the evolution of low-temperature transport and magnetic properties, and the model of antiferromagnetic domains and ferromagnetic domain interfaces.
5. A discussion connecting the individual results into a comprehensive overview of the rare-earth $A_2Ir_2O_7$ series, accompanied by the prospects for future investigations of the $A_2Ir_2O_7$ and related series.
6. A summary of the most important conclusions.

For the sake of consistency, we limited the present thesis to the investigation of only $A_2Ir_2O_7$ iridates. In addition to the presented work, much effort was also invested in the study of rare-earth $A_2Zr_2O_7$ zirconates during the doctoral journey of the author. Most of the results have been published in impacted scientific journals. All eight published articles connected to $A_2B_2O_7$ compounds authored and co-authored by the applicant are listed at the end of this thesis.

1. Theoretical background

1.1 Magnetic properties of rare-earth A^{3+} ions

The atoms' magnetism is dictated by the electron configuration, characterised mainly by orbital angular and spin contribution (quantum numbers L and S, respectively). In most cases, rare-earth ions are found in a trivalent state A^{3+} [11], which is also the case for the studied $A_2B_2O_7$ oxides [4]. It has the ground state configuration [Xe]$4f^n$, where [Xe] is the xenon configuration and n is the number of electrons in the $4f$ shell. Based on the calculations on the free A^{3+} ions, the ground state is separated from the first excited states by energy of the order of ~10 eV [11]. The ground state multiplet is then split by several interactions with progressively lower magnitude of energy; the example for the Er^{3+} cation is illustrated in Fig. 1.1. The ground configuration is first split into terms by the Coulomb interaction; the new ground term can be straightforwardly determined employing the first two Hund's rules. Afterwards, the third Hund's rule removes the $(2L+1)(2S+1)$-fold degeneracy of the ground term. This is caused by the spin-orbit coupling (SOC) described by an effective Hamiltonian [12]

$$\hat{H}_{LS} = \xi \cdot \hat{L} \cdot \hat{S}, \qquad (1)$$

where ξ is the SOC constant, and $\hat{L}$ and $\hat{S}$ are the operators of the orbital and spin momenta, respectively. Finally, for ions in a crystal lattice, the crystal electric field (CEF) splits the ground state multiplet into a set of singlets, doublets, etc., dependent on the local point symmetry of the ion's crystallographic position. Following with an example of the Er^{3+} ion ($J = 15/2$), its 16-fold degenerate state can be split into a maximum of 8 doublets, based on the Kramers' theorem. In the $A_2B_2O_7$ pyrochlore structure, where A^{3+} occupies a Wyckoff position with a trigonal point symmetry (D_{3d}, $-3m$) [13], eight doublets are dictated (see Fig. 1.1).

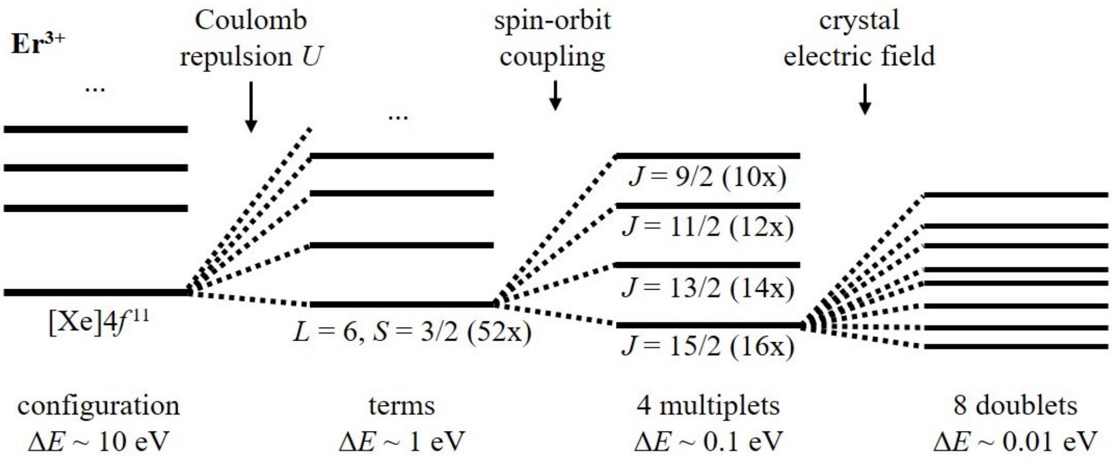

Fig. 1.1: Electron configuration and energy band splitting of an Er^{3+} ion in the $A_2B_2O_7$ pyrochlore structure.

The rare-earth ions' excitation energy scheme can be directly measured, for example, by inelastic neutron scattering, and it can be employed for modelling magnetic susceptibility, isothermal magnetisation, or specific heat. The magnetic moment of the free rare-earth ions can be straightforwardly predicted by the electron configuration, considering the SOC ground multiplet. This includes the effective magnetic moment calculated as $\mu_{\mathrm{eff}} = g\sqrt{J(J+1)}\mu_{\mathrm{B}}$ (g is the Landé g-factor dependent on L, S, and J, and μ_{B} is the Bohr magneton), connected to the Curie-Weiss response of the material. Additionally, the saturated magnetic moment $\mu_{\mathrm{satur}} = gJ\mu_{\mathrm{B}}$ can be predicted. μ_{satur} is the maximum moment reachable in a high magnetic field and at low temperatures. Table 1.1 contains the predicted magnetic moments throughout the rare-earth series. Theoretical values are compared to the experimental results on pure rare earths, which present a good approximation of the free-rare-earth environment [14]. Eu^{3+} and Lu^{3+} are the only nonmagnetic ions ($J = 0$) from the rare-earth series.

Table 1.1: Electron configuration and magnetic properties of the free trivalent rare-earth ions, including the spin numbers L, S, J, Landé g-factor, effective paramagnetic moment μ_{eff}, and saturated moment μ_{satur} (both theoretical and experimental values are listed). The experimental values were determined from measurements on pure rare-earth metals [14]. Yb metal is divalent and nonmagnetic [15].

A^{3+}	$4f^{n}$	L	S	J	g	μ_{eff} theory (μ_{B})	μ_{eff} exp. (μ_{B})	μ_{satur} theory (μ_{B})	μ_{satur} exp. (μ_{B})
Ce	1	3	0.5	2.5	6/7	2.54	2.51	2.14	0.6
Pr	2	5	1	4	4/5	3.58	2.56	3.20	2.7^{α}
Nd	3	6	1.5	4.5	5/7	3.62	3.4	3.27	2.2^{α}
Pm	4	6	2	4	3/5	2.68	-	2.40	-
Sm	5	5	2.5	2.5	2/7	0.85	1.74	0.71	0.13^{α}
Eu	6	3	3	0			nonmagnetic		
Gd	7	0	3.5	3.5	2	7.94	7.98	7.0	7.63
Tb	8	3	3	6	3/2	9.72	9.77	9.0	9.34
Dy	9	5	2.5	7.5	4/3	10.65	10.83	10.0	10.33
Ho	10	6	2	8	5/4	10.61	11.2	10.0	10.34
Er	11	6	1.5	7.5	6/5	9.58	9.9	9.0	9.1
Tm	12	5	1	6	7/6	7.56	7.61	7.0	7.14
Yb	13	3	0.5	3.5	8/7	4.54	-	4.0	-
Lu	14	0	0	0			nonmagnetic		

$^{\alpha}$ Values measured at 38 T

1.2 Electronic structure and magnetism of Ir^{4+} ions

Iridium can exhibit several oxidation states. In the $A_2Ir_2O_7$, iridium has a 4+ valence, which results in five electrons in the 5*d* shell (half-filled $5d^5$). Compared to rare earths, however, the electron configuration of Ir^{4+} is more complex. The 3*d* to 5*d* metals play an important role in the correlated electron physics. Moving from the 3*d* to the 5*d* series, the 5*d* orbitals become more extended, and the Coulomb repulsion U weakens [16]. The SOC, on the other hand, increases remarkably, resulting in a similar strength of electron correlations and SOC in Ir^{4+}. Generally, the 3*d* to 5*d* series have a tendency to not follow Hund's rules due to either hybridisation of covalent bonds or large crystal field, resulting in different expectations for magnetic moments for these ions [17]. Usually, the free Ir^{4+} ion is supposed to be in a low-spin configuration ($S = 1/2$, $J_{\mathrm{eff}} = 1/2$), giving $\mu_{\mathrm{eff}} = 1.73\ \mu_B$ and $\mu_{\mathrm{satur}} = 1\ \mu_B$ [18] (following the Hund's rules would instead result in $S = 5/2$ and $J = 5/2$).

In the case of Ir^{4+} ion in $A_2Ir_2O_7$, the crystal field of octahedral oxygen cage splits the 5*d* states into higher e_g and lower t_{2g} states [19]. That is, *d* orbitals have five degenerate states each for two electrons with opposite spins (10 spins in total); the resulting e_g states are double degenerate and the t_{2g} states are triple degenerate. The t_{2g} states are significantly lower in energy (~2eV difference in $A_2Ir_2O_7$ [16]); therefore, only these are occupied. The band structure becomes more complicated with the introduction of similarly strong SOC and Coulomb repulsion. As seen in Fig. 1.2, the SOC splits the t_{2g} band into the lower $J_{\mathrm{eff}} = 3/2$ (fully filled with four electrons) and the higher $J_{\mathrm{eff}} = 1/2$ band (half filled with one electron) [20]. Additionally, Coulomb repulsion can disturb the two bands, possibly introducing Mott physics with a gap [20,21] (more in the Section *1.5 Metal-insulator transition*). That is, low-energy electronic structure is highly dependent on the distortion of the half-filled $J_{\mathrm{eff}} = 1/2$ band (and possible mixing with the distorted $J_{\mathrm{eff}} = 3/2$ band).

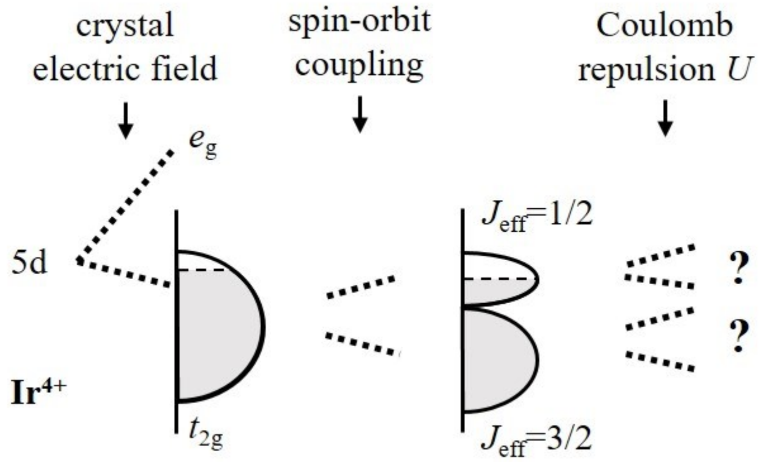

Fig. 1.2: Electron configuration and energy band splitting of an Ir^{4+} ion in the $A_2Ir_2O_7$ pyrochlore structure.

Confluence of the Coulomb repulsion and SOC of the Ir^{4+} electronic structure can result in many exotic ground states, which is one of the main reasons for the condensed matter community's evident interest in the $A_2Ir_2O_7$ iridates [16]. The scenario of a strong Coulomb interaction over a weak SOC would result in the typical Mott insulator state. On the other hand, a strong SOC compared to a weak electron correlation introduces the region of topological insulators and semimetals. In the case of $Ir^{4+,}$ where both interactions are of similar strength, exotic ground states such as Weyl semimetal, axion insulator, or topological Mott insulator have been predicted and reported [16]. Weyl semimetals are characterised by the presence of quasiparticle excitations with exceptionally high mobility, called Weyl fermions. In these materials, the so-called Fermi arcs connect the Weyl nodes of opposite chirality [5,22]. In the axion insulator, the Weyl points annihilate in pairs, resulting in a topological (quantised) magnetoelectric effect protected by the inversion symmetry [7]. A topological Mott insulator is, as the name suggests, an intermediate state between the familiar Mott insulator and the topological band insulator. It is characterised by the deconfined neutral spinons and can be regarded as a quantum spin-liquid state [8].

1.3 Geometrical frustration

Although there are different kinds of frustration in both physics and human lives, we restrict our focus to the so-called geometrical frustration in magnetic materials. This topic includes mostly materials with triangular patterns in their crystal lattice. In two dimensions, it is represented by an edge-sharing or corner-sharing triangular lattices, the latter of which is also known as the Kagomé lattice. Such a lattice is realised also in 3D as the so-called hyper-Kagomé lattice. Alternatively, in 3D, four equilateral triangles can form a tetrahedron. Crystal lattices of edge-sharing tetrahedra (face-centred cubic) and corner-sharing tetrahedra (pyrochlore) are quite common in nature [4]. In the case of $A_2Ir_2O_7$ iridates, crystallising in a pyrochlore structure, both A^{3+} and Ir^{4+} cations separately reside in 3D geometrically frustrated sublattices.

In general, geometrical frustration suppresses the long-range magnetic ordering. As a result, some materials fail to order even at extremely low temperatures, resulting in an extensive amount of ground-state entropy. Fascinating ground states can emerge, such as spin liquid, spin ice, or spin glass state [3]. The spin liquid is a magnetically disordered (no static order), yet strongly correlated state. In other words, a dense cooperative paramagnet. The spin fluctuations in this state are either classical or quantum. The case of quantum spin liquid, which does not order even at the absolute zero temperature due to the quantum mechanical uncertainty principle, has been of considerable interest lately [23]. The spin ice state is correlated following the so-called ice rule, as an analogue to rotations of molecules in regular ice. For example, it was observed in $Dy_2Ti_2O_7$ and $Ho_2Ti_2O_7$ titananes [3]. There, two spins are always pointing inside the tetrahedron while the two other spins point out. As each tetrahedron can have six different configurations, the ground state entropy is extensive in the macroscopic sample. The spin glass state results from a combination of frustration and randomness. One way of achieving this is diluting a geometrically frustrated lattice with diamagnetic ions. Typical signatures of the spin glass state are a frequency-dependent magnetic susceptibility and a linear temperature dependence of heat capacity. A spin glass state was observed in an ordered pyrochlore structure of $Y_2Mo_2O_7$, that is, a small local disorder could still cause this phenomenon [3].

The magnitude of the geometrical frustration can be conveniently characterised by the so-called frustration index, defined as [3]

$$f = |\theta_{CW}|/T_C. \tag{2}$$

Here, θ_{CW} is the paramagnetic Curie-Weiss temperature and T_C is a critical temperature. T_C can be a temperature of long-range order (Curie or Néel temperature), a glassy transition, or a transition into a spin ice state, etc. Materials which have a transition at very low temperatures have a high frustration index. Theoretically, a quantum spin liquid which does not order down to 0 K has an infinitely large frustration index.

1.4 Electrical transport

According to the theories of electronic band structure, solids can be classified into metals, insulators, and semiconductors. Metals have a half-filled electron band, resulting in low electrical resistivity (high conductivity). In the simplest approach, contributions to the electrical resistivity of metals are independent, following Matthiessen's rule:

$$\rho_{tot} = \rho_0 + \rho_{therm} + \rho_{e-e} + \rho_{mag}. \tag{3}$$

The total electrical resistivity ρ_{tot} is separated into the following contributions: The constant residual resistivity ρ_0 results from electrons scattering on defects in the material. Thermal contribution ρ_{therm} origins in electron-phonon interactions and depends linearly on temperature at higher temperatures and approximately as T^5 at low temperatures. Electron-electron contribution ρ_{e-e} is described within the Fermi-liquid theory. It is dominant at the lowest temperatures as a function of T^2. Finally, magnetic contribution ρ_{mag} is constant in the paramagnetic state but behaves differently in the ordered states, commonly creating a small kink in the electrical resistivity data at the ordering temperature.

Semiconductors and insulators have a gap between a filled and empty electron band. The energy difference between the two corresponds the magnitude of the gap. In simple terms, the electrical resistivity of semiconductors increases upon cooling because the electrons lose the energy to overcome the insulating gap. This can be described with the Arrhenius law (thermal activation of carriers), which is commonly used at higher temperature regions:

$$\rho(T) = \rho_A e^{\Delta/T}. \tag{4}$$

Here, ρ_A is the pre-exponential factor, and Δ is the gap energy. However, the behaviour of electrical resistivity often does not follow the activation rule precisely, especially at lower temperatures. One of the models encapsulating this is the so-called variable-range hopping (VRH) model. A more specific example is called the Mott VRH model, which describes the electrical resistivity of disordered systems which contain localised carriers [24], expressed as the following:

$$\rho(T) = \rho_A e^{(T_0/T)^{1/4}}, \tag{5}$$

where T_0 is the characteristic temperature. Finally, reaching even lower temperatures, some materials tend to diverge from the Mott VRH. For such cases, calculations consider also the effect of the Coulomb gap near the Fermi level, described by the formula of the so-called Efros–Shklovskii VRH [25]:

$$\rho(T) = \rho_A e^{(T_0/T)^{1/2}}. \tag{6}$$

1.5 Metal-insulator transition

Although materials with predicted partially filled electronic bands are indeed behaving like metals in most cases, there were exceptions discovered. Some transition-metal oxides were reported to be insulators despite having a partially filled d-electron band, e.g., NiO or La_2CuO_7 [26]. As this phenomenon was ascribed to the electron-electron correlations, a long history of research in the field of strongly correlated matter began, in hopes of being able to easily tune metallic/insulating properties of materials through the so-called metal-insulator transitions (MIT). Most notably, a lot of theoretical achievements in this field are connected to the articles of N. F. Mott spanning from 1949 to 1990 [26]. Therefore, materials which were predicted to be metals (based on electron structure calculations), but acted in reality as insulators have been classified generally as “Mott insulators”. In simplicity, Mott insulators are not conducting because of a large Coulomb repulsion between two electrons that occupy the same site, resulting in band splitting (gap creation). A theoretical understanding of a transition between metal and Mott insulator was achieved employing the so-called Hubbard model with a Hamiltonian [27]:

$$\hat{H} = -\sum_{i,j\in\Lambda}\sum_{\sigma} t_{ij} c_{i\sigma}^{+} c_{i\sigma} + U \sum_{i\in\Lambda} c_{i\uparrow}^{+} c_{i\downarrow}^{+} c_{i\downarrow} c_{i\uparrow}, \tag{7}$$

where t is the hopping amplitude, $c(c^{+})$ is the annihilation (creation) operator, σ is the spin, Λ is a set of spatially localised orbitals, and U is the Hubbard repulsion. The first term represents the hopping of electrons in the tight-binding framework, and the second term represents the nonlinear repulsive interactions. For Ir^{4+}, the splitting of the half-filled $J_{eff} = 1/2$ band originates in the Hubbard model electron-electron correlations.

Another notable interpretation of the insulating behaviour seen in transition-metal oxides is the so-called Slater model. Instead of Coulomb interaction, the Slater model works based on antiferromagnetic (AFM) ordering. A periodic perturbation of the magnetic ions' potential created by a commensurate AFM ordering leads to the splitting of the electronic band [28]. Indeed, most materials exhibiting an MIT also show an AFM ordering. However, energy tied purely to the AFM order is generally significantly smaller compared to the U from the Hubbard model. Although overshadowed by the Mott model in many cases, the Slater model was used multiple times to describe the intricate behaviour of compounds containing 5d elements, e.g., $Cd_2Os_2O_7$ [29] or $NaOsO_3$ [30].

While the Mott mechanism works very well on materials with partially filled 3d orbitals, when we move to 4d and 5d orbitals, the electronic repulsion diminishes as the orbitals become more extended. This gives space for effects stemming from the magnetic order, i.e., the Slater mechanism. The main differences between the two mechanisms are: in the Slater picture, the MIT exists below the Néel temperature, i.e., it is induced by the AFM state. In the Mott picture, the gap exists already above the AFM order. Moreover, the Slater transition is predicted to be continuous, while the Mott transition is often associated with a first-order transition [31]. When the AFM transition and the MIT happen (seemingly) concomitantly (the case of $A_2Ir_2O_7$ or $Cd_2Os_2O_7$ [31,32]), it is not clear which mechanism should be attributed to the creation of the MIT. Therefore, both mechanisms are sometimes used to explain the forming of the MIT [29,33] (or rather, there are cases when scientists argue with each other over which mechanism is dominant, e.g., the case of $SrIrO_4$ [33,34]).

The thermodynamics of the Slater MIT were previously calculated employing the mean-field approximation [35]. Based on these calculations, below the MIT, the electrical resistivity behaves in the same way as an opening of a BCS gap in a superconductor. Although a precise description is very complex, an excellent approximation of this behaviour can be expressed as [36]

$$\left[\frac{\Delta(T)}{\Delta(0)}\right]^2 = \cos\left[\frac{\pi}{2}\left(\frac{T}{T_C}\right)^2\right]. \tag{8}$$

Here, $\Delta(T)$ is the gap energy and T_C is the critical/transition temperature.

1.6 Compressibility

Tuning of the electrical and magnetic properties can be achieved by changing the structural parameters of the studied materials. Three main techniques are standardly considered in this regard: temperature change, chemical substitution (chemical pressure) and external pressure. Although decreasing the temperature often leads to the contraction of the crystal lattice, temperature also affects the occupations of (quantum) states. Chemical pressure can result in much greater changes in lattice parameters than temperature change, but it often introduces disorder in the system and changes the energy levels completely by introducing more/fewer electrons into the system. External pressure is, in comparison, a clean method of tuning the interatomic distances. Contraction of the lattice results in a greater overlap of the electron orbitals, making the electrons more delocalised. In general, it is expected that a material under external pressure becomes more conducting while ferromagnetism or superconductivity are be suppressed. On the other hand, the application of pressure can sometimes enhance magnetic properties [37] or even create superconductivity in normally non-superconducting materials [38]. Moreover, the application of pressure can lead to the formation of new (meta)stable phases of matter with completely different structure and properties.

1.6.1 Compressibility under high pressure

Pressure, in the most general way, can be described by the stress tensor with nine components, three of which represent the direct/normal stress (responsible for compression), and six represent the shear stress (responsible for deformation/shape change) [39]. Hydrostatic pressure requires all direct stresses to be equal, as well as the absence of any shear stress. This results in a stable compression of the sample without any change of shape, which is also desirable as a concept for theoreticians calculating pressure effects. That is, the application of hydrostatic pressure preserves the lattice symmetry. It is, however, an ideal concept that cannot be realised perfectly, but is achieved to reasonable degree using liquid or gas pressure-transmitting medium. If the medium is solid (or solidifies during the experiment), the created conditions are, at best, described as quasi-hydrostatic. The pressure is then considered approximately hydrostatic at the local scale, while different areas of the sample can be under different pressure, characterised by a pressure distribution. In the simple case of an elastic contact of an indenter and a plane, it is possible to calculate the pressure distribution with the following equation [40]:

$$p_\eta(r) = \frac{2\eta+1}{2}\frac{Q}{\pi {r_0}^2}\int_0^{\sqrt{1-r^2/{r_0}^2}}\left(\frac{r^2}{{r_0}^2}+x^2\right)^{\eta-1} dx, \tag{9}$$

where η describes the indenter shape, r_0 is the contact area radius, and Q is the load applied on the indenter (see Fig. 1.3). Employing these calculations confirmed that using anvils of nearly-conical shape leads to the highest pressures, seen in the use of diamond anvil cells.

Although most high-pressure studies aim to create hydrostatic pressure, the so-called uniaxial pressure is used for tuning anisotropic properties of single crystals. In this case, only one of the normal stress components is non-zero, and the sample is compressed only along one direction. Usually, the material expands in the perpendicular directions. Being able to tune interatomic distances anisotropically creates an interesting playground for condensed matter physics, especially for theory, as more and more atomic structures are studied and refined. While knowing the microstructure, applying uniaxial pressure can be used to tune very specific anisotropic properties of solids. Unfortunately, it is also very limited experimentally, as relatively low pressures (compared to hydrostatic experiments) can destroy the sample before desirable properties are reached.

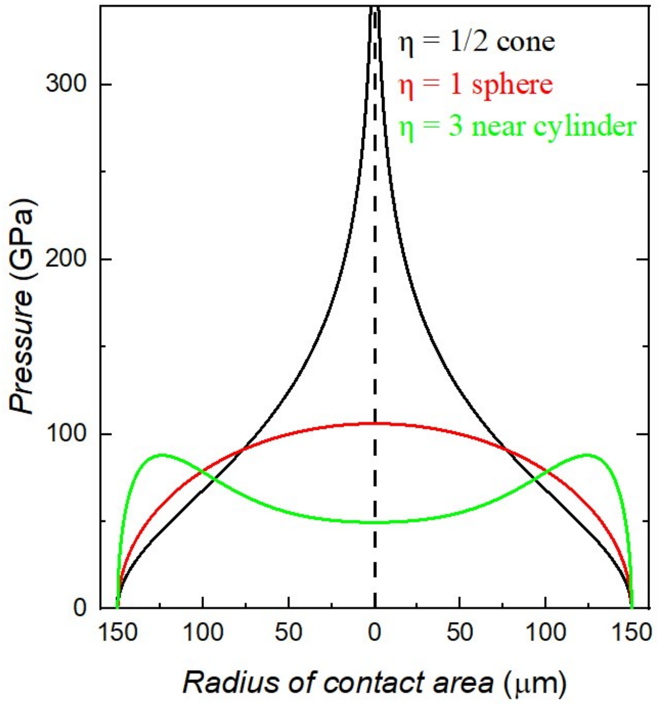

Fig. 1.3: Pressure distributions over the area of an elastic contact of an indenter with a plane. The indenter has the shape of a cone (η = 1/2), a sphere (η = 1), or a near cylinder (η = 3). Calculations were done with the same load Q = 250 kg and contact area radius r_0 = 150 μm [40].

Compressibility of materials is characterised by the equations of state (EoS). Focusing on external pressure, the isothermal EoS introduces the bulk modulus of the material (inverse of compressibility) as

$$K = -V(\partial P/\partial V)_T. \tag{10}$$

For hydrostatic pressure and infinitesimal changes in volume, the linear elasticity theory can be applied, tying the bulk modulus to six components of the compressibility matrix of materials as [39]

$$K = [s_{11} + s_{22} + s_{33} + 2(s_{12} + s_{13} + s_{23})]^{-1}. \tag{11}$$

However, for experiments at high pressure, linear elasticity theory often fails as it cannot describe finite changes in volume. As the material is being significantly compressed, it is important to deal with the decrease of compressibility with pressure, i.e., no material can be compressed to zero volume. For this purpose, EoS that are in a sense an extension of linear elasticity are used. There is, however, no absolute thermodynamic basis for specifying how the bulk modulus changes with pressure. Therefore, different models for EoS were proposed, bearing different assumptions and approximations, whose correctness can often only be based on the agreement with experimental data.

One of the simplest EoS can be derived from the assumption that the bulk modulus depends on pressure linearly. The so-called Murnagnan EoS [41] is very popular since it has a simple invertible form that can describe volume as

$$V_{PT} = V_{0T}(1 + K'_{0T}P/K_{0T})^{-1/K'_{0T}}, \tag{12}$$

where K_{0T} and K'_{0T} are the bulk modulus and its derivative at ambient pressure and temperature T. Although it uses a strong assumption of linearity, it can still reproduce data of small compressions. That is, it is reasonable to use this EoS with compressions no larger than 10% (volume down to 90%). For larger strain, the second derivate of the bulk modulus K'' needs to be employed as well. One such model is the so-called Birch-Murnaghan EoS [42], which assumes that the strain energy of the compressed solid

$$f_E = \left[(V_{0T}/V_{PT})^{2/3} - 1\right]/2 \tag{13}$$

can be expressed as a Taylor series in the finite Eulerian strain. Expansion to the fourth order in strain then leads to the equation

$$P = 3K_{0T}f_E(1 + 2f_E)^{\frac{5}{2}}$$
$$\left[1 + \frac{3}{2}(K'_{0T} - 4)f_E + \frac{3}{2}\left(K_{0T}K''_{0T} + (K'_{0T} - 4)(K'_{0T} - 3) + \frac{35}{9}\right)f_E^2\right]. \tag{14}$$

In most cases, the third-order Birch-Murnaghan EoS is employed. This is introduced by a third-order truncation, setting the coefficient f_E^2 to zero. Just as in the case of the Murnaghan EoS, it is a three-parameter EoS (with V_{0T}, K_{0T}, and K'_{0T}), but now with a nonzero K''_{0T} which is implied by the truncation condition. On the other hand, it cannot be simply inverted like the Murnaghan EoS to a form of pressure-dependent volume function. Lastly, for even higher volume variations (even below 60% of ambient volume), the so-called Vinet EoS [43] can be used, for example. This EoS is derived from generalised interatomic potential and is also a three-parameter EoS with implied K''_{0T}.

1.6.2 Thermal compressibility

Similarly to pressure, thermal compressibility can also be understood by employing a reasonable EoS, characterised by the thermal (isobaric) expansion coefficient

$$\alpha = V^{-1}(\partial V/\partial T)_P. \tag{15}$$

The simplest approximation would be a constant α, which would result in linear thermal compressibility. An extension that accommodates non-linear behaviour was proposed by Berman [44], resulting in the following EoS:

$$V_T = V_0\left(1 + \alpha_0 T + \frac{1}{2}\alpha'_0 T^2\right), \tag{16}$$

where α_0 and α'_0 are the thermal coefficient and its derivative at 0 K. Although simple to implement, this model always fails at low temperatures since it expects finite thermal expansion at 0 K. A more complex EoS can be derived, e.g., using assumptions of the early Debye's model for specific heat and Grüneisen theory of thermal expansion. More specifically, we assume that the thermal expansion is tied to the phonon contribution of specific heat and even to the bulk modulus through the Grüneisen parameter [45]

$$\gamma = \alpha K V / C_V, \tag{17}$$

where K is the isothermal bulk modulus and C_V is the isochoric specific heat. Following the assumptions of the Debye's model for specific heat, thermal compressibility can be described as [45]

$$V_T = V_0 + I_V T F(\theta_D / T), \tag{18}$$

where V_0 is the volume at 0 K, $I_V = 3k_B r_{at} \gamma / K_0$ is dependent on the Grüneisen parameter and the bulk modulus (k_B is the Boltzmann constant, r_{at} is the number of atoms in the polyatomic basis) and $F(\theta_D/T)$ is an analytical integral used in Debye's theory, employing Debye's temperature θ_D. The resulting EoS has three parameters – θ_D, I_V, and V_0. That is, fitting the data to this model results in an estimation of the Debye temperature of the material θ_D, zero-temperature volume V_0, and moreover, with the knowledge of the bulk modulus, it is possible to estimate also the Grüneisen parameter γ. The fitting process, however, does not use the analytical Debye integral, but instead a simplified fourth-order polynomial approximation that works very well in the temperature range above ~ $\theta_D/10$, the so-called Thacher's approximate function [45]. Unfortunately, this means the lower temperature region should not be included in the fitting process. Additionally, the model expects knowledge of high-temperature compressibility (based on high-temperature phonon contributions), which is not naturally measured during low-temperature experiments. Therefore, parameters are to be calculated asymptotically, fitting different temperature regions (from $\theta_D/10$ to T_{i} while increasing T_{i} as much as possible). Finally, the temperature region below $\theta_D/10$ is calculated based on the fitted parameters and the low-temperature part of Thacher's function. The resulting EoS not only models the compressibility down to 0 K but also connects it to physical properties measured with specific heat experiments.

2. Experimental methods

Most of the experimental methods described in the following chapter (except for diamond anvil cell and synchrotron radiation techniques) are available at the Department of Condensed Matter Physics and the Materials Growth & Measurement Laboratory (MGML). For further details about instrumentation, see Ref. [46].

2.1 Sample synthesis – flux growth

The flux growth method is a well-established technique for the synthesis of unstable, high-temperature- or incongruently-melting materials [47]. In the case of rare-earth iridates, high evaporation and decomposition of the iridium dioxide prevents effective growth of crystals using other commonly employed methods. The main advantage of the flux method is that the precursors dissolve in the melted flux well-below their melting temperature. The crystal nucleation begins once the critical concentration is reached. While the desired single crystals are slowly growing in the oversaturated environment, the critical concentration of the dissolved precursors can be maintained by controlling the temperature or the evaporation of flux. This process can take several hours or days, slowly adjusting the temperature. As a result, usually relatively small single crystals are created, frequently with clear facets similar to crystals grown in nature. Disadvantages of the flux method compared to, e.g., Czochralski pulling method, Bridgeman method, or floating-hot-zone method, are: the single crystals are often much smaller and there is a chance of contamination of the samples by the flux. Therefore, the right choice of the material used as flux is paramount.

2.2 Structural and phase characterisation

After the synthesis of the selected material, it is essential to check the structure, correct stoichiometry, and overall quality of the grown sample. This is done routinely at the home facility of the Department of Condensed Matter Physics employing the following methods.

2.2.1 Powder X-ray diffraction

The structure parameters (including the space group, lattice parameters and atomic positions), as well as the presence of any foreign phase in the sample, can be determined by powder X-ray diffraction (XRD). We employed the Bruker D8 advanced diffractometer with the conventional Bragg-Brentano geometry and a copper K_α X-ray source [46]. From the position of the diffraction peaks, it is possible to determine the space group and the lattice parameters of the structure. More complex analysis, which includes the intensity of the peaks, ultimately reveals structural details, e.g., atomic positions within the specific space group, occupancy, preferential orientation, etc. [48]. Moreover, any additional peaks not in agreement with the fit prove the presence of a foreign phase/s. In our case, the finely ground powder was spread out with toluene on a silicon plate and then scanned in most cases from 10 to 110 degrees in 2θ. The measured diffraction patterns were fitted using the Rietveld method and the Fullprof suite [49] or the Topas academic suite [50].

Routine laboratory powder XRD experiments are sufficient for the confirmation of the correct structure and the presence of minority phases. Although complex information can be extracted from laboratory XRD given sufficient sample quality, experimental setup and exposition time, synchrotron facilities are nowadays employed for the highest resolution experiments, revealing fine details of the structure (see Section *2.5 Synchrotron radiation experiments*).

2.2.2 Laue method

Single crystals of sufficient size (typically with dimensions ≥ several hundred μm) are routinely checked employing the Laue diffraction technique. It is a quick and useful technique capable of revealing the quality and orientation of a single crystal. Since it employs a polychromatic X-ray beam (or neutron beam in the case of large-scale facilities), multiple Bragg reflections can be measured by a 2D detector at once. Clear reflections in agreement with the simulated diffractogram (based on the structural model) are a sign of a good-quality single crystal, especially when good agreement is observed after rotating the crystal. In addition, the symmetry of the crystal is apparent from the symmetry of the diffractogram, serving as an additional check of the correct structure. In addition to quality checks, the Laue method is used to orient samples for measurements along specific crystallographic directions, which is otherwise impossible on crystals without well-defined facets. However, Laue diffraction cannot be used reasonably for determining crystal lattice parameters. Specifically, for crystals with a cubic structure (e.g. pyrochlore structure), varying the lattice parameter a does not change the positions of the diffracted reflections (due to the polychromatic nature of the X-ray beam).

The Laue method was employed on the backscattering diffractometer (Photonic Science) [46]. It uses a Cu X-ray tube, back reflection geometry, and a CCD camera for the acquisition of the backscattered signal. The resulting diffractograms are compared to the simulations made by CLIP (Cologne Laue Indexation Program) [51].

2.2.3 Single crystal diffraction

After initial confirmation of single crystal quality by the Laue diffraction. Single crystal diffraction can be employed for determining structural parameters (or solving the structure if it is unknown). It works similarly to powder diffraction, but in this case, there is only one grain to diffract from. That is, it is much more difficult to satisfy the Bragg law and find a reflection compared to the powder diffraction. This usually involves the use of a complex goniometer able to rotate the single crystal. As a result, the process can become relatively time-consuming. The required sample is usually small (tens or hundreds of μm dimensions) and of good quality. The refined structural information is very rich as the diffraction positions and intensities are measured accurately. Single crystal diffraction is an essential method especially when solving new structures.

The single crystal diffraction measurements were done in collaboration with the Institute of Physics, Academy of Sciences of Czech Republic. We employed a four-cycle diffractometer (Gemini from Rigaku Oxford Diffraction) equipped with a Mo X-ray tube ($\lambda_{K\alpha}$ = 0.71073 Å), graphite monochromator, Mo-enhance collimator, and an Atlas CCD detector. The crystals were glued on a glass fibre and mounted onto a goniometer head. The diffraction patterns were collected at 120 K. The CrysAlisPro software [52] was used to reduce the data and to face-index the crystal shape. This is necessary to perform the empirical absorption correction using spherical harmonic functions implemented in the SCALE3 ABSPACK scaling algorithm. Structural solution was done using the Superflip program [53]. Finally, Jana2020 package [54] was employed for structural refinement.

2.2.4 Scanning electron microscopy

Scanning electron microscopes (SEM) provide multiple useful methods for the characterisation of materials, including composition, topology, and grain distribution. The accuracy and the penetration depth are dependent on the electron energy (voltage). That is, procured information is limited to the near surface (up to a few μm penetration). The backscattered electron (BSE) method can be used to check the quality of the surface and the existence of different phases or grains. The secondary electrons (SE) method is used for the highest-resolution topology scans. The energy dispersive X-ray analysis (EDX) is a technique combined with the SEM to determine stoichiometry of materials. Excitations between core energy levels have a characteristic wavelength. Scanning the spectrum of emitted X-rays, it is possible to determine the elemental composition of very precise spots on the studied sample. Limitation of the techniques is that the sample cannot be an insulator (it would be charged by the electrons, preventing reasonable interaction with further incoming electrons). Furthermore, the sample stoichiometry is determined with an error of a few percent and the technique is only qualitative for atoms with a small atomic number, e.g., oxygen. Therefore, in the case of $A_2Ir_2O_7$, it is reasonable to check only the stoichiometry of the rare-earth A and Ir to be 50:50. Light elements can be effectively investigated using sister methods such as X-ray photoelectron spectroscopy (XPS) and X-ray fluorescence (XRF).

Measurements were done on the SEM Tescan Mira I LMH [46]. Among other methods, BDE, SE, and EDX are routinely employed on this microscope for the basic characterisation and the quality check of the synthesised crystals. Routinely, the A and Ir composition of the $A_2Ir_2O_7$ samples can be checked with an error of up to 1-2%. Of course, only near-surface information can be obtained; samples would need to be polished or cut to gain more in-depth information.

2.3 Investigation of magnetic and transport properties

In this section, we focus on the methods used for the measurements of bulk material with varying temperature and magnetic field. Three devices were employed: Physical Property Measurement System (PPMS), Magnetic Property Measurement System (MPMS), both from Quantum design, and a closed-cycle refrigerator (CCR) from Sumitomo Heavy Industries / Janis Research [46]. PPMS and MPMS are equipped with a superconducting magnet, and the MPMS also with a superconducting quantum interference device (SQUID).

2.3.1 Electrical resistivity

Electrical resistivity was measured with the 4-probe method in order to minimise the contribution from the leading wires. Cold-pressed powder pellets of dimensions approximately 3x1x1 mm^3 were investigated. We attempted to measure also small single crystals (edge of approximately 500 μm). In this case, the quasi-4-probe method was employed; i.e., instead of four contacted spots on the sample, each with one lead, there were two contacted spots, each with two leads (one for voltage and one for current). This was due to the difficulty of preparing four contacts on such small samples. Considering the semi-metallic/insulating nature of the measured $A_2Ir_2O_7$ samples, the additional parasitic contribution from the wires is negligible. The poor conductivity of the samples prevented the use of spot welding; instead, DuPont silver conductive paste or Lake Shore low-temperature conductive epoxy was used for the preparation of electrical contacts.

Measurements were done mostly in the PPMS, allowing the investigation in a temperature range of 2-310 K and magnetic field range of 0-9 T. Since the electrical resistivity of our $A_2Ir_2O_7$ samples reached orders of MΩ at low temperatures in selected cases, a special electric current source had to be used (department laboratories are normally equipped for low-resistivity measurements; therefore measurements up to MΩ are not done routinely). Keithley 6221 (current source) and Keithley 2182A (nanovoltmeter) were employed with the Delta method, which automatically triggers the current source to alternate the signal polarity and then triggers a nanovoltmeter reading at each polarity. Ambient pressure experiments were done on the specialised measurement puck. During the high-pressure experiments (see Section *2.4 High pressure techniques*), a piston-cylinder cell was attached to a connector compatible with the PPMS.

Measurements (especially the initial ones) were done also in the CCR [46]. Compared to the PPMS, the CCR is not equipped with a magnetic field option and the lowest temperature limit is approximately 3 K. On the other hand, the advantage of the CCR is the thermal stability of the apparatus, especially for experiments with pressure cells. Compared to the PPMS, where a temperature hysteresis during the pressure cell measurement was evident even at 1 K/min cooling speed (not enough thermal conductivity through the pressure cell connector), no hysteresis could be detected on the CCR measurements. No magnetic field option also guarantees zero residual magnetic field, which cannot be neglected for PPMS or MPMS when measuring systems highly sensitive to magnetic field. Furthermore, the CCR has larger sample space, capable of accommodating pressure cells that are too large for PPMS or MPMS.

2.3.2 Heat capacity

Heat capacity (or specific heat) measurements can reveal important information about the structural, conducting, and magnetic properties of materials, especially about transitions between individual phases. All phase transitions are associated with a certain amount of free energy/entropy that is reflected in an anomaly in the specific heat. Additionally, crystal electric field excitations result in the magnetic specific heat in the form of theoretically well-defined Schottky contributions [55].

Measurements were performed in the PPMS using a specialised puck that has a platform fixed solely by leading wires. For every data point, a heat pulse is delivered to the platform, and subsequently, the temperature relaxation is scanned with a thermocouple. In the so-called relaxation method, the exponentially relaxing temperature is fitted to obtain the specific heat of the whole platform (with the attached sample). After the subtraction of the contributions from the platform and apiezon (grease used to fix the sample onto the platform with good thermal conductivity), the contribution solely from the sample is obtained. The accessible temperature range employing the standard PPMS option is 2-400 K (the so-called ^{4}He option). Temperatures down to 0.4 K can be reached with the ^{3}He insert (^{3}He option). However, only low temperatures up to ~6 K can be scanned reliably this way. Combining these two techniques, it is possible to acquire data from the temperature range of 0.4-400 K. Simultaneously, a magnetic field in the range of 0-9 T can be applied during the measurement (in one specific direction and its opposite).

Unfortunately, the preferred sample mass required for each option is different. This often results in the measurement of two different samples. For ^{4}He measurements, a mass of at least a few mg is preferred, whereas for ^{3}He measurements, 1 mg or less is normally sufficient (also highly dependent on sample thermal conductivity). The shape of the sample is also important; plate-like samples are ideal to ensure good contact with the platform. Additionally, the error of determining the mass of the sample and apiezon (and sometimes nonmagnetic analogue for determination of magnetic contributions) stack together, making the data analysis difficult, especially at high temperatures.

2.3.3 DC magnetisation

DC (direct current) magnetisation measurements allow direct determination of the total magnetic moment of the sample as well as magnetic susceptibility. Temperature scans can indicate phase transitions and reveal ordering temperatures and their basic nature. Magnetic field scans follow the saturation of magnetic moments, metamagnetic transitions, or possible remanent magnetisation and coercive field.

MPMS-XL 7 T magnetometer was employed to measure DC magnetisation, able to reach temperatures between 1.8-400 K and magnetic field up to 7 T. MPMS uses a SQUID detector, which is an extremely precise magnetisation detector, in principle, capable of distinguishing between quanta of magnetic flux. Aside from the conventional DC scanning method, the reciprocating sample option (RSO) method was used to reach a sensitivity of the order of 10^{-8} emu needed to measure signals from ferromagnetic domain walls in tiny $A_2Ir_2O_7$ single crystals (see Section *4.4 Antiferromagnetic domain structure*). The RSO method uses a slow oscillatory movement of the sample inside the detection coil to read the signal continuously, instead of standard step-like measurements.

2.3.4 AC magnetic susceptibility

AC (alternating current) magnetic susceptibility measurements are more complex than DC measurements, employing oscillatory magnetic field and looking at frequency dependencies of magnetic susceptibility. Instead of moving the sample, the induction coil produces AC magnetic field that induces magnetisation in the sample, which is afterwards detected by the detection coil. Some materials, e.g., spin liquids, which are not ordered long-range due to magnetic frustration, exhibit anomalies that are dependent on the frequency of the AC magnetic field.

MPMS and PPMS have the option to measure AC susceptibility. Furthermore, it is possible to measure AC susceptibility in the PPMS in high-pressure cells using homemade coils. For this purpose, we used a coil (both induction and detection coils packed together) with an inner diameter of 1.6 mm, small enough to fit inside the hybrid piston-cylinder pressure cell. This way, it is possible to scan relative changes in AC susceptibility at high pressure. However, it no longer uses the SQUID technology; therefore, the sensitivity is significantly lower, and the determined values are qualitative only. Nevertheless, it can be combined with the SQUID measurements at ambient pressure to reasonably scale the high-pressure data to correct absolute values of AC magnetic susceptibility.

2.4 High pressure techniques

2.4.1 Hybrid piston-cylinder cell

Commercially available from the C&T Factory Co., Ltd, the hybrid piston-cylinder pressure cell provides large versatility compared to anvil cells, but at the cost of much lower pressure limit and incompatibility with X-ray diffraction. Composed of an inner cylinder (Ni-Cr-Al alloy) and outer cylinder (CuBe alloy), it is built to routinely withstand up to 3 GPa of pressure (see Fig. 2.1). Its biggest advantage is the large sample space with the diameter $d = 3$ mm and length $l \cong 9$ mm. It also has a compatible size with the PPMS, allowing for measurements of electrical resistivity, AC susceptibility, compressibility, or specific heat of relatively large samples. Data are acquired through electrical leads connected to the sample space. Pressure is determined at room temperature with a calibrated manganin manometer [40] located inside the cell, next to the sample, with an experimental error of approximately 0.05 GPa. Equal redistribution of pressure (hydrostatic conditions) is achieved using liquid pressure-transmitting media from the Daphne oil series. For example, the employed Daphne 7575 remains liquid at ambient temperature up to approximately 4 GPa of pressure [56], i.e., in the whole applicable pressure region. Of course, cooling down the pressure cell results in the solidification of the pressure-transmitting medium (quasi-hydrostatic conditions). However, non-hydrostaticity caused by such a solidification is insignificant as the pressure is not changing much in a closed cell during the cooling/heating process. That is, it is far more important to ensure the hydrostatic conditions during pressure application (done usually at room temperature) to ensure highly hydrostatic conditions.

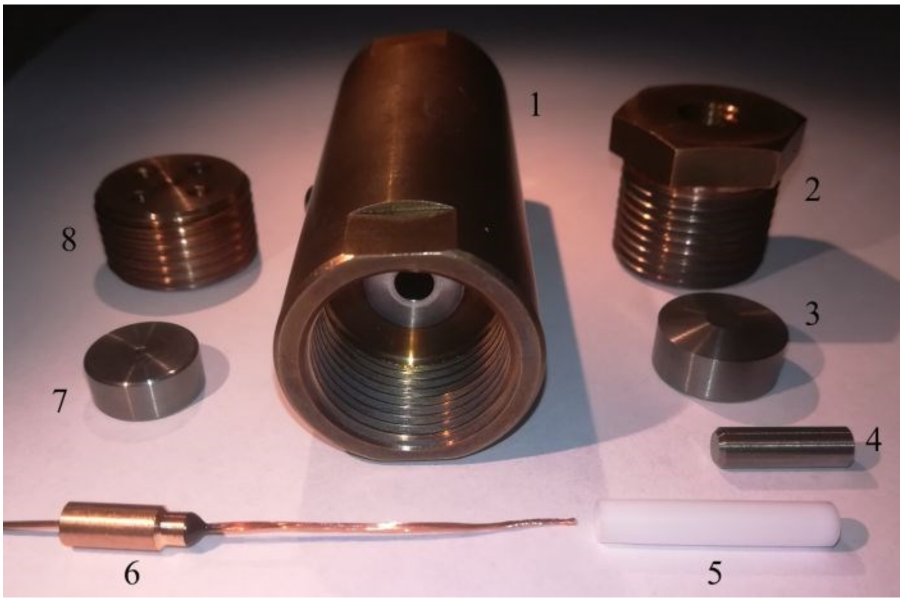

Fig. 2.1: Components of the hybrid piston-cylinder cell: 1. Main body made of two cylinders, 2-3. Front piston support, 4. Piston, 5. Teflon cell (sample space inside), 6. Plug for electrical leads, 7-8. Plug support.

2.4.2 Diamond anvil cell

Diamond anvil cells (DAC) have two main advantages over other types of pressure cells. Firstly, diamond is the hardest mineral, therefore it can withstand more load than other materials without breaking. Secondly, diamonds are transparent to a wide range of the electromagnetic spectrum, making DACs extremely viable in combination with hard-X-ray synchrotron sources. Within the current study, DACs rented at large-scale facilities were employed [57], with a safe limit of 20 GPa, and the diamond culet size of 600 μm in diameter. A disassembled DAC can be seen in Fig. 2.2a. A piece of thin steel plate is used as the gasket – indentation by the diamond anvils is followed by drilling a hole with $d \sim 300$ μm in the middle of the indent. However, at the high-pressure limit of the cell, the gasket hole's diameter shrinks approximately to half, reducing the sample space to a cylinder with a diameter $d \sim 150$ µm and height $h \sim 50$ µm. Within this space, samples are placed together with tiny rubies (possibly more than one sample per pressure cell if the beam is very focused). Fluorescence of a ruby is commonly used to determine the pressure within the cell [58]. He gas was used as the pressure-transmitting medium. Employing a specialised apparatus, the sample space was filled with He compressed significantly with 1400 bars before sealing it. Arguably the most hydrostatic option, He solidifies above 12.1 GPa at 300 K and keeps the standard deviation of determined pressure at approximately 0.05 GPa within the 20 GPa pressure range used [59]. The load was applied by a built-in He membrane, which is capable of tuning the load in situ, delicately, and remotely.

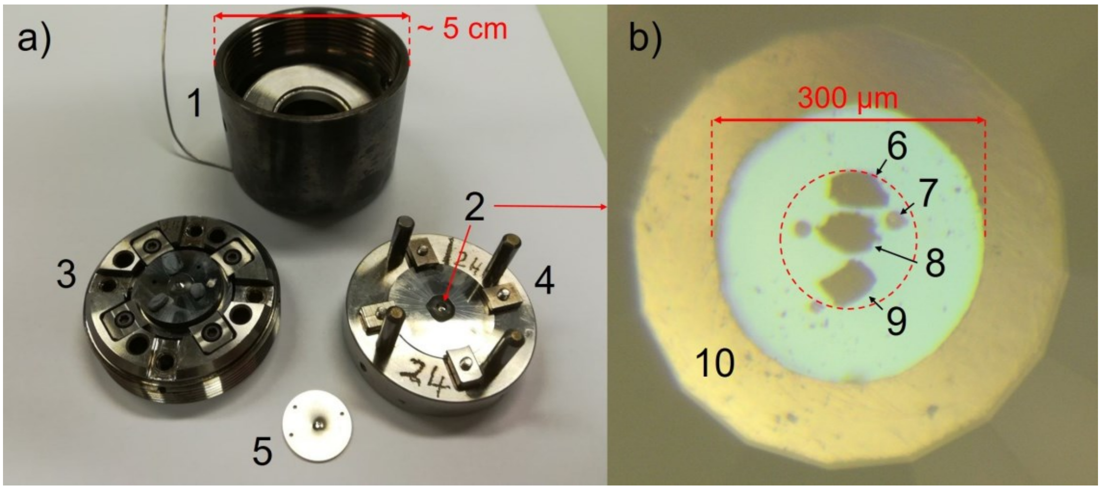

Fig. 2.2: a) Components of the diamond anvil cell: 1. He membrane pod, 2. Top diamond anvil, 3. Bottom anvil support, 4. Top anvil support, 5. Indented steel gasket. b) Sample space on top of the diamond anvil: 6. $Sm_2Ir_2O_7$ single crystal, 7. ruby (two more on the left, next to the samples), 8. $Pr_2Ir_2O_7$ powder, 9. $Er_2Ir_2O_7$ single crystal, 10. Steel gasket. The smaller red dotted circle (d = 150 µm) represents the predicted compressed sample space from d = 300 µm after the application of 20 GPa of pressure.

2.5 Synchrotron radiation experiments

Synchrotron radiation, although in principle very similar to laboratory X-ray radiation, has numerous advantages in comparison. It is horizontally polarised and has a continuous spectrum, which enables the possibility of adjusting the energy/wavelength and also controlling the polarisation. At the same time, its brilliance is orders of magnitude larger (more than a billion times in some cases). Brilliance describes both the intensity (brightness) and the angular spread of the beam. As a result, even a common powder diffraction on a synchrotron is much faster and more precise than high-quality laboratory X-ray diffraction. All in all, combined with the ability to tune the wavelength and polarisation, the enormous brilliance of the beam enables scientists to perform much more complex experiments, which would be either impossible or take too much time on any laboratory X-ray source. Of course, synchrotron radiation has one major disadvantage – it is much more expensive than laboratory X-ray sources.

Similarly to neutron sources or free electron lasers, synchrotrons are large-scale facilities. In order to measure there, one must propose an excellent experiment which is accepted by the scientific committee and awarded the measurement time. The whole process usually takes more than half a year. In this work, we present results from four synchrotron experiments, measured at three large-scale facilities, the European Synchrotron Radiation Facility (ESRF) (Grenoble, France), Bessy II (Berlin, Germany), and Diamond (Didcot, United Kingdom).

2.5.1 Temperature-dependent diffraction

In order to study subtle changes in the crystal structure, temperature-dependent powder diffraction was done on the KMC-2 beamline [60] at Bessy II and the ID22 beamline [61] at ESRF. Temperatures from 300 K down to 25 K (KMC-2) and 4 K (ID22) were measured. For example, on ID22, the diffracted photons were detected using a multianalyser stage (Fig. 2.3); with nine separate analyser crystals, the background noise was drastically suppressed. The instrumental contribution to the FWHM is only around 0.003° in 2θ (referential peaks from LaB_6 measured with FWHM ≈ 0.005°). Moreover, a higher-energy beam, 0.354 Å on ID22 and 1.127 Å on KMC-2, pushes diffraction peaks to lower angles, i.e., more diffraction peaks can be measured using the same angular region. A diffraction pattern with a higher resolution than the laboratory XRD can be collected in under one minute. In the case of ID22, a high-resolution scan with a range of 10-50 degrees was made in ~6 minutes; in the case of KMC-2, a high-resolution scan with a range of 5-80 degrees was made in approximately half an hour.

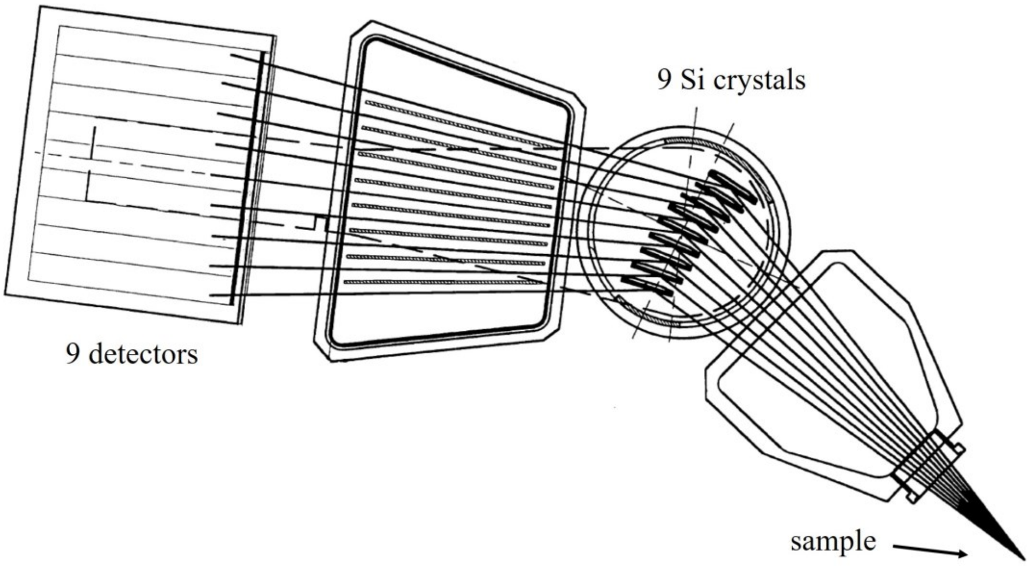

Fig. 2.3: Schematic picture of the multianalyser stage used on ID22 at ESRF [62].

2.5.2 Diffraction under pressure

Powder and single-crystal diffraction under high pressure was done utilising DACs. The combination of highly focused synchrotron beam and transparent diamonds is currently the best option for studying structure at high (static) pressures. Two such experiments were done within this work, one on the beamline ID15b at ESRF [63] and the second on the beamline I15 at Diamond [64]. Both beamlines specialise in experiments with DACs and routinely rent several types to users during the measurement time.

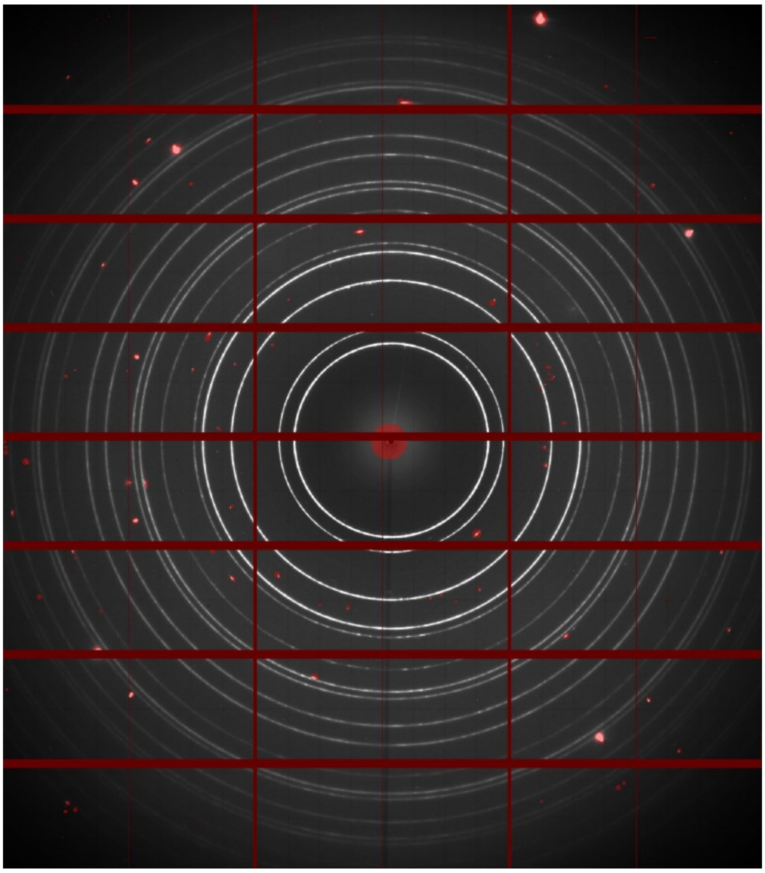

Fig. 2.4: 2D diffractogram of powder $Lu_2Ir_2O_7$ at ~20.5 GPa (I15, Diamond) analysed in the Dioptas software. Firstly, detector calibration is implemented. Afterwards, all reflections from the diamond anvil (big spots), solidified helium (tiny spots), and dead pixels, are manually masked (indicated by the red colour). Lastly, diffraction rings are integrated into a 1D diffraction pattern for further analysis.

More important than intensity or variable wavelength in this case is the small beam size. Even though it is possible to perform experiments with DACs and laboratory X-rays, the beam is normally big enough to diffract from the whole sample space, even the gasket around it. In contrast, the synchrotron beam can be extremely focused, e.g., down to 5x5 μm^2 on ID15b (see the experimental arrangement in Fig. 2.5). This means there is no diffraction from the gasket or rubies, only from a very

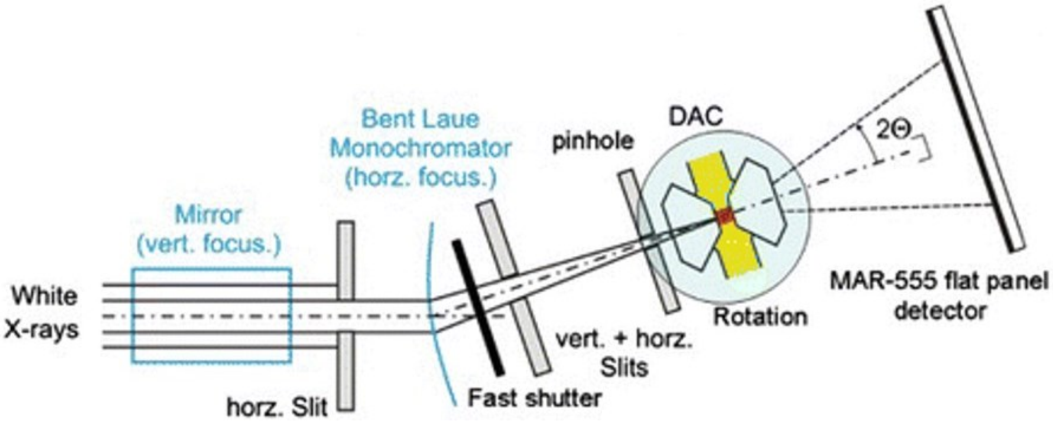

Fig. 2.5: Experimental arrangement of the ID15b beamline. Extremely high focus of the beam enables diffraction from only specific parts of the sample space (beam spot down to 5x5 μm) inside the diamond anvil cell. Diffracted signal is gathered using a 2D detector. Illustration adopted from [63].

small and well-defined portion of the sample (and, of course, the diamond anvils). Moreover, the inhomogeneous distribution of quasi-hydrostatic pressure (Fig. 1.3) is not affecting the measured diffraction as much, and there is a possibility of loading multiple samples in one pressure cell (Fig. 2.2b). On the other hand, an extremely focused beam reduces the statistics of powder diffraction, as only limited amount of grains is in the beam. Another general inconvenience of DAC experiments is that the angular range of the high-pressure diffraction is greatly limited by the window in the pressure cell (only up to ~43 degrees in 2θ during our experiment at ID15b and ~37 degrees at I15). Therefore, it is very important to have a high-energy beam in order to detect as many diffraction peaks as possible within this limited angle. On ID15b, the wavelength was ~0.41 Å (30 keV), and on I15, it was ~0.35 Å (35 keV). After the data acquisition by a 2D detector, the powder-diffraction data is masked and integrated using the Dioptas software [65] (Fig. 2.4). The single-crystal-diffraction data are analysed as described in the Section *2.2.3 Single crystal diffraction*.

3. Previous results

$A_2B_2O_7$ oxides, where A is a rare earth and B is a transition metal, have been studied extensively in the recent years due to their complex electron ground states and emerging novel phases [3,4]. In the present section, we focus on summarising the most relevant previous results on $A_2Ir_2O_7$ iridates. Most previous studies were aimed at the lighter part of the rare-earth series (A = Pr – Eu), particularly at $Eu_2Ir_2O_7$ with nonmagnetic Eu^{3+}. In comparison, previous results on heavy-rare-earth iridates, the focus on this study, are lacking, especially on single crystals.

3.1 Crystal structure of $A_2Ir_2O_7$ iridates

$A_2B_2O_7$ oxides stabilise frequently in the so-called pyrochlore structure (cubic structure, space group $Fd\bar{3}m$, 227). There exists a region of stability for the pyrochlore structure based on the ratio of the atomic radii of A and B, $1.36 \leq r_A/r_B \leq 1.71$ [3]. Employing high-pressure synthesis, metastable pyrochlore oxides can be prepared with r_A/r_B up to ~2.30 [66]. Leaving the stability region results often in a disordered defect-fluorite structure (cubic, space group $Fm\bar{3}m$, 225) or sometimes a completely different orthorhombic or monoclinic structure [3,66]. That is, having A and B atoms of more similar size promotes their mixing and disorder in the system. Borderline examples are, e.g. B = Zr or Hf families, where lighter-rare-earth members (A = La – Gd) crystallise in the pyrochlore structure, but heavier-rare-earth members with

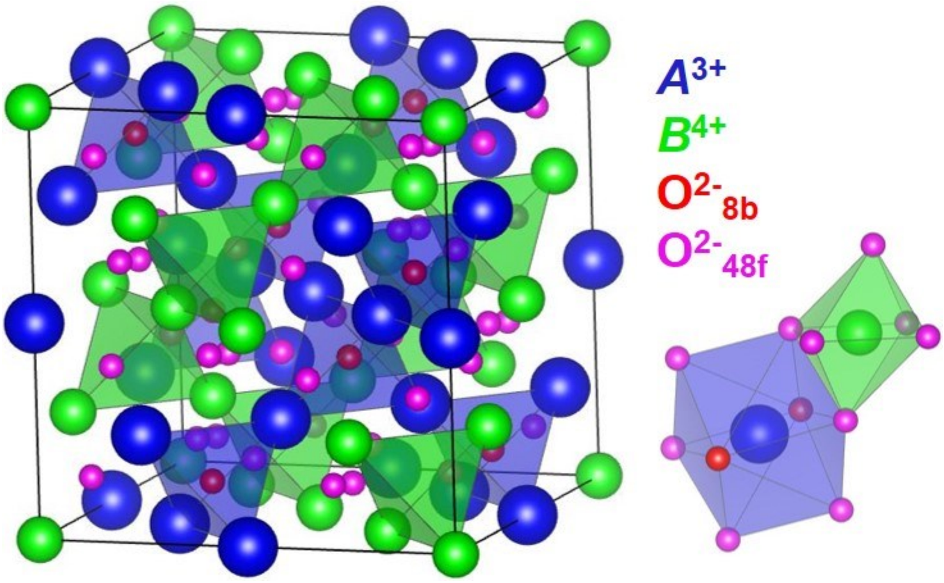

Fig. 3.1: Illustration of the elementary unit cell of the pyrochlore structure. The local environment of the A^{3+} and B^{4+} cations are characterised by the distorted cubic and octahedral oxygen cages, respectively. The free oxygen parameter x_{48f} dictates the distortion of the oxygen cages. Images were generated employing the freely available VESTA software [67].

a smaller atomic radius tend to adopt the defect-fluorite structure [66,68]. $A_2Ir_2O_7$ iridates crystallise in the pyrochlore structure across the whole rare-earth series (A = Pr – Lu) [3,66]. A = La, Ce members have not been reported so far.

In the pyrochlore structure, as seen in Fig. 3.1, the A^{3+} and B^{4+} cations separately form two interpenetrating sublattices of corner-sharing tetrahedra, each consisting of only the respective cations [4]. The positions of the cations are fixed by the symmetry of the structure, i.e., 16*d* position (1/2, 1/2, 1/2) for A^{3+} and 16*c* position (0, 0, 0) for B^{4+}. As discussed in Section *1.3 Geometrical frustration*, a lattice with magnetic moments situated on the vertices of tetrahedra is prone to exhibit geometrical frustration and related complex states. A^{3+} and B^{4+} cations are surrounded by distorted cubic and octahedral oxygen cages, respectively. The Wyckoff positions of the O^{2-} anions are 8*b* position (3/8, 3/8, 3/8) and 48*f* position (x_{48f}, 1/8, 1/8). The free fractional coordinate x_{48f} dictates the distortion of the oxygen cages. $x_{48f} = 0.3125$ leads to a perfect octahedral cage around each B^{4+} cation, while $x_{48f} = 0.375$ would mean a perfect cubic cage around each A^{3+} cation. Empirically, the value of x_{48f} in $A_2B_2O_7$ oxides tends to reach the value in a range of 0.320–0.345, distorting local oxygen environments of both cations [3]. Importantly, the distortion affects the B-O-B bond angle as well as the B-O bond length; both are important for the understanding of the magnetic and electrical transport properties [69]. All in all, the pyrochlore structure of the $A_2B_2O_7$ oxides can be fully described by only two structural parameters: the cubic lattice parameter a and the fractional coordinate of oxygen x_{48f}.

3.2 Electrical transport and magnetic properties

Complex and frequently exotic phenomena observed in the $A_2Ir_2O_7$ iridates stem from the interplay between electron correlations, strong spin-orbit coupling, and magnetic exchange interactions on the geometrically frustrated lattice. Based on the temperature regions, we can distinguish between very low temperatures, where the magnetic properties are dictated mostly by the rare-earth magnetism (except for cases of nonmagnetic A^{3+}, e.g. Eu or Lu), and intermediately low temperatures (~100 K), where weaker Ir^{4+} magnetism has pronounced effects on the properties. Of course, both A^{3+} and Ir^{4+} magnetism still affect the properties in the temperature regions they are not dominant in, e.g. CEF effects of A^{3+} ions at intermediately low temperatures. The Ir^{4+} sublattice orders antiferromagneticaly in the so-called all-in-all-out (AIAO; and equi-energy AOAI) order. That is, magnetic moments point along local <111> directions of the tetrahedra. The Néel temperature T_{Ir} depends seemingly on the size of the A^{3+} cation rather than its magnetic moment [55] (see Fig. 3.2). At/below the same temperature, $A_2Ir_2O_7$ undergoe a metal-insulator transition (characterised by T_{MI}) for light-rare-earth members and rather a semiconductor-insulator transition moving to the heavy-rare-earth members [32] (Fig. 3.3). As for the rare-earth magnetism at very low temperatures, it varies significantly with the rare-earth element. For example, the emergence of a chiral spin liquid state below 1.5 K in $Pr_2Ir_2O_7$ [70], a long-range AIAO order of Tb cations in $Tb_2Ir_2O_7$ [9,71], or a fragmented spin ice state in $Ho_2Ir_2O_7$ [2,72].

The $A_2Ir_2O_7$ iridates remain in the pyrochlore structure when cooled down through T_{Ir}. In a few studies (mostly lighter A members), the pyrochlore structure was followed to very low temperatures, with no signs of a structural transformation [e.g. 9,73,74]. However, very recently, there have been reports of an isostructural transition around T_{Ir} for $Eu_2Ir_2O_7$ upon cooling [69] or for $Sm_2Ir_2O_7$ upon the application of external pressure [75]. That is, although the pyrochlore structure remained stable and no anomaly was observed in the evolution of the lattice parameter, there was a small anomaly seen in x_{48f} evolution, dictating the distortion of the local oxygen cages. The importance of the local structure in regard to the magnetic and electrical transport properties of $A_2Ir_2O_7$ was also highlighted by the studies of polarisation-resolved Raman scattering. That is, in $Eu_2Ir_2O_7$, the Ir-O-Ir bond-bending vibration exhibited softening and line-shape anomalies around T_{Ir} [76].

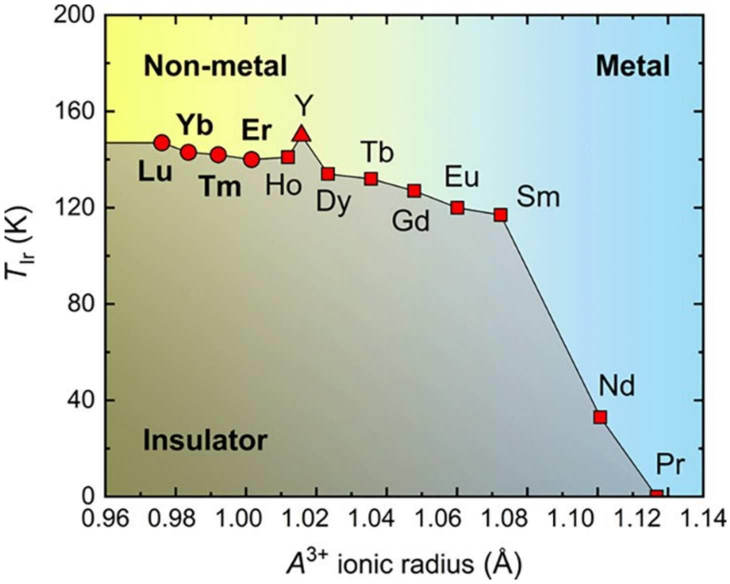

Fig. 3.2: Phase diagram of the $A_2Ir_2O_7$ iridates adapted from [55]. The AFM transition temperature T_{Ir} increases for heavy-rare-earth members. Approximately on the same border, there exists a (non-)metal-insulator transition.

Electrical transport properties are characterised mainly by the metal-insulator (or semiconductor-insulator) transition happening at/below the AFM ordering temperature T_{Ir}. The temperature evolution of electrical resistivity of mainly light-rare-earth analogues is presented in Fig. 3.3. The electrical resistivity can easily rise by more than four orders of magnitude in the insulating state below T_{MI}. A = Pr analogue is the only one in the rare-earth series exhibiting no metal-insulator transition (and no magnetic ordering) [5,32]. Moving to the heavier-rare-earth members, the high-temperature metallic phase evolves into a semiconducting one. Simultaneously, the transition into the insulating state becomes smoother, only discernible on a log-log scale for A = Dy and Ho members in Fig. 3.3. Overall, the electrical transport properties are significantly dependent on the sample preparation and stoichiometry

[32,77,78,79,80]. Striking differences can normally be seen when comparing polycrystalline and single-crystal samples [81,82,83]. For example, the relative change $\rho_{2\mathrm{K}}/\rho_{300\mathrm{K}}$ between low temperature and room temperature resistivity in $\mathrm{Eu_2Ir_2O_7}$ can range from less than two orders of magnitude [79,80] to more than five orders of magnitude [32,82].

Electrical resistivity of the material can be tuned by chemical substitution (chemical pressure). Substituting Ir for Ru in $\mathrm{Eu_2Ir_2O_7}$ had a negligible effect on T_{Ir}, but the electrical transport properties changed significantly, shifting the metal-insulator transition to lower temperatures [79]. The substitution of the rare-earth Eu, e.g. for Sr (hole doping), shifted both T_{Ir} and T_{MI} to lower temperatures, with both anomalies no longer bound to approximately the same temperature [80]. Eu-Bi substitution revealed an anomalous lattice contraction, while both T_{Ir} and T_{MI} decreased together with the increasing Bi content [84]. In comparison, the application of external pressure is a clean way of tuning the structure without adding disorder. It generally introduces more conducting properties in the $A_2\mathrm{Ir_2O_7}$ iridates. In $\mathrm{Nd_2Ir_2O_7}$, the insulating state was monotonously suppressed with the application of pressure [85,86]; a metallic state was reached with 10 GPa of pressure [85]. For $\mathrm{Eu_2Ir_2O_7}$, the application of pressure continuously closed the insulating gap at around ~6 GPa, crossing over to a metallic state with a negative temperature coefficient of electrical resistivity [83].

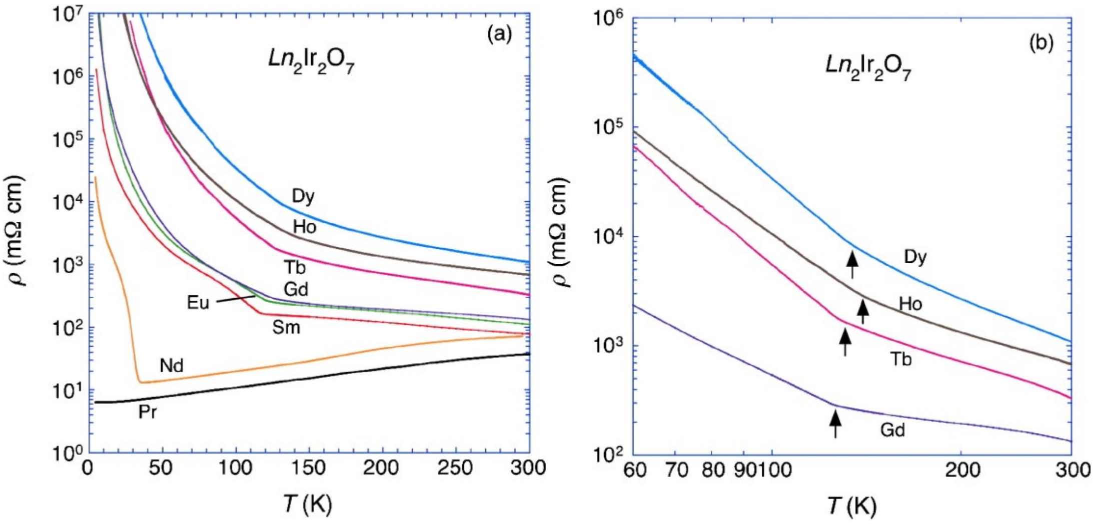

Fig. 3.3: Temperature evolution of the electrical resistivity of several $A_2\mathrm{Ir_2O_7}$ members (A = Pr – Ho), adopted from [32] ($Ln = A$ in a different notation).

The magnetotransport properties of the $A_2\mathrm{Ir_2O_7}$ iridates characterise not only the electrical transport, but also provide insight into the AFM structure of the Ir sublattice inside the insulating phase. In $\mathrm{Ho_2Ir_2O_7}$ single crystal, magnetoresistivity (MR) was observed to be highly anisotropic; a hysteresis was revealed along the [111] direction, described by the influence of Ho monopole density [2]. Measurements of

$Nd_2Ir_2O_7$ revealed not only an anisotropy and a hysteresis, but also large changes of resistivity with field application, attributed to conductive domain walls inside the insulating bulk [87,88]. Very recently, high-pressure MR of $Sm_2Ir_2O_7$ has been employed to map the region around the quantum critical point at ~6.3 GPa [89]. Finally, studies of $Eu_2Ir_2O_7$ revealed a linear asymmetric term in MR dependent on the cooling field and robust up to 15 T [90,91,92,93].

The AIAO AFM ordering of the Ir sublattice was previously confirmed in multiple $A_2Ir_2O_7$ iridates (A = Nd, Sm, Eu, Tb, Yb, Lu) employing neutron diffraction, resonant X-ray diffraction (RXD), or Raman scattering [9,10,74,76,94,95]. The ordering temperature T_{Ir} is typically determined also by simple magnetisation measurements. The temperature dependence of magnetisation in $A_2Ir_2O_7$ is accompanied by a bifurcation between zero-field-cooled (ZFC) and field-cooled (FC) regimens at T_{Ir} [e.g. 32,55,96]. The magnitude of the bifurcation decreased in off-stoichiometric samples [81,92]; the feature is seemingly not created by defects in the crystal lattice (from disorder). In most studies, T_{Ir} determined from magnetisation corresponds to the T_{MI} determined from electrical resistivity. Furthermore, a broad anomaly in specific heat can be tracked around the same temperature as well [13,55,97,98]. In a few studies, the isothermal magnetisation revealed a small hysteresis [19,99,100], which is generally a sign of a small ferromagnetic (FM) contribution. Moreover, cooling some $A_2Ir_2O_7$ iridates in magnetic field produced a small but robust remanent magnetisation, which shifted the whole isothermal magnetisation curve [92,100,101].

One of the explanations for the presence of a small FM contribution inside the bulk AFM state is the domain wall model. The domain structure consisting of AIAO and AOAI domains must contain domain walls (DWs), which were speculated to contain uncompensated magnetic moments (resulting in the FM contribution) [102]. This can also explain the linear asymmetric term in MR. As asymmetric MR should always turn symmetric in a high enough magnetic field, one of the explanations for the asymmetric term lies in the FM domain walls pinned by the AIAO AFM domain structure [92]. Such a feature is similar to the exchange bias effect in conventional FM/AFM exchange-coupled systems [103,104]. An alternative explanation was reported by Fujita et al. [91,105]. The asymmetric MR was explained by different hopping probability of AIAO- and AOAI-type domains in applied magnetic field, based on the double-exchange model. In $Nd_2Ir_2O_7$, the DWs have much higher electrical conductivity than the bulk; the domain structure was mapped with spatially resolved microwave impedance microscopy [106]. In an isostructural compound $Cd_2Os_2O_7$ (also with the same AIAO order), the domain structure was directly observed with resonant magnetic microdiffraction [107]. The size of the domains in $Eu_2Ir_2O_7$ thin films was studied by MR employing microscale Hall bars [108]. In the above cases, the domain structure could be controlled by the application of a cooling magnetic field.

The understudied heavy-rare-earth part of the $A_2Ir_2O_7$ series (compared to the lighter-A members) exhibits vastly different transport properties while retaining similarities in the nature of the electrical and magnetic anomalies. It is interesting to also probe the semiconducting and highly insulating behaviour in the heavy-rare-earth members. Moreover, some of these members have significantly higher magnetic moments of the A^{3+} ions, resulting in intriguing low-temperature properties. The true nature of the bifurcation in magnetisation, asymmetric MR, or the hidden FM component remains unclear. Although a few high-pressure experiments on the light-A analogues exist, the systematics of the local pyrochlore structure with varying A or the application of pressure is missing. That is, structural information can help interpret both already published and future high-pressure data, especially since the anomalies are seemingly connected to the local distortion of the structure (Ir-O-Ir bond angle). In this work, we strive to understand or at least bring more insight into these presented topics.

4. Results

4.1 Synthesis and characterisation

4.1.1 Polycrystalline samples

The CsCl flux method was employed to synthesise the polycrystalline $A_2Ir_2O_7$ samples. Initial A_2O_3 and IrO_2 oxides with high purity (99.99% metal basis, Alfa Aesar) were mixed with the CsCl flux (99.999%, Thermo Scientific). A ratio of $A_2O_3/IrO_2/CsCl = 1:2:50$ was used. The mixture was reacted repeatedly (6-9 cycles) in a platinum crucible at approximately 800 °C. Afterward, the residual salt was washed out of the mixture with distilled water. A detailed description of the synthesis was published by my colleague [109] who did most of the work developing the sample synthesis process and grew most of the samples studied in this work. Small clusters of single crystals were prepared (~10x10x10 μm^3 dimensions) with clear facets visible using the SEM. However, the crystals were far too small for single-crystal measurements; therefore, they were crushed into fine powder for polycrystalline measurements. In the case of electrical resistivity measurements, they were cold-pressed into pellets with approximately 2 kbar of pressure, as seen in Fig. 4.15.

The stoichiometry of the powder was checked using the EDX technique. Although the A:Ir = 50(2):50(2) stoichiometric ratio was confirmed on average, there have been observations of Ir-deficient (a few %) spots on the samples. Detailed quantitative analysis using EDX was difficult due to the sample being a powder and a bad conductor. The crystal structure of the samples was checked by XRD measurements using a laboratory X-ray source. An example of the diffraction pattern of $Lu_2Ir_2O_7$ is presented in Fig. 4.1. The Rietveld model agrees very well with the pyrochlore structure. Most of the synthesised samples contained minority phases of the precursor oxides A_2O_3, IrO_2, and pure iridium, which is typical for these materials [74,79,100]. These minority peaks are hardly seen in the pattern in Fig. 4.1 (within 1% of molar weight), although different samples had different quantities of the minority phases. Moreover, the slightly asymmetrical shape of the peaks can be discerned from the pattern, seen on the difference curve. See Section *4.2 Robustness of the pyrochlore structure in A2Ir2O7* and Fig. 4.6 with our synchrotron data for further details.

The structural parameters of the $A_2Ir_2O_7$ iridates vary systematically with the atomic number of A. Moving from light rare earths to heavy ones, the pyrochlore lattice contracts as the atomic radius of A shrinks. This is followed in the summary of structural parameters in Table 4.1. The second free structural parameter x_{48f} seems to increase with the atomic number of A ($Lu_2Ir_2O_7$ has the most distorted oxygen cages around Ir). However, the laboratory XRD is not precise enough to display this evolution smoothly. The Ir-O-Ir bond angle φ is solely dependent on x_{48f}, while the Ir-O bond length d is dependent on both a and x_{48f}.

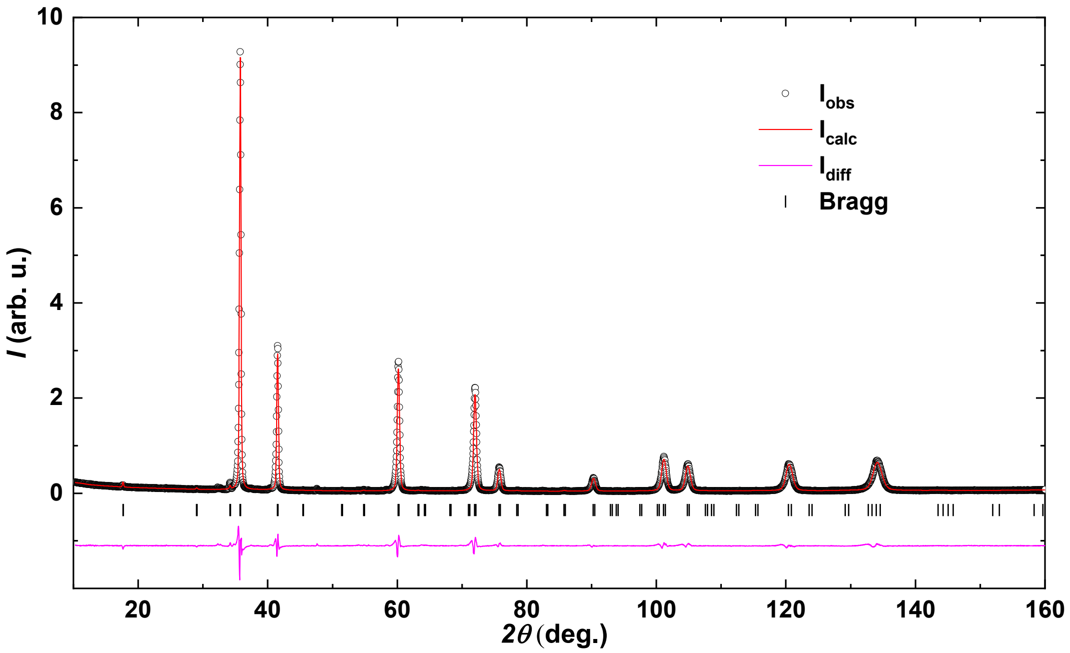

Fig. 4.1: Powder X-ray diffraction pattern of the $Lu_2Ir_2O_7$ sample. The pink line illustrates the difference between the measured data (black circles) and modelled data (red line). The predicted peak positions of the pyrochlore structure are also shown. Data published in [110]. Few small peaks indicate a secondary Ir phase.

Table 4.1: Structural parameters of polycrystalline $A_2Ir_2O_7$ iridates with A = Dy – Lu determined by laboratory X-ray diffraction. The pyrochlore structure ($Fd\bar{3}m$) is fully characterised by the lattice parameter a and the fractional coordinate of oxygen x_{48f}. The rest of the parameters are calculated from a and x_{48f}, including the volume V, Ir-O-Ir bond angle φ, and Ir-O bond length d. Statistical refinement errors are shown in the brackets. Data published in [110].

A	a (Å)	V (Å^3)	x_{48f}	φ (deg.)	d (Å)
Dy	10.192(2)	1058.7(6)	0.334(2)	129(1)	1.995(9)
Ho	10.184(1)	1056.2(3)	0.335(2)	129(1)	1.997(9)
Er	10.162(1)	1049.4(3)	0.334(2)	129(1)	1.989(9)
Tm	10.135(1)	1041.1(3)	0.337(2)	128(1)	1.997(9)
Yb	10.108(2)	1032.8(6)	0.336(2)	128(1)	1.987(9)
Lu	10.104(1)	1031.5(3)	0.340(3)	126(1)	2.004(9)

4.1.2 Single crystals

The flux method was used for the synthesis of single crystals as well, but this time, PbF_2 (99.997% metal basis, Thermo Scientific) was used as flux. Reaction cycles were performed at ~1100°C in air. The grown crystals with approximate dimensions up to 0.5x0.5x0.5 mm^3 had an octahedral (bipyramidal) shape with smooth and shiny facets.

Examples of the grown crystals are presented as BE images in Fig. 4.2a-b. Although more members of the $A_2Ir_2O_7$ series have been synthesised in our group, only A = Er and Lu members have been studied in this work. These analogues were not reported to be synthetised as single crystals by any other group. The crystals were just large enough for Laue diffraction, which was used to confirm their single-crystallinity. It also confirmed that the triangular facets of the octahedron are perpendicular to the <111> crystallographic directions. Such an orientation is not surprising, since the octahedron has the same symmetry as a cube. That is, eight vertices of a cube are equivalent to eight faces of an octahedron. Similarly, it was confirmed that the octahedron vertices point to the <100> directions (connecting two opposite vertices through the middle). Finally, the opposite edges are connected along the <110> directions (again through the middle of the crystal). An example of a Lauegram is shown in Fig. 4.2c. While the $Er_2Ir_2O_7$ samples often had clear vertices, the $Lu_2Ir_2O_7$ samples tended to show cut-out vertices in the form of rectangle facets (see Fig. 4.2b). That is, in the latter case, the crystal also did not grow with the same speed along all directions (rectangular facets instead of symmetric square facets, or small edges instead of a vertex).

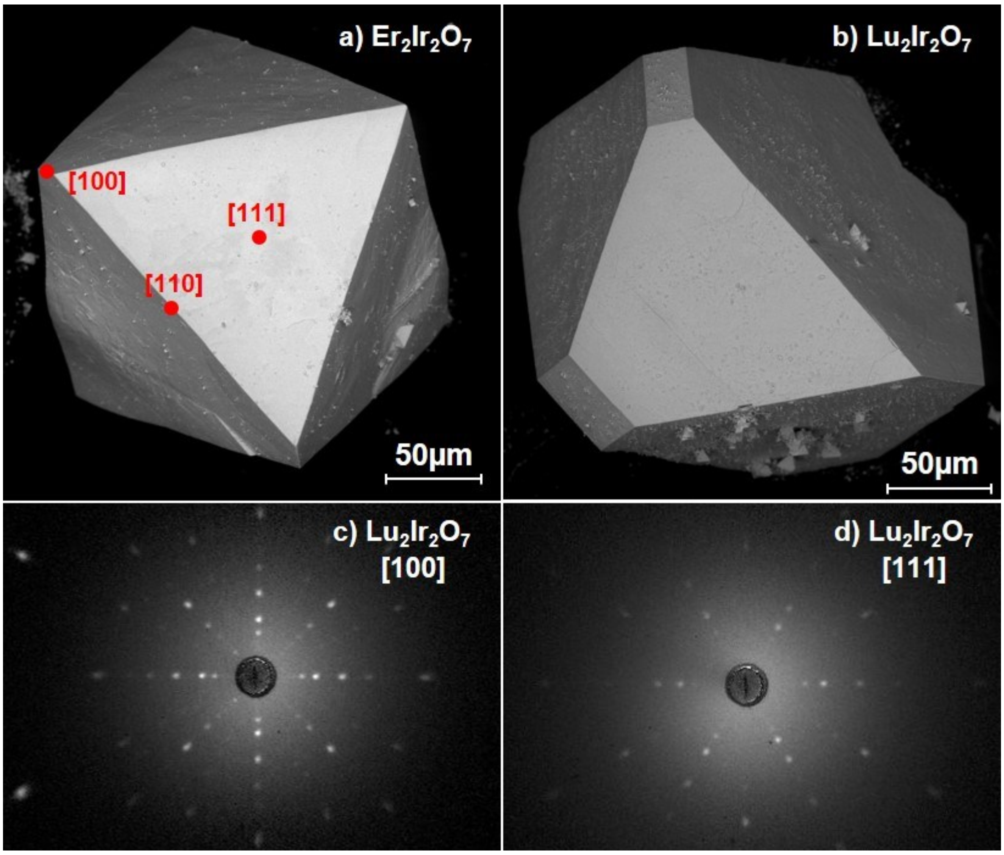

Fig. 4.2: Backscattered-electron (BSE) images of a) $Er_2Ir_2O_7$ and b) $Lu_2Ir_2O_7$ single crystals. As illustrated, the main crystallographic axes are easily determined based on the clear facets (see the text). Lauegrams of a $Lu_2Ir_2O_7$ single crystal along the c) [100] and d) [111] crystallographic axis. The four-fold and tree-fold rotation symmetry is revealed, respectively. Images partly published in [111].

The EDX mapping of the sample surface mostly confirmed the stoichiometry of the synthesised single crystals. However, unlike the case of the CsCl flux, the lead from the PbF_2 flux unfortunately had a tendency to mix into the pyrochlore phase. This was not apparent at first because A = Er crystals had no lead on the surface. A = Lu members showed traces of Pb on the surface, which led to an extensive investigation of the composition under the surface. It was discovered that the minority lead atoms are present under the surface of all synthesised members, including the A = Er samples (only seen after polishing the samples). The composition of Pb was not homogeneous, ranging from a few percent up to 20 %, depending on the growing conditions of the sample. The Pb atoms do not mix with the Ir atoms, only with the A atoms, which is understandable based on the similar radius of Pb and A atoms. This is also evident from how the composition of Ir was approximately the same on a wide area of a sample while the composition of A lowered in places where the Pb composition was higher, and vice versa. This is nicely illustrated by the 2D EDX maps done on an A = Lu sample in Fig. 4.3. It is clear that the Ir composition is homogeneous, unlike the A:Pb ratio. Simultaneously, a slight Ir deficiency was observed (averaging from multiple samples), with an approximate ratio (A + Pb):Ir = 51(2):49(2).

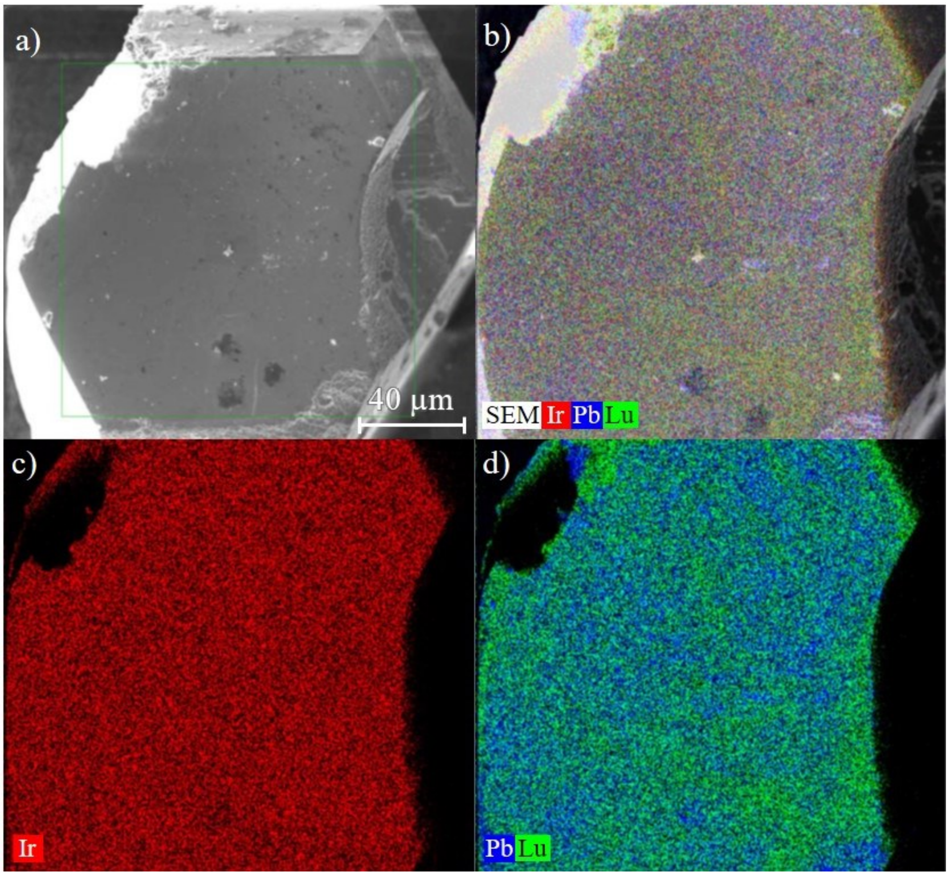

Fig. 4.3: BSE images and 2D EDX scans of a $Lu_2Ir_2O_7$ single crystal done on a SEM. a) BSE image with the illustration of the area scanned with the EDX. b) 2D EDX scan of Lu, Pb, and Ir, interlapping with the BSE image. c) 2D EDX scan of only Ir composition and d) only Lu and Pb composition. The Ir composition is homogenous, unlike the Lu and Pb composition. Images published in [111].

The structure of the single crystals was confirmed to be pyrochlore by single crystal diffraction on $Er_2Ir_2O_7$ and $Lu_2Ir_2O_7$ samples of dimensions 0.13×0.10×0.03 mm^3 and 0.13×0.07×0.04 mm^3, respectively. No significant deviations were observed when refining the occupancy factors of *A* and Ir positions. Therefore, they were fixed to full occupancy. Mixed occupancy (substitution by Pb atoms) was also tried on both *A* and Ir positions. These attempts resulted, however, in worse refinement factors, thus, no mixing of Pb atoms into the lattice was used in the final model. Lattice parameters a = 10.1626(1) Å for $Er_2Ir_2O_7$ and a = 10.1215(1) Å for $Lu_2Ir_2O_7$ were determined. The refined atomic positions and the equivalent isotropic displacement parameters are shown in Table 4.2. Both a and x_{48f} parameters correspond well to the parameters determined for the powder samples; although, slightly larger a is observed for the Lu single crystal compared to powder.

Table 4.2: Atomic positions and equivalent isotropic displacement parameters U_{eq} of $Er_2Ir_2O_7$ and $Lu_2Ir_2O_7$ single crystals determined by single-crystal XRD. Data published in [111].

Atom	Wyckoff position	x	y	z	U_{eq} (Å^2)
Er	16*d*	0.5	0.5	0.5	0.0038(1)
Ir	16*c*	0	0	0	0.0045(1)
O1	8*b*	0.375	0.375	0.375	0.011(2)
$O2_{Er}$	48*f*	0.332(3)	0.125	0.125	0.045(4)
Lu	16*d*	0.5	0.5	0.5	0.0019(2)
Ir	16*c*	0	0	0	0.0021(3)
O1	8*b*	0.375	0.375	0.375	0.056(3)
$O2_{Lu}$	48*f*	0.338(6)	0.125	0.125	0.023(6)

4.2 Robustness of the pyrochlore structure in $A_2Ir_2O_7$

The stability of the crystal structure within the $A_2Ir_2O_7$ series was studied using synchrotron radiation. Four powder XRD experiments were performed (for experimental details, see Section *2.5 Synchrotron radiation experiments*). The first subsection is dedicated to the temperature-dependent structural properties and the second one deals with the application of external pressure on the pyrochlore structure. Together, the structural properties pave the way towards a deeper understanding of later-presented magnetic and transport properties.

4.2.1 Thermal evolution of the crystal lattice

Two temperature-dependent synchrotron XRD measurements were performed. One on the ID22 beamline at ESRF, France, and the other on the KMC-2 beamline at Bessy II, Germany. The collected diffraction patterns are shown in Fig. 4.4 and Fig. 4.5. The Rietveld refinement of the diffraction data confirms the $A_2Ir_2O_7$ iridates crystallising in the pyrochlore structure t ($Fd\bar{3}m$). In some cases, small peaks from the IrO_2 or A_2O_3 minority phases can be seen in the high-resolution diffraction patterns (only at the low angles). They were modelled as follows: IrO_2 with the tetragonal $P42/mnm$ space group (n. 136) [112], Pr_2O_3 with the trigonal $P\bar{3}m1$ space group (n. 164) [113], and A_2O_3 (A = Sm, Dy – Lu) with the cubic $Ia\bar{3}$ space group (n. 206) [114]. Additionally, minority Ir phase (face-centred cubic) can also be characterised by very sharp peaks in the pattern. Although the Ir peaks are relatively tall, they are much narrower than the pyrochlore peaks, resulting in a weight percentage of Ir in the sample well below 1%. All phases could be modelled at ambient temperature and down to low temperatures with the same structural model; i.e., no structural transition has been observed when cooling the samples down to base temperature.

The biggest obstacle of the detailed analysis of the patterns was, however, the peak shape of the studied pyrochlore phase. In all measured samples, the pyrochlore peak shape is asymmetric, which is especially visible in high-resolution diffraction experiments. The examples are shown in Fig. 4.6. The main objective of the analysis was to determine the lattice parameter a and the free coordinate parameter $x_{48\mathrm{f}}$. In order to determine the temperature dependence of $x_{48\mathrm{f}}$, small variations of the intensity must be properly modelled. This requires a very precise fit of the peak shape. For this purpose, we introduced more pyrochlore phases with a slightly shifted lattice parameters. This can be understood as follows: The main stoichiometric pyrochlore phase contributes the majority of the diffraction intensity with a symmetric peak. However, there are small contributions of off-stoichiometric (Ir-deficient) pyrochlore phases which have a slightly inflated lattice due to larger rare-earth atoms mixing in the Ir sublattice. These create small symmetric peaks in slightly smaller 2θ angles than those of the stoichiometric phase, resulting in a broad asymmetric peaks. A similar off-stoichiometric refinement technique was previously employed, for example, in rare-earth $A_2Zr_2O_7$ zirconates [115] or Li-N-H structures [116].

More specifically, we used 11 pyrochlore phases with an equidistantly shifted lattice parameter. The lattice parameter and the corresponding composition of the off-stoichiometric phases was estimated by employing the empirical Vegard's law. That is, A_2O_3 is considered as the 0% Ir occupancy case compared to $A_2Ir_2O_7$ as the 100% Ir occupancy case. As A_2O_3 crystallises in a different cubic structure ($Ia\bar{3}$), this method is only approximative. Ir occupancy from 70% to 100% was modelled (3% step per phase) and the respective models were used for fitting the temperature-dependent diffraction data. As seen in Fig. 4.6, the $Lu_2Ir_2O_7$ sample exhibits only slight asymmetry which could be reasonably described by one off-stoichiometric contribution (91% Ir occupancy). On the other hand, $Sm_2Ir_2O_7$ showed clearly asymmetric peaks which needed many of the off-stoichiometric phases to be active. That is, 11 phases were used in all cases for consistency, but in reality, a number of these off-stoichiometric phases ended up being unused in the refinement (refined to zero or negligible scale factors). All of the pyrochlore phases were restricted to have the same peak shape parameters, temperature displacement factors, and the $x_{48\mathrm{f}}$ parameter. That is, they differed only by a, the Ir occupancy (both set with equidistant steps), and their scale factors. Once a satisfactory refinement was reached on the lowest-temperature pattern, the resulting parameters were used as the starting values for a temperature-dependent sequential refinement. To reduce the overfitting of the model, the ratio of the scale parameters was fixed during the sequential refinement. That is, all eleven pyrochlore phases were tied together and the number of refined parameters was the same as in the case of a single pyrochlore phase refinement.

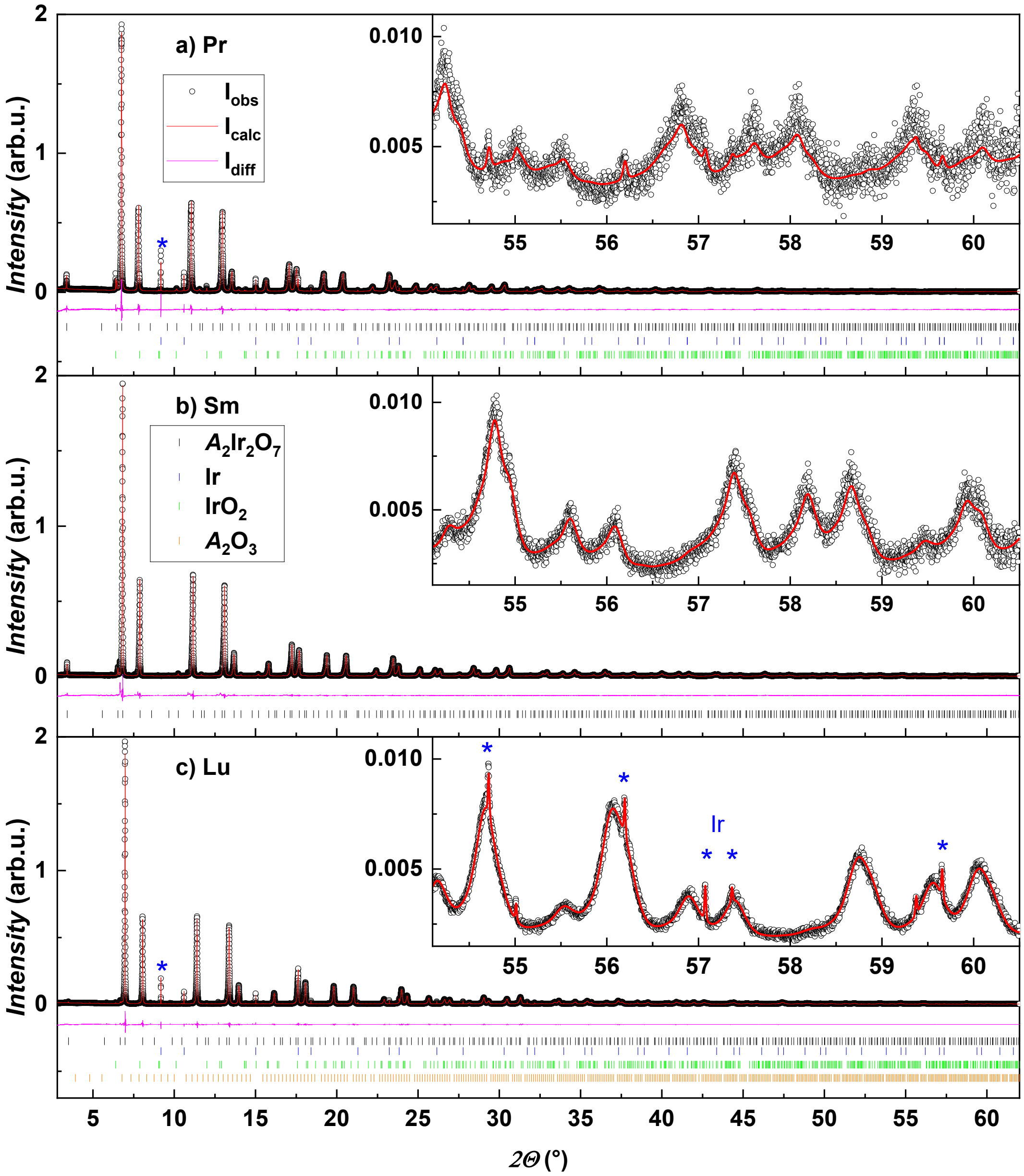

Fig. 4.4: Sychrotron radiation powder diffraction patterns of A = Pr, Sm, and Lu members, measured at 4 K at the ID22 beamline. The insets show the high-angle region of the pattern, showcasing the high resolution of the instrument. In addition to the pyrochlore phase, the minority Ir, IrO_2, or A_2O_3 phases were modelled when necessary (narrow peaks ascribed to the pure Ir minority phase are marked by blue asterisks). The refinements‘ goodness-of-fit values were between 2-3. Data published in [117].

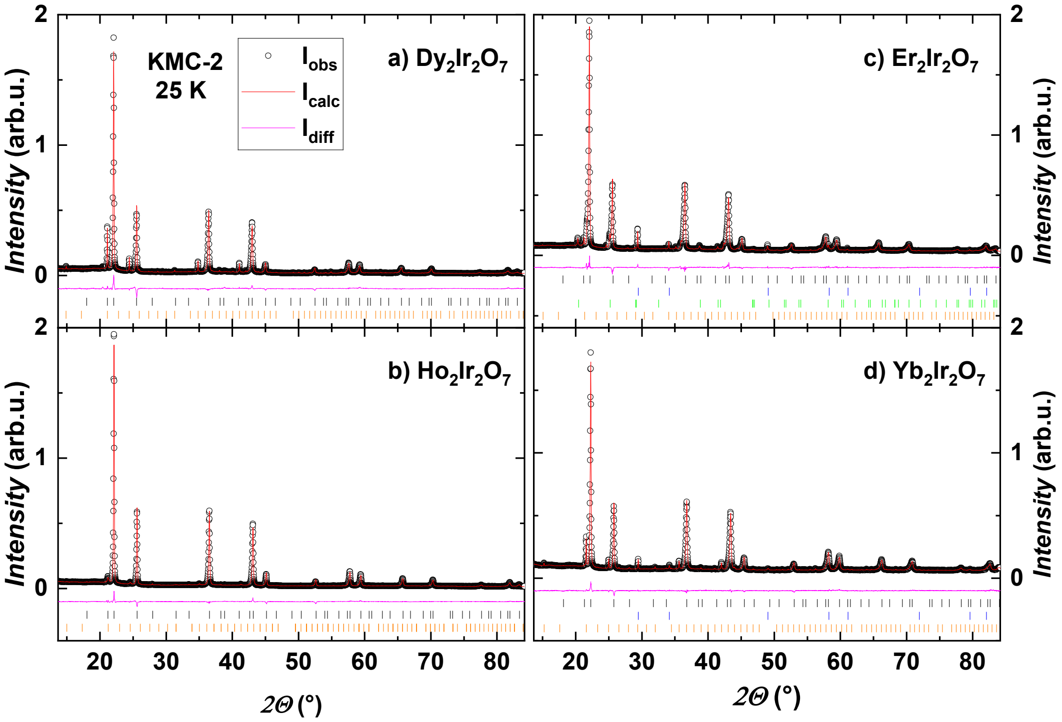

Fig. 4.5: Sychrotron radiation powder diffraction patterns of A = Dy, Ho, Er, and Yb members, measured at 25 K at the KMC-2 beamline. In addition to the pyrochlore phase, the minority Ir, IrO_2, or A_2O_3 phases were modelled when necessary. The refinements' goodness-of-fit values were between 1.5-3. Data published in [117].

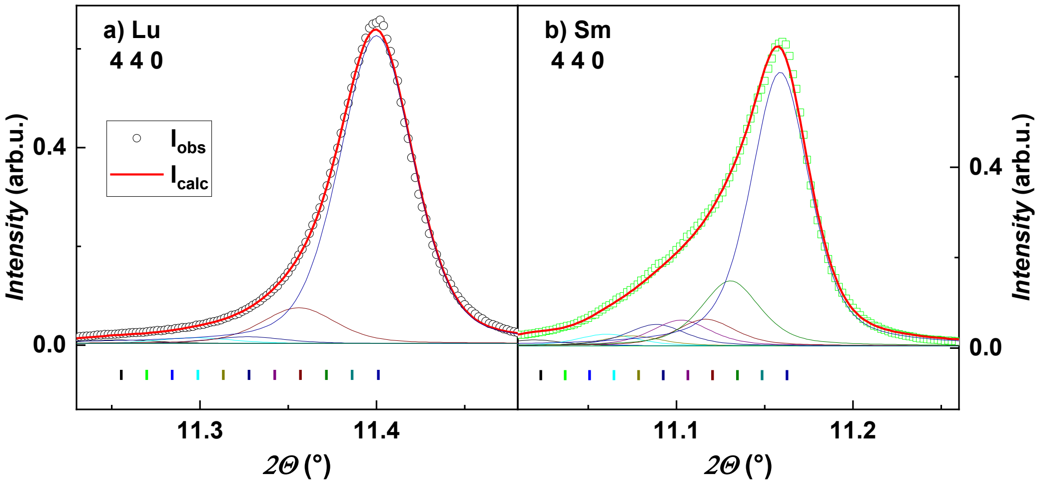

Fig. 4.6: Close-up of the pyrochlore 440 diffraction peak of a) $Lu_2Ir_2O_7$ and b) $Sm_2Ir_2O_7$ samples collected on the ID22 beamline. The asymmetric peak shape is modelled by 11 pyrochlore phases (see the text for details). The positions of the individual phases is described by the coloured ticks. Equivalently coloured lines represent the intensity contribution from each phase. Data published in [117].

Throughout all temperature-dependent structural measurements, no structural transformations have been observed. Ranging several members from A = Pr to Lu, the pyrochlore structure remains stable down to very low temperatures. The sequential refinements result in a temperature dependence of the structural parameters a and $x_{48\mathrm{f}}$. As we focus on the stoichiometric phase for the analysis, the values of the lattice parameter a from the 100% Ir occupancy phase (which contributed the most to the diffraction intensity) are used for further analysis.

Temperature evolution of the lattice parameter was used to calculate the volume compressibility of the $A_2Ir_2O_7$ iridates (see Fig. 4.7). Not only are there no structural transformations observed, the evolution of volume is smooth also around T_{Ir}. That is, no anomaly in the lattice parameter a can be seen around T_{Ir}. We observed an anomaly at 50 K for A = Sm and Lu iridates measured at ID22. Unfortunately, this was caused by the instrument, as the attenuator was used for temperatures below 50 K. The attenuator is routinely used at ID22 to reduce sample heating from the intense synchrotron beam. Unexpectedly, the beam was heating the sample nonnegligibly even above 50 K, which was discovered during the analysis of the data. The compressibility data have been fitted employing the combination of the Debye's model and Grüneisen theory (18). Both the high-temperature and low-temperature regions were modelled following the Thacher's approximate function [45]. More specifically, fitted parameters from the high-temperature region were used for correcting the low-temperature region in the final model. Compressibility can be generally characterised by the thermal expansion coefficient α (equation 15), therefore, it is worth calculating at least its room temperature value. A derivative of the modelled function was employed to determine the room-temperature thermal expansion coefficient $\alpha_{300\mathrm{K}}$. For the case of the A = Sm and Lu members which were not fitted with the Debye's model, the coefficient was estimated from the mean derivative of the data above 240 K, where the thermal changes of the coefficient remain small. We present values connected to volume compressibility, which are not to be mistaken with the lattice parameter compressibility (approximately three times smaller values of α for cubic systems).

Resulting parameters for different rare-earth members, namely zero-temperature volume V_0, Debye temperature θ_{D}, I_V, and thermal expansion coefficient $\alpha_{300\mathrm{K}}$ are presented in Table 4.3. Similarly to the results of the laboratory XRD, the synchrotron experiments confirmed the lanthanide contraction. That is, lattice parameter a decreased monotonously with the increasing atomic number of the rare earth. Compared to the laboratory XRD, results from the KMC-2 and ID22 beamlines have approximately one order and two orders of magnitude smaller error, respectively, due to much better instrumental resolution. The values of the Debye temperature θ_{D} are mostly in the region between 350 K and 400 K, with A = Pr and Ho exhibiting slightly higher values. No systematic evolution of θ_{D} can be reasonably determined. The values of θ_{D} and the lack of systematic evolution correspond well with the previous results on $A_2Ir_2O_7$ iridates determined from the analysis of specific heat [32,98,101,118]. With the knowledge of the isothermal bulk modulus K_0, I_V can be

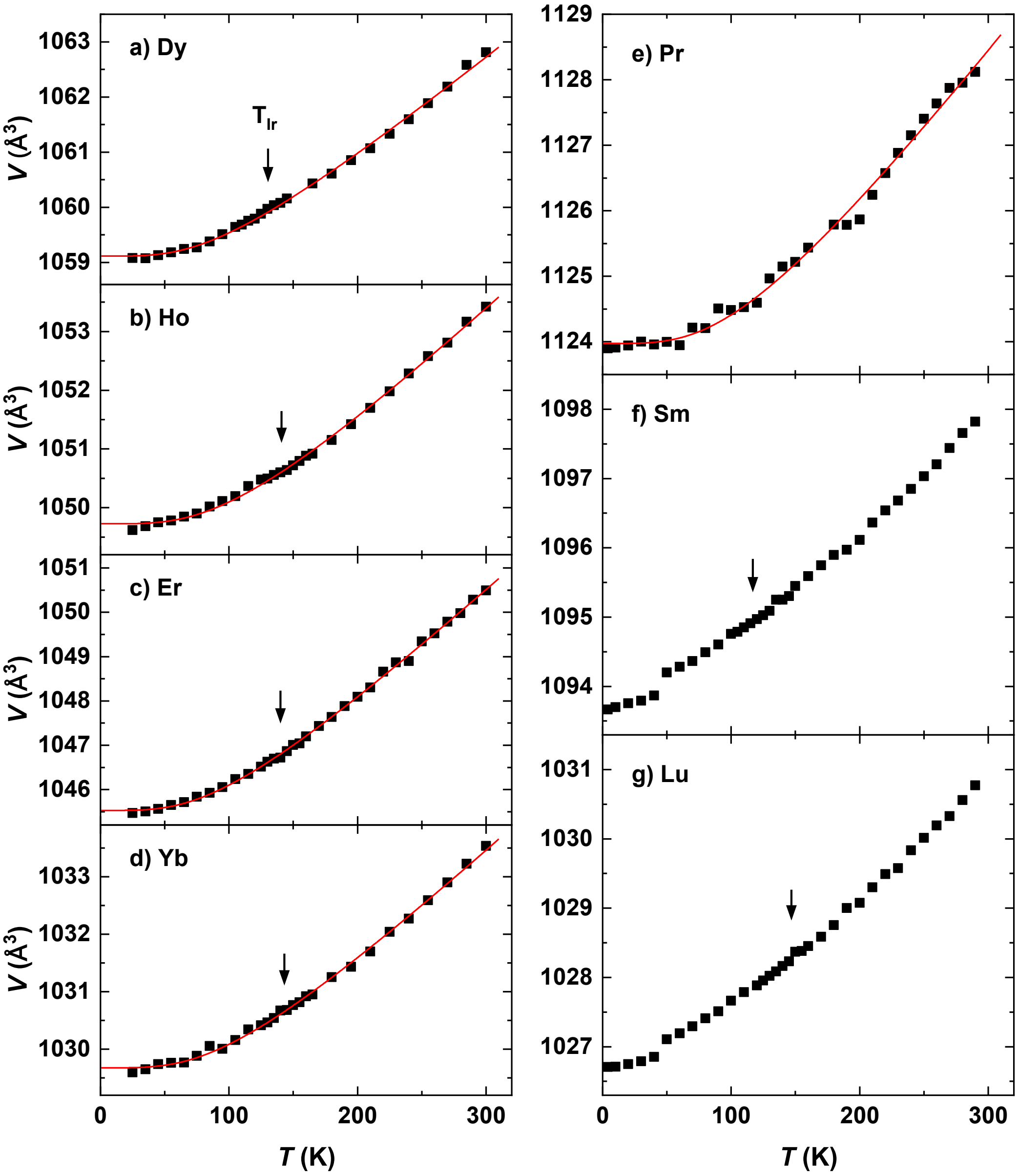

Fig. 4.7: Thermal compressibility of the $A_2Ir_2O_7$ iridates measured at the KMC-2 beamline (A = Dy, Ho, Er, Yb) and the ID22 beamline (A = Pr, Sm, Lu). Arrows indicate the Néel temperature T_{Ir} determined from magnetisation measurements [55]. No anomaly in compressibility is seen at T_{Ir}. The data were fitted to the augmented Debye's model (18), which is indicated by the red curves. Data published in [117].

used to estimate the Grüneisen parameter γ (see the following section). That is, $\gamma = I_V K_0 / 3k_B r$, where $r = 88$ atoms per unit cell for the $A_2Ir_2O_7$ iridates. Similar I_V has been reported also in our neutron diffraction article on $Tm_2Ir_2O_7$ [118]. More specifically, I_0 corresponding to the thermal compression of the lattice parameter a is reported instead of I_V corresponding to volume; a good agreement can be reached after recalculating the data using volume instead of the lattice parameter. The thermal coefficient α_{300K} does not show a clear evolution with the atomic number of the rare earth. Instead, the values remain in the region of approximately 1.7-2.1 10^{-5} K^{-1}, with the exception of A = Er. This observation can be compared to the rare-earth $A_2Ti_2O_7$ titanates (also crystallizing in the pyrochlore structure), which tend to have α_{300K} in the range of 2.4-3.3 10^{-5} K^{-1} [119,120].

Table 4.3: Refined structural parameters and compressibility parameters from thermal diffraction experiments on ID22 and KMC-2 beamlines. Lattice parameter a and the corresponding volume V determined by Rietveld analysis. Zero-temperature volume V_0, Debye temperature θ_D, and I_V, determined from the Debye modelling of the thermal compressibility. Room-temperature thermal expansion coefficient α_{300K}. Values are accompanied by the statistical refinement errors. Data partly published in [117].

A	a (Å)	V (Å^3)	V_0 (Å^3)	θ_D (K)	I_V	α_{300K} ($K^{-1}10^{-5}$)
Pr	10.41002(2)	1128.12(1)	1123.97(5)	420(35)	2.62(14)	2.11(11)
Sm	10.31597(2)	1097.82(1)	-	-	-	1.72(8)
Dy	10.20512(19)	1062.81(6)	1059.12(3)	359(20)	1.93(5)	1.70(3)
Ho	10.17499(13)	1053.42(4)	1049.73(2)	407(16)	2.11(5)	1.83(4)
Er	10.16556(23)	1050.50(7)	1045.53(2)	365(11)	2.70(4)	2.39(5)
Yb	10.11056(19)	1033.54(6)	1029.68(2)	386(16)	2.11(5)	1.88(4)
Lu	10.10154(2)	1030.77(1)	-	-	-	1.90(8)

The temperature evolution of x_{48f} is plotted in Fig. 4.8. x_{48f} describes the distortion of the local oxygen octahedral cages surrounding the Ir^{4+} ions. The Ir-O-Ir bond angle is only dependent on x_{48f}, while the Ir-O bond length is dependent on both x_{48f} and a. In a recent article on $Eu_2Ir_2O_7$, an anomaly was observed at T_{Ir} in the temperature evolution of the bond angle and bond length [69] (see Fig. 4.8c). Therefore, similar anomalies were expected to be followed in other rare-earth members as well (same structure, similar presence of the AIAO AFM ordering and semiconductor-insulator transition). However, no anomalies are clearly visible in the presented data on A = Sm and Lu (A = Pr does not magnetically order down to the lowest temperature; thus no anomaly is expected). In all members, a monotonous increase of x_{48f} upon cooling has been observed. Furthermore, there is a significant systematic evolution of x_{48f} with the radius of the rare-earth ion. The oxygen cages are more distorted (larger x_{48f}) moving from the light end of the series (A = Pr) to the heaviest A = Lu member. Only the data from ID22 are shown, as KMC-2 data have much bigger error bars in comparison. It is difficult to disprove the existence of the anomaly based on the measured data, as the error bars are comparable to the changes seen in the referenced A = Eu member [69] (where the error bars are not reported). Relatively high error of determining x_{48f} despite employing beamlines with very high resolution (especially ID22) can be possibly attributed to the asymmetric nature of the diffraction peaks caused by off-stoichiometry.

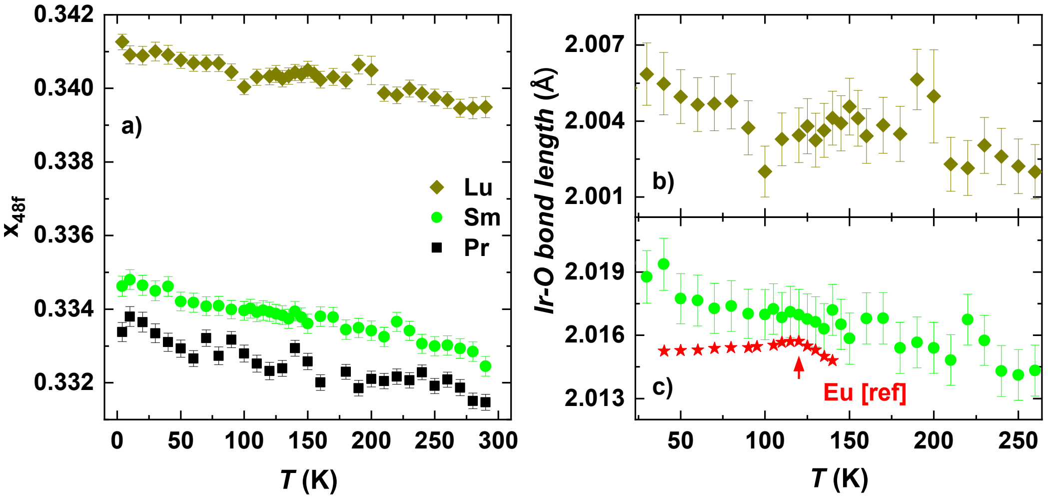

Fig. 4.8: Temperature dependence of the local oxygen environment of the $A_2Ir_2O_7$ pyrochlore structure. a) Evolution of the free oxygen coordinate x_{48f} for A = Pr, Sm, and Lu members. Evolution of the Ir-O bond length of b) A = Lu and c) A = Sm, Eu members. The reference data of $Eu_2Ir_2O_7$ were adopted from [69]. The red arrow marks the anomaly observed in the reference data. Data published in [117].

4.2.2 Compressibility under external pressure

Two high-pressure diffraction experiments have been done; one at the ID15b beamline, ESRF, France, and the other at the I15 beamline, Diamond, UK. The evolution of the structure of A = Pr, Sm, Ho, Tm, and Lu $A_2Ir_2O_7$ iridates with pressure up to 20 GPa was studied using diamond anvil cells (see Section *2.5.2 Diffraction under pressure*). Rietveld analysis was done in a similar fashion as for the temperature-dependent data in the previous section. That is, multiple pyrochlore phases were used to model the ambient pressure data and the ratio of their scale factors was fixed during the pressure-dependent sequential refinement. As the resolution of the high-pressure beamlines is smaller compared to that of ID22 beamline, the instrumental broadening made the previously discussed asymmetry of the diffraction peaks less prominent. Therefore, three pyrochlore phases were enough to reasonably describe the high-pressure diffraction peaks for all measured samples (one major stoichiometric phase and two minor off-stoichiometric phases).

For all investigated compounds, the pyrochlore structure remained stable up to the highest measured pressures. The stability of the pyrochlore structure is illustrated for $Lu_2Ir_2O_7$ in the contour graph in Fig. 4.9. We see the diffraction peaks shift to higher angles (the lattice is compressed) and there are no signs of any diffraction peaks appearing or disappearing with the applied pressure of up to 20 GPa. In most samples, traces of the minority phases (A_2O_3, IrO_2, and Ir) could be followed in the background. Minority phases with large-enough contributions were modelled when refining the diffraction patterns (the Rietveld refinement; Fig. 4.11). In the $Tm_2Ir_2O_7$ member, the signal from the IrO_2 minority phase (around 2.7%) in the background could be followed to observe a structural phase transition at approximately 15 GPa. Multiple peaks were split into two, while some remained unaffected. A transition from tetragonal structure to orthorhombic structure was proposed. For more information on the structural transition of IrO_2, see our publication [117].

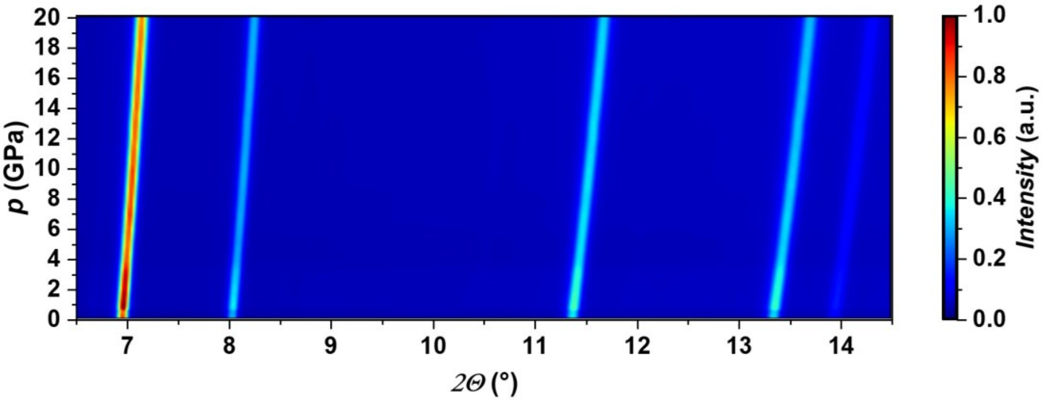

Fig. 4.9: Contour graph of the pressure-dependent diffraction pattern of $Lu_2Ir_2O_7$ measured at I15. Only pyrochlore peaks are observable up to 20 GPa of pressure. Data published in [117].

The powder diffraction patterns of $Lu_2Ir_2O_7$ are presented in Fig. 4.10. Patterns of the remaining samples are summarised in Fig. 4.11. The goodness-of-fit values of the refinements were approximately 1, with the exception of A = Tm member, for which it was around 3. The insets show the evolution of the peak shape with the application of pressure and the depressurisation process. Only minimal broadening of the peak shape is followed up to 20 GPa of pressure, showcasing the (quasi-)hydrostatic conditions. Since He gas was used as the pressure-transmitting medium, hydrostatic conditions are expected in the pressure range up to approximately 12.1 GPa. Under higher pressure, He solidifies at ambient temperature, creating quasi-hydrostatic conditions. The diffraction signal from the solid He was removed during the masking process; therefore, it is not present in the patterns. As seen in the inset of Fig. 4.10, slight broadening can be seen both from moving between 0-10 GPa (hydrostatic conditions) and 10-20 GPa (quasi-hydrostatic conditions). Evidently, solid He is able to create conditions very close to hydrostatic, at least up to 20 GPa.

Data of the pressure evolution of the lattice parameter enables us to follow the compressibility of the selected $A_2Ir_2O_7$ iridates illustrated in Fig. 4.12. Smooth evolution of the volume is observed in all measured analogues. The compressibility data are fitted employing the third-order Birch-Murnaghan EoS (14). The determined structural parameters, including the bulk modulus and its derivative, can be found in Table 4.4. As the application of 20 GPa of pressure results in a total compression of approximately 10% in these materials, compressibility data can also be reasonably modelled by the simpler Murnaghan EoS (12). Indeed, almost identical parameters were obtained from employing the Murnaghan EoS, as well as Vinet EoS. The near-

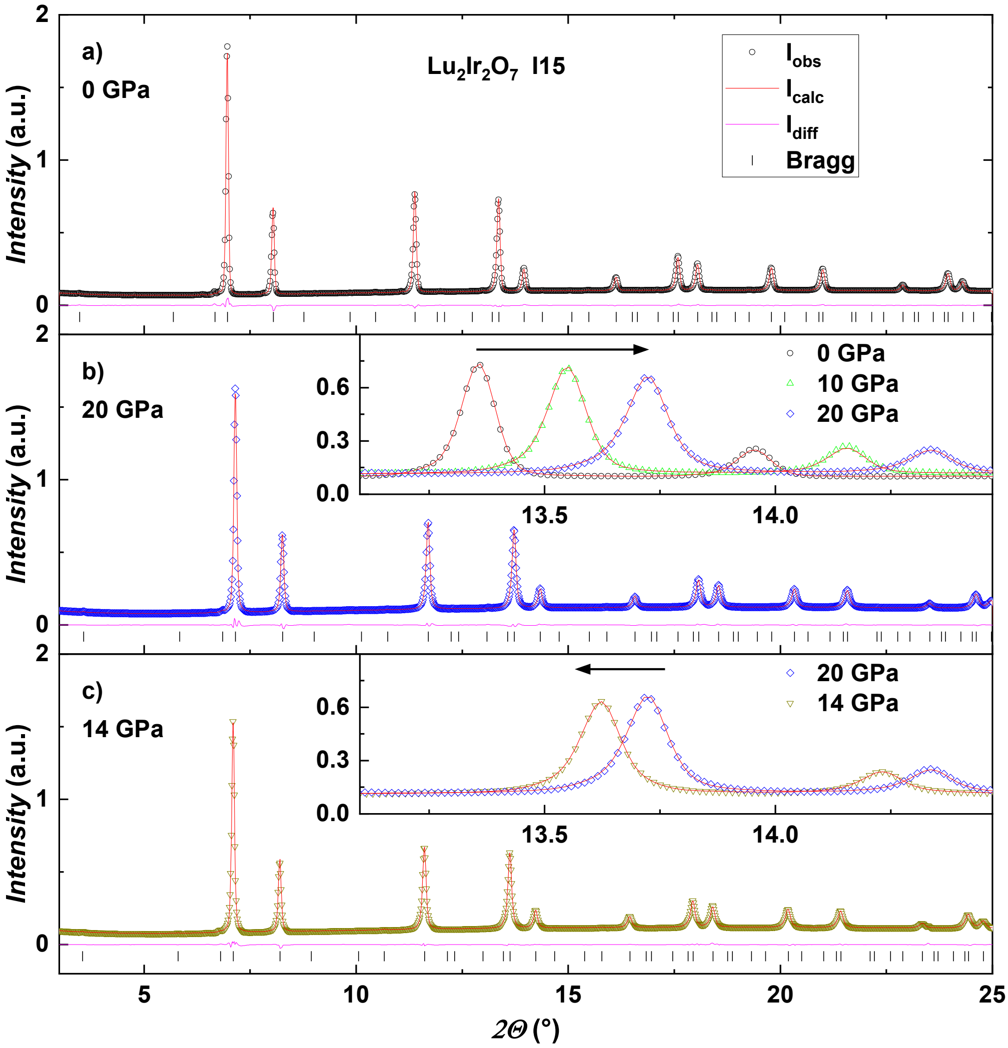

Fig. 4.10: Diffraction patterns of $Lu_2Ir_2O_7$ measured at I15. a) Data from a closed pressure cell at minimal pressure (near-ambient conditions). b) Data from the highest measured pressure 20 GPa and c) from 14 GPa during the depressurisation process. Insets show a zoomed-in region, illustrationg the change of the peak shape throughout the measurements. The ticks describe the main stoichiometric pyrochlore phase. Data published in [117].

ambient-pressure volume (closed pressure cell) is in a very good agreement with the ambient-temperature volume determined from the thermal diffraction experiments. An exception is the slightly higher volume of the *A* = Pr member. As no structural transformations were observed, this means the pyrochlore structure is very robust against high pressure and low temperature. Although we did not measure the entire rare-earth series, we see similarities in several members ranging from *A* = Pr to Lu. Thus, it is reasonable to assume similar compressibilities for the rest of the rare-earth series. As all members exhibit the stable pyrochlore structure, we can compare the effect of hydrostatic pressure to the chemical pressure (substitution) impact on the

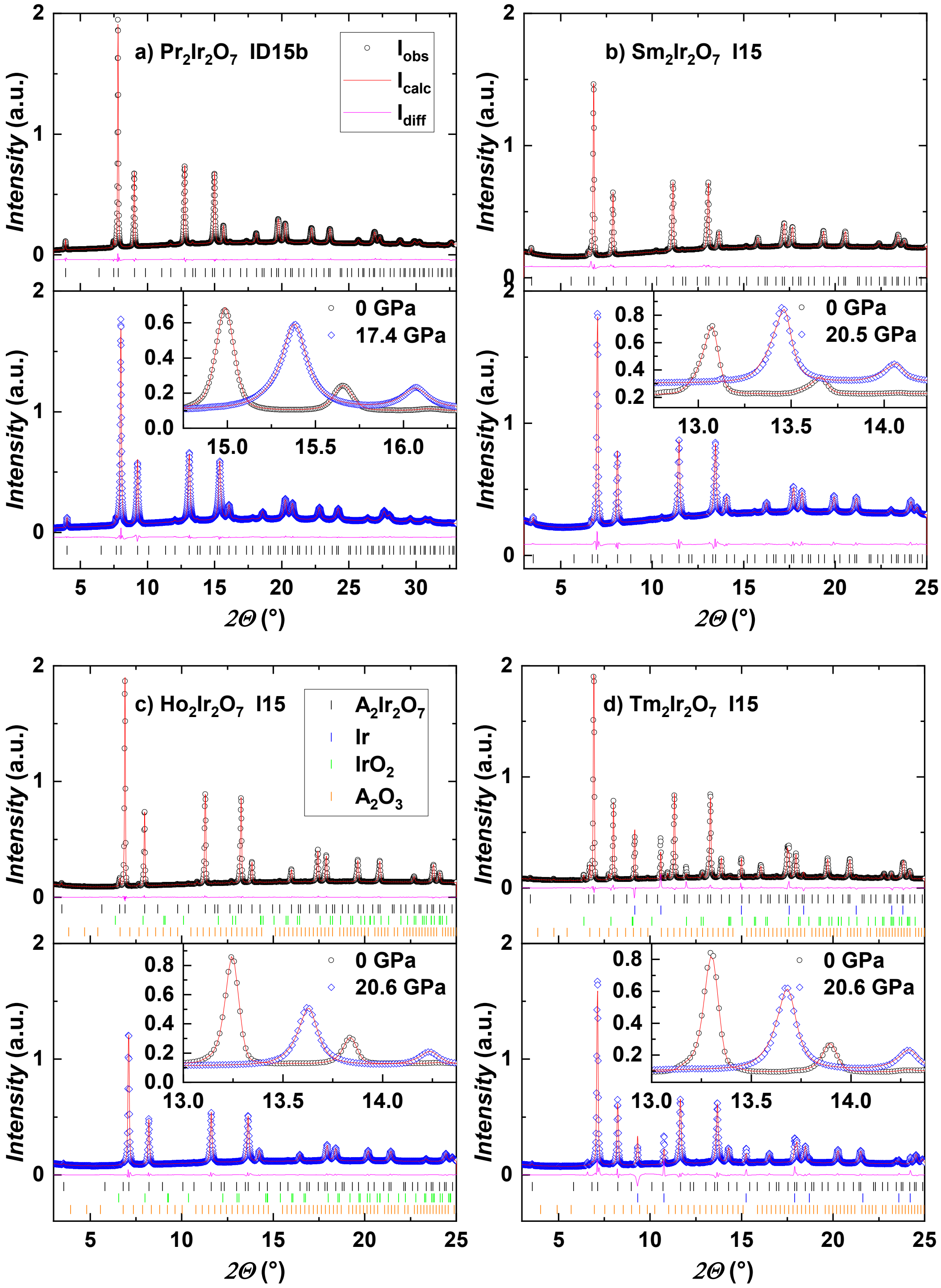

Fig. 4.11: Diffraction patterns of A = Pr, Sm, Ho, and Tm iridates under pressure. The top figures show near-ambient conditions and the bottom figures show the highest-measured-pressure conditions. A = Ho and Tm members were also fitted with the minority phases (see coloured ticks). The evolution of the peak shape is demonstrated in the insets. The ticks describe the main stoichiometric pyrochlore phase. Data published in [117].

crystal lattice. This is illustrated with the horizontal straight lines in Fig. 4.12. The application of 20 GPa of pressure on $Pr_2Ir_2O_7$ results in a pyrochlore structure with approximately the same lattice parameter as $Lu_2Ir_2O_7$. Therefore, a pressure of 20 GPa is enough to shift the structural parameters throughout the whole rare-earth series while maintaining the pyrochlore structure. This, however, does not take into account the change of x_{48f}, which seems to be a crucial factor for the existence of the electrical-transport and magnetic phase transitions.

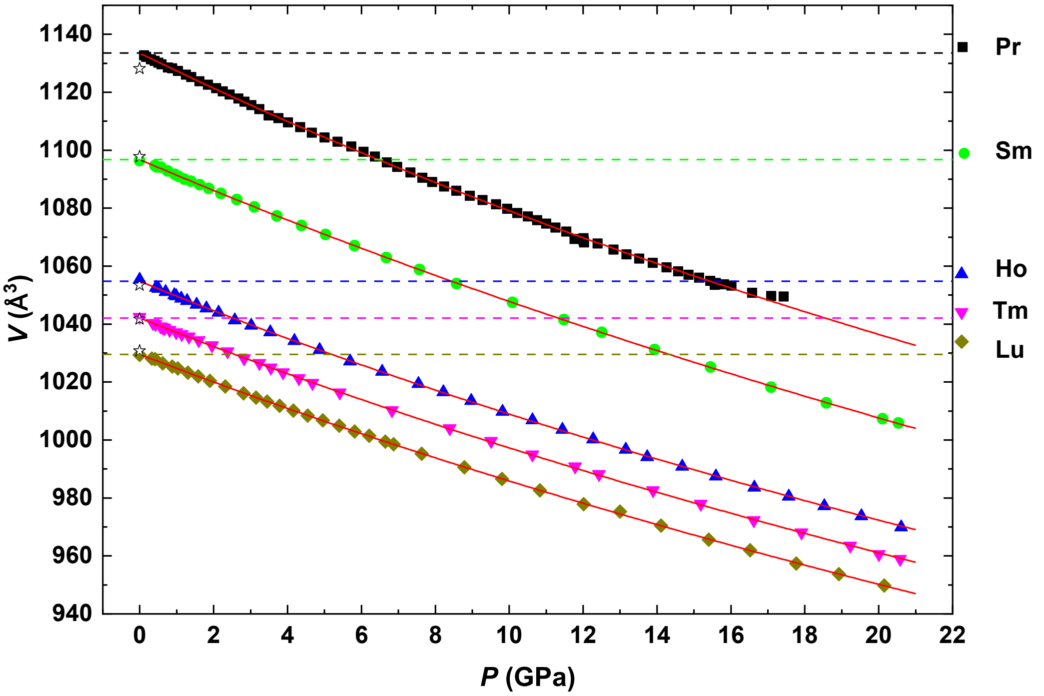

Fig. 4.12: Compressibility of the $A_2Ir_2O_7$ iridates (A = Pr, Sm, Ho, Tm, and Lu) up to 20 GPa of pressure measured at ID15b and I15. The red curves are fits to the third-order Birch-Murnaghan EoS (14). Ambient-pressure volume determined from temperature-dependent diffraction experiments at ID22 and KMC-2 are illustrated by the white stars. Straigth horizontal dashed lines represent ambient-pressure volume of each measured analogue for the purpose of comparing chemical and external pressure. Data published in [117].

In addition to the lattice parameter a, the pressure evolution of the x_{48f} parameter was followed (Fig. 4.13). However, the resolution of the high-pressure beamlines was smaller than that of the thermal diffraction beamlines. This resulted in a larger instrumental error in the x_{48f}. In all cases, a constant trend was followed. That is, no clear pressure evolution of x_{48f} could be seen within the experimental error. The absolute value of x_{48f} is dependent on the radius of the rare-earth ion, as a larger x_{48f} is observed for heavier rare earth, similarly to the observations in the previous section. Only the A = Tm member, which has the highest impurity content and therefore the

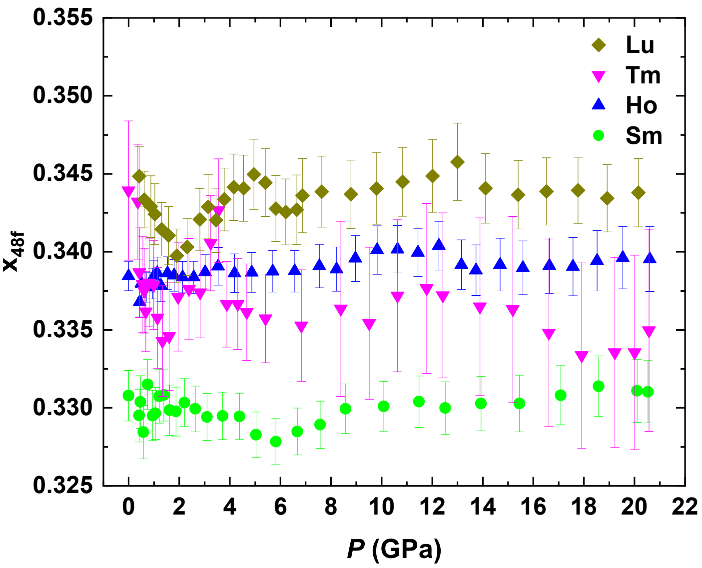

Fig. 4.13: Pressure dependence of the structural parameter x_{48f}. of the $A_2Ir_2O_7$ iridates measured at I15. Data published in [117].

biggest error bars, does not fall clearly into the trend. Compared to chemical pressure, external pressure up to 20 GPa appears to have a negligible effect on x_{48f}. Local anomalies in the data are attributed rather to the refinement and instrumental artefacts.

Refined parameters characterising the pressure compressibility of the $A_2Ir_2O_7$ iridates are displayed in Table 4.4. The bulk modulus monotonously increases with the atomic number of *A*. This result is intuitive, as members with heavier *A* have smaller lattice parameter *a* (lanthanide contraction) and therefore are less compressible with pressure (bigger bulk modulus). Overall, the values of the bulk modulus agree relatively well with the previous results from other groups, e.g., $Eu_2Ir_2O_7$ (K_0 = 209.6 GPa) [121] or $Sm_2Ir_2O_7$ (K_0 = 215.6 GPa) [73]. A similar bulk modulus can also be seen in rare-earth $A_2Zr_2O_7$ zirconates [122], which tend to undergo a structural transition from the pyrochlore phase below 20 GPa. There, however, the pyrochlore structure is not as stable as in the case of iridates, as part of the rare-earth $A_2Zr_2O_7$ zirconate series crystallise in the defect fluorite structure. No systematic evolution of the first derivative of the bulk modulus is observed with the atomic number of *A*. Although the statistical errors are slightly smaller than the differences between K_0' values, the real error (considering also slightly different stoichiometries and impurity phases in different samples) is high enough to mask any evolution. Using the values of I_V determined from thermal compression measurements, the Grüneisen parameter γ was estimated for *A* = Pr and Ho members. For both members, γ is very similar. We cannot comment on the evolution of γ from only two determined values; however, we can compare these values with previous results. In Raman spectroscopy of $Eu_2Ir_2O_7$ [123], determined Grüneisen parameters of individual Raman modes are in good agreement with our results. In general, the Grüneisen parameter of pure metals also shows similar values [124].

Table 4.4: Refined structural parameters and compressibility parameters from high-pressure diffraction experiments on the ID15b and I15 beamlines. Lattice parameter a and the corresponding volume V determined by the Rietveld analysis. Ambient-temperature bulk modulus K_0 and its first derivative K_0' determined from modelling compressibility to the third-order Birch-Murnaghan EoS. The Grüneisen parameter γ is calculated using the equation $\gamma = I_V K_0 / 3k_B r$, where $r = 88$ atoms per unit cell for the $A_2Ir_2O_7$ iridates. Values are accompanied by the statistical refinement errors. Data partly published in [117].

A	a (Å)	V (Å^3)	K_0 (GPa)	K_0'	γ
Pr	10.4242(1)	1132.74(3)	181.2(17)	4.7(3)	1.3(1)
Sm	10.3116(2)	1096.42(6)	200.7(9)	3.81(11)	-
Ho	10.1811(1)	1055.32(3)	202.6(15)	4.7(2)	1.2(1)
Tm	10.1396(3)	1042.47(9)	206.2(11)	4.45(16)	-
Lu	10.0968(1)	1029.32(3)	210.4(11)	4.23(14)	-

4.2.3 Structural evolution with chemical pressure

In addition to the variation of temperature and the application of pressure, chemical pressure (substitution) is the third basic technique of tuning the crystal structure. This often encompasses partial substitution from a few to tens of percent of atoms of one type. However, full substitution (for example, all Pr atoms substituted for Nd atoms) can also be considered, especially since all rare-earth members crystallise in the same pyrochlore structure. As we investigated the structure of multiple $A_2Ir_2O_7$ iridates, comparisons between individual members with different A can be made at ambient temperature and pressure. The evolution of the Ir-Ir bond length is displayed in Fig. 4.14a. As positions of the iridium atoms are fully fixed by the symmetry of the pyrochlore structure, the Ir-Ir bond lengths are (linearly) dependent only on the lattice parameter. As expected from the lanthanide contraction, with increasing radius of A, the lattice parameter a increases as well. An approximately linear trend is seen in the data. On the other hand, the evolution of x_{48f} is not as straightforward. In Fig. 4.14b, we can see a slightly decreasing tendency with A in our data, in agreement with the structural parameters published previously. Only A = Pr member measured at ID15b does not fit into the trend well. It is clear that the ionic radius of A affects the local oxygen-cage distortion, with heavy-rare-earth members exhibiting the largest distortion. However, these variations with A are quite often comparable with the experimental error of the measurement. Moreover, sample dependence also plays a big role in this error (slightly varying stoichiometries of A, Ir, and/or O).

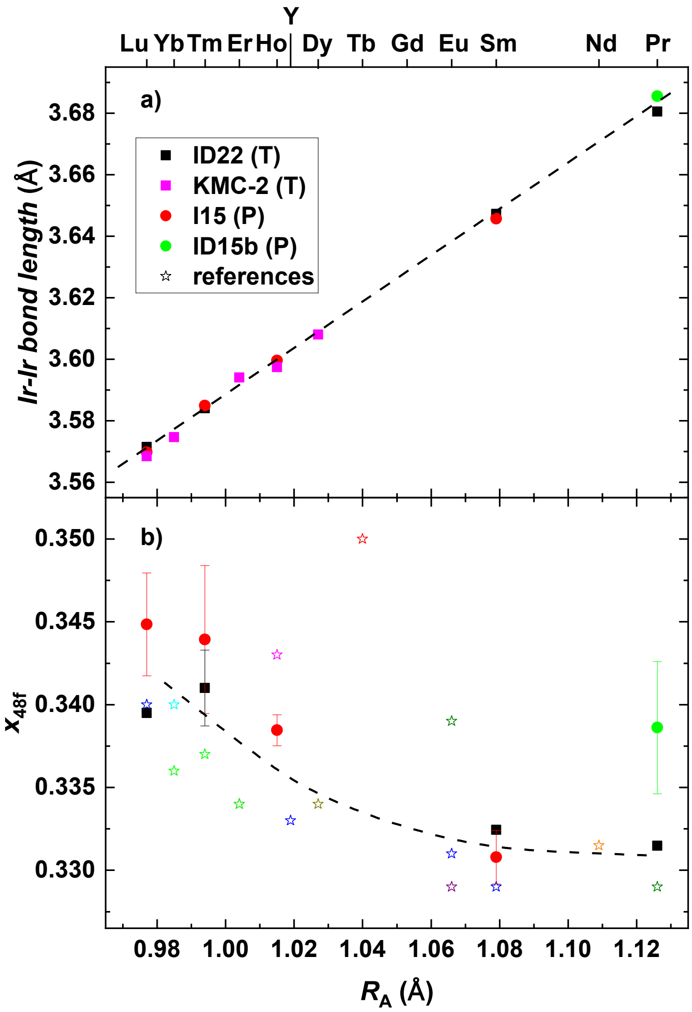

Fig. 4.14: Evolution of a) Ir-Ir bond length and b) x_{48f} with the radius of the rare-earth ion A^{3+}. The corresponding rare-earth trivalent ionic radii (with eight coordination) are shown on the top axis. The dashed line and curve are guides to the eye. Data from all four synchrotron measurements are presented and compared to the previous results (star symbols) from [10,55,71,72,74,97,101,121,125]. Data published in [117].

4.3 Evolution of the electrical transport properties

Electrical transport is directly connected to the electron band structure of materials. Structural and magnetic anomalies are often reflected in electrical resistivity as small features. In this work, electrical resistivity and magnetoresistivity measurements were done on cold-pressed powder pellets of heavy-rare-earth $A_2Ir_2O_7$ members (A = Dy – Lu). Ambient pressure experiments were performed using a measurement puck, and the high-pressure experiments employing a piston pressure cell. PPMS and CCR instruments were used (experimental details in Sections *2.3.1 Electrical resistivity* and *2.4.1 Hybrid piston-cylinder cell*). An example of an experimental montage for ambient pressure measurement is presented in Fig. 4.15.

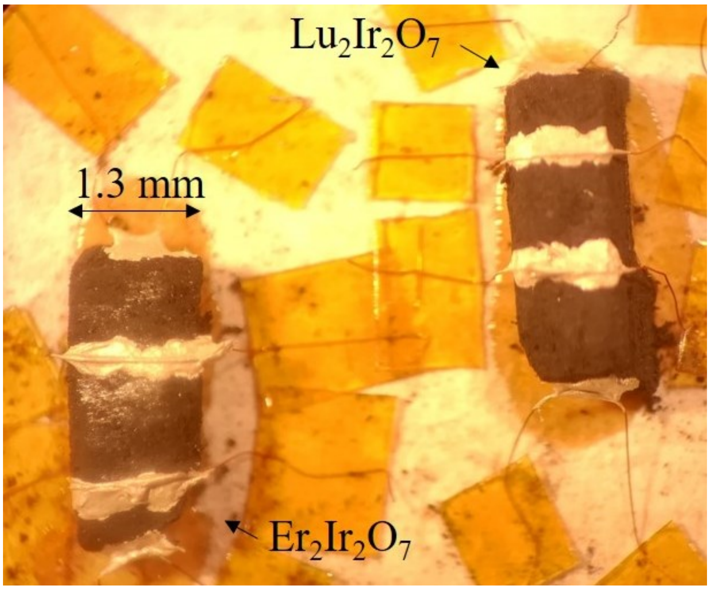

Fig. 4.15: Photo of the powder pellets of $Lu_2Ir_2O_7$ and $Er_2Ir_2O_7$ under a microscope. The samples are glued on a measurement puck and contacted for the electrical resistivity measurement (4-probe method) at ambient pressure. Two samples are measured per one puck.

4.3.1 Electrical resistivity at ambient pressure

The temperature dependence of electrical resistivity was investigated for multiple heavy-rare-earth $A_2Ir_2O_7$ iridates (A = Dy – Lu). As seen in Fig. 4.16a, all measured analogues exhibit semiconducting (at higher temperatures) or insulating (at lower temperatures) behaviour. A relatively broad change of slope in electrical resistivity characterises the transition between these two temperature regions. This can be clearly seen on the log-log scale (inset of Fig. 4.16a). The transition is not visible on the fully linear or semi-logarithmic scale.

A = Lu and Yb members, which are at the end of the rare-earth series (with the heaviest rare earths), show the most insulating behaviour. There, the electrical resistivity increases by cooling from ambient temperature to 5 K by approximately 6 orders of magnitude. Below 5 K, the electrical resistivity of the A = Lu and Yb samples is not shown, as it was too high to measure reliably. That is, even electrical currents of dozens of nA were seemingly strong enough to locally heat the sample and change the value of electrical resistivity (electrical resistivity greater than 10 MΩ). Nevertheless, following the power-law trend from temperature above 5 K, electrical resistivity would probably increase by another 1-2 orders of magnitude before reaching 2 K. The rest of the analogues could be measured down to 2 K, as the insulating properties were not as high as for the A = Yb and Lu members. A = Dy and Ho samples show almost identical behaviour. The $Er_2Ir_2O_7$ sample is the least insulating among the investigated members, with a total increase in electrical resistivity of approximately 3 orders of magnitude. This is peculiar, since Er is in the middle of the investigated heavy-rare-earth series. Therefore, it is difficult to determine a systematic trend based on the rare earth *A*. Overall behaviour in the insulating state resembles a power-law function for the *A* = Yb and Lu members, but this is clearly not the case for the rest of the analogues (at least not in the whole insulating region). In general, the absolute values of electrical resistivity (at least at ambient temperature) are comparable to the previous results on powders [10,32,77,126]. However, this takes into account the possible differences in the sample shape factors and the different pelletisation process (varied grain distribution within the powder pellet).

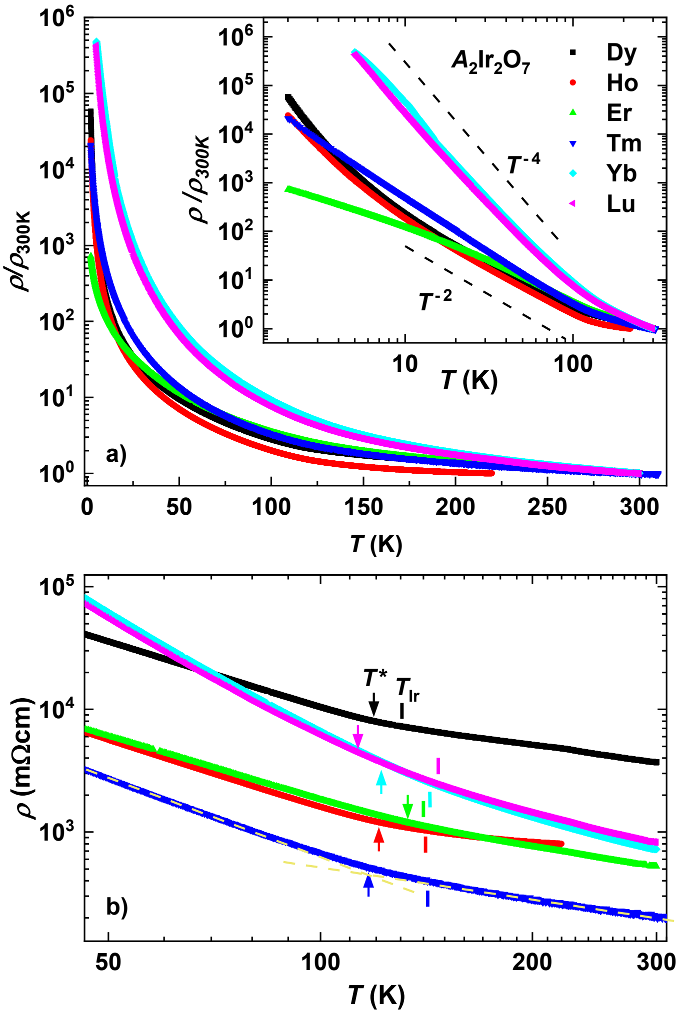

Fig. 4.16: Temperature dependence of electrical resistivity of heavy-rare-earth $A_2Ir_2O_7$ iridates. a) Whole temperature region on a semilogarithmic scale. The inset shows a fully logarithmic scale. The dashed lines in the inset are power-law functions as guides to the eye. b) Zoomed-in temperature region (fully logarithmic scale) presenting the semiconductor-insulator transitions. T^* (arrows), characterising the transition (change of slope), was determined as intersects of linear fits (yellow dashed lines, power-law on log-log scale) below and above the transition. The T_{Ir} values (coloured ticks) were determined from ZFC-FC bifurcation in magnetisation [13,55,97,98]. Data published in [110].

The anomaly in electrical resistivity of $A_2Ir_2O_7$ iridates concomitant with the AFM ordering transition is generally denoted as a metal-insulator transition [32]. This is appropriate for the light-rare-earth iridates, where a local minimum in the electrical resistivity can be observed. For heavy-rare-earth iridates, the focus of this study, a semiconductor-insulator transition is a more appropriate notation. In fact, increasing the atomic number of A promotes more insulating properties. Moreover, more insulating behaviour is accompanied by a broader and less detectable transition. This can be seen in Fig. 4.16 where the A = Yb and Lu analogues are the most insulating and have the broadest anomaly. For heavy-rare-earth iridates, the anomaly is characterised by a change of slope ($\partial\rho/\partial T$) visible only on the fully logarithmic scale. In all measured samples, the biggest change of slope is not at the same temperature as the AFM ordering temperature T_{Ir}. Rather, the broad anomaly is always slightly below T_{Ir}. Approximately at T_{Ir}, the change of slope only starts to develop. For lighter-A analogues, the metal-insulator transition temperature T_{MI} has previously been determined as a local minimum in $\rho(\mathrm{T})$ [32], from a change in its derivative $\partial\rho/\partial T$ [79] or even from a change in $\partial\ln(\rho)/\partial(T^{-1/4})$ [78]. All these techniques become unreliable for broad changes of slope seen in heavy-rare-earth iridates. In order to characterise the anomaly in our data, we employed linear fits on the log-log scale (power-law functions) bellow and above the transition, which intersect approximately at the middle of the transition. The same method was used previously, for example, on $Ho_2Ir_2O_7$ [127]. We denote this temperature as T^* (see Fig. 4.16). As employing intersecting power-law functions does not hold physical meaning, T^* stands to tentatively characterise the position of the transition and is not necessarily equivalent to T_{MI}. The transition is expected to be second-order in nature, as no thermal hysteresis was measured around the anomaly. The broadness of the anomaly may be partially caused by the grain structure of the powder samples.

The temperature dependence of the electrical resistivity was fitted with multiple models in mind, each having a different physical justification. The high-temperature region (above the transition) is described by the Arrhenius thermal activation model (4), which is normally used for semiconductors. The results of the modelling are presented in Fig. 4.17 for all six measured analogues. When plotting the data as $\ln\rho$ vs. $1/T$, the Arrhenius law follows a straight line, therefore it is easier to visually check the validity of the model. The agreement with the model worsens when approaching T_{Ir}, but works reasonably well at higher temperatures. Heavier analogues, such as A = Yb or Lu, exhibit better agreement with the model than lighter members. This observation makes sense as these iridates behave more and more like a semiconductor with increasing A. As the Arrhenius law describes a thermally activated system with an energetic gap, we can estimate the gap energies of the investigated compounds from the refinement (see Table 4.5).

We attempt to describe the insulating (low-temperature) region by three different models. First model employs the power-law fitting, which is described by a simple function $\rho = A_{pl}T^n$, where A_{pl} and n are refined power-law coefficients. To be exact, a power-law evolution with n = -4 is predicted for the single-particle model for

Weyl fermions scattering from a random Coulomb potential, or the so-called thermally screened charged impurities (TSCI) model [128]. This model was previously employed to model electrical resistivity of, e.g., $Y_2Ir_2O_7$ [129] or other light-rare-earth members [82]. Already visible in the inset of Fig. 4.16a, the power law describes the data reasonably well (comparable to the straight dashed lines), but fails at the lowest temperatures. The model was employed at temperatures below the transition around

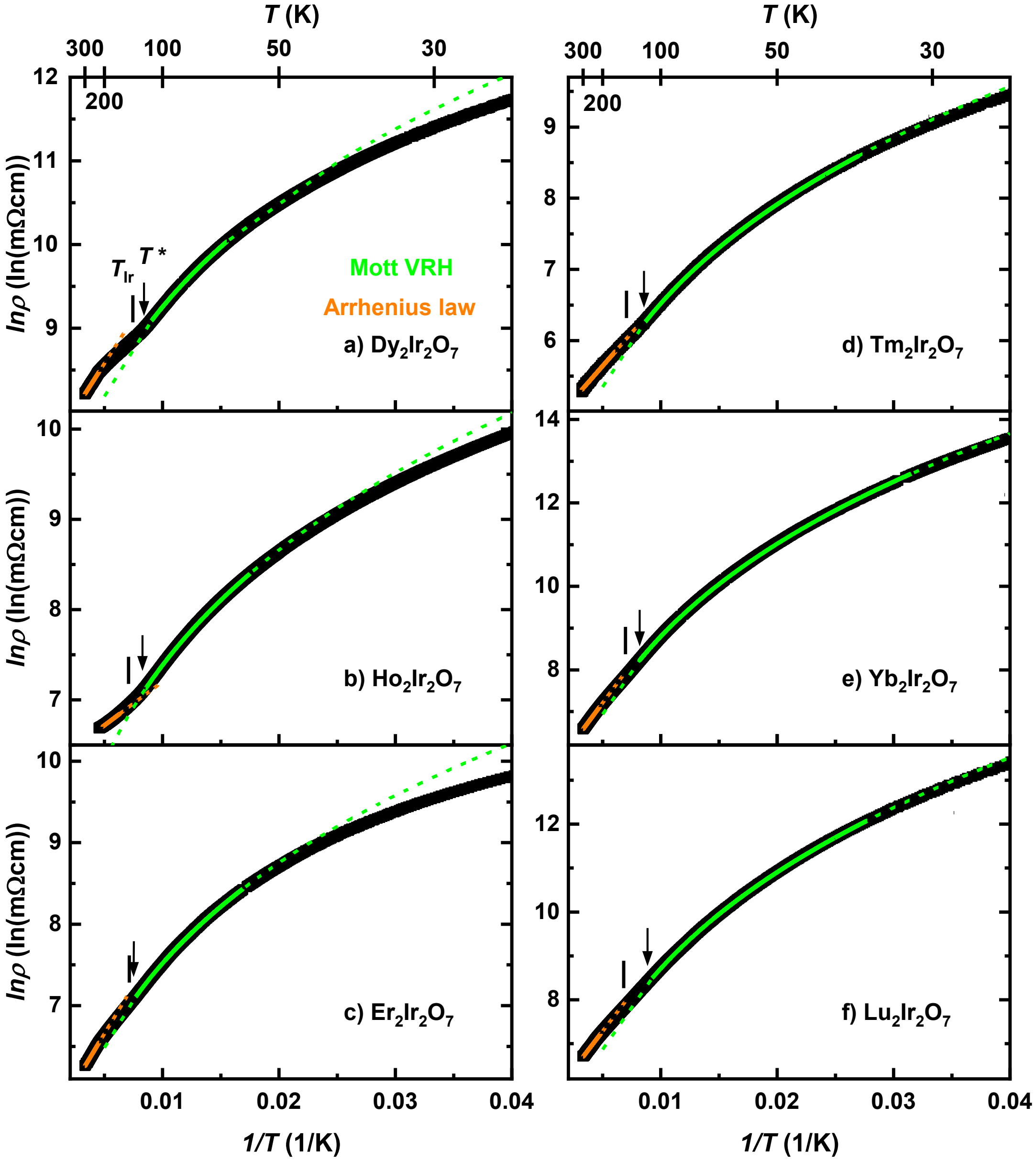

Fig. 4.17: Inverse temperature dependence of lnρ of heavy-rare-earth $A_2Ir_2O_7$ iridates. Straight orange lines correspond to fits to the Arrhenius model at temperatures above the transition, while the Mott variable-range-hopping model was used for temperatures below the transition (green curves). Dashed lines/curves are extrapolated models to the unfitted temperature regions. T_{Ir} and T^* are the same as in Fig. 4.16. Data published in [110].

T^* down to 15 K, as a clear deviation from the model is observed at lower temperatures for all measured members. As seen in Table 4.5, A = Yb and Lu analogues exhibit values of n close to the predicted -4, but the rest of the investigated compounds behave mostly with a coefficient around -2, incompatible with the model. Moreover, the TSCI model clearly cannot be used at the lowest temperatures. Therefore, using the TSCI model alone does not explain the behaviour of electrical resistivity in the measured $A_2Ir_2O_7$ iridates. There is an interplay predicted between the Weyl semimetal and the Mott insulator state [7], which explains the inconsistency with the pure TSCI model.

Secondly, we consider the Mott VRH model. This model is described by the equation (5) and is often used for strongly disordered systems with localised charge carriers. As mentioned in the previous sections, the pyrochlore structure is fully ordered. Thus, in the ideal crystal, no localised charge carriers created by disorder are expected. However, slight off-stoichiometry (which was indeed detected in our samples) can introduce charge carriers. Such a justification for using the Mott VRH model was also previously used in [77,81,82]. The fits to our data are presented as green curves in Fig. 4.17. Although the data corespond well to the model at temperatures right below the transition at T^*, the agreement worsens at lower temperatures. For A = Dy, Ho, and Er samples, the fit does not correspond to the data below 60 K. Heavier analogues show more agreement, but cannot be fitted reasonably below 30 K. At lower temperatures, the model expects a higher electrical resistivity compared to our data. Moreover, the Mott VRH model is often considered to transform into the Efros-Shklovskii VRH model described by equation (6) at low temperatures. This would mean an even higher electrical resistivity predicted at low temperatures, which is the opposite of what is observed. Therefore, the Mott VRH model does not explain the behaviour of the electrical resistivity of $A_2Ir_2O_7$ iridates as well. The incompatibility with the model can be seen as a sign of the off-stoichiometry not having a big impact on the electrical transport properties of our samples.

Finally, the last model considered is the so-called Slater model. It contrasts with the Mott insulator model, not depending on Coulomb interaction but instead on AFM order. The idea used for $A_2Ir_2O_7$ iridates is the same as for $Cd_2Os_2O_7$, which also has a pyrochlore structure and a metal-insulator transition with concomitant AFM order [29,31,107]. As the AIAO order, which is present in both of these compounds, has the propagation vector (0,0,0), both the crystallographic and magnetic unit cells are the same. Hence, the involved Slater mechanism is without Brillouin-zone folding [29]. Electrical resistivity of the Slater-type transition was previously modelled for $Cd_2Os_2O_7$ employing the equation (8) [31]. However, it is difficult to reproduce this in our data simply from the fact that the heavy-rare-earth iridates do not behave as metals above the transition. They already possess a narrow gap at the temperature of the AFM ordering, which is also the temperature at which the Slater mechanism should induce a gap that creates the insulating properties. The coexistence of these gaps potentially plays a role in understanding the true nature of the semiconductor-insulator transition of the $A_2Ir_2O_7$ iridates, but further speculation is better left to the discussion at the end of this thesis.

Following the data in Table 4.5, we can compare the evolution of T_{Ir} and T^* with the rare earth A. The evolution of T_{Ir} determined from magnetisation measurements shows a (more-or-less) monotonous increase with A, not as significant as in the light-rare-earth analogues. In comparison, T^* does not evolve systematically. This is mainly due to the fact that T^* does not describe the broadness of the anomaly, only its position. Moreover, the error of estimating T^* is quite large, especially for broader anomalies, e.g., seen in $Lu_2Ir_2O_7$. Therefore, T^* has a qualitative rather than a quantitative character. The most important observation in this case is that T^* is always found below T_{Ir}.

The refined parameters from the modelling of temperature-dependent electrical resistivity are presented in Table 4.5. Based on the activation energies, the heavy-rare-earth $A_2Ir_2O_7$ iridates are narrow-band semiconductors at high temperatures. No systematic evolution of the activation energy on A can be followed in our results. Previous results documented comparable values of activation energy (mostly light-rare-earth members, but with overlapping A = Dy and Ho analogues) [32,81] with no systematic evolution with A, similarly to our data. The power-law coefficients do not show the expected value $n = -4$ predicted by the TSCI model. Although they are relatively close for A = Yb and Lu members, the statistical error of determining n is quite small compared to the differences between n values for various A. Lastly, the characteristic temperature T_0 of the Mott VRH model follows a similar behaviour as the power-law coefficients n. That is, A = Dy – Tm analogues have similar values which are quite different from the A = Yb and Lu members, and there are no clear signs of systematic evolution.

Table 4.5: The anomalous temperatures and refined parameters of the electrical transport properties of $A_2Ir_2O_7$ iridates. The temperature of the AFM ordering T_{Ir} was determined from the bifurcation in magnetisation (previous results of our group). T^* characterises the semiconductor-insulator anomaly in electrical resistivity data. Refined parameters, namely the activation energy Δ (Arrhenius law), power-law coefficient n (TSCI model), and characteristic temperature T_0 (Mott VRH model), are presented. Data published in [110].

A	T_{Ir} (K)	T^* (K)	Δ (K)	n	T_0 (10^5 K)
Dy	131(2) [97]	119(5)	218(1)	-1.86(1)	2.0(1)
Ho	141(2)	121(8)	97(1)	-1.97(1)	2.1(1)
Er	140(2) [13]	133(6)	237(1)	-1.49(1)	1.8(1)
Tm	142(2) [55]	117(7)	187(1)	-2.25(1)	2.9(1)
Yb	143(2) [55]	122(7)	375(1)	-3.74(1)	18.9(1)
Lu	147(2) [98]	113(10)	346(1)	-3.75(1)	18.0(1)

4.3.2 Magnetoresistivity at ambient pressure

Aside from the temperature-dependent measurements of electrical resistivity, the magnetic-field dependences were also measured (i.e. magnetoresistivity (MR) measurements). Relative MR of all six investigated heavy-rare-earth iridates is presented in Fig. 4.18a. All members, with the exception of A = Lu member (Lu^{3+} is nonmagnetic), exhibit a significant drop in electrical resistivity with the application of magnetic field at low temperatures (2 K). The drop is most significant in smaller magnetic fields up to 2 T, after which the decrease in MR is not as pronounced. The $Lu_2Ir_2O_7$ member is only affected by the magnetism of Ir^{4+} ions. Compared to the significant drop in other measured samples, the MR of $Lu_2Ir_2O_7$ seems approximately constant. Nevertheless, the contribution of Ir magnetism results in very small changes in MR up to 9 T. These changes are not negligible and are addressed separately in the following section. Here, we focus on the big drop in MR caused by the magnetism of rare-earth A^{3+} ions. Relative MR drops down to ~8% of the zero-field value for $Dy_2Ir_2O_7$ at 9 T. The large drop in MR quickly disappears at higher temperatures, as illustrated in Fig. 4.18b with $Er_2Ir_2O_7$ data. Here, we see that heating up to ~10 K already greatly suppresses the drop in MR. At around 15 K, the values of electrical resistivity are almost the same. At higher temperatures, both the 0 T and 9 T curves exhibited almost identical behaviour, even around T^* or T_{Ir}. Similar behaviour is seen in all investigated compounds.

The magnitude of the drop is systematic with regard to the rare earth A. Although monotonous, the evolution of the drop with A is far from an equidistant evolution of the compressed pyrochlore structure. Therefore, lanthanide compression does not play a decisive role here. Instead, we look at the different magnetic moments of A^{3+} ions. As seen in Table 1.1, Dy^{3+} and Ho^{3+} free ions have the highest predicted magnetic moment, which monotonously decreases when moving to heavier rare earths, all the way to the nonmagnetic Lu^{3+}. In all investigated samples, the rare-earth ions do not magnetically order down to 2 K, and all have an AFM-ordered Ir sublattice at 2 K (below T_{Ir}). Based on the behaviour seen in Fig. 4.18b, it is highly possible that the observed drop is mostly affected by the magnetism of rare-earth ions, which commonly show magnetic features only at very low temperatures. The ordered Ir sublattice is known to create a local molecular field which can have a magnitude of multiple Tesla. At lower temperatures, where the correlations between A^{3+} ions are stronger, the influence of the Ir molecular field on A^{3+} can result in the observed drop in MR. Thus, magnitude of the magnetic moment of A^{3+} may be directly related to the drop in MR. Looking at the difference in the magnitudes of the drops, the most puzzling is the comparison between the A = Tm and Yb analogues. Although the drops are similar, the free Tm^{3+} ion has an almost two-times larger magnetic moment than the free Yb^{3+} ion. This is probably connected to the difference between a free ion and an ion in a crystal electric field of the pyrochlore structure. More insights into the band-splitting can be investigated by inelastic neutron diffraction. For example, $Tm_2Ir_2O_7$ showed a nonmagnetic singlet ground state in [55]. In $Yb_2Ir_2O_7$, on the other hand,

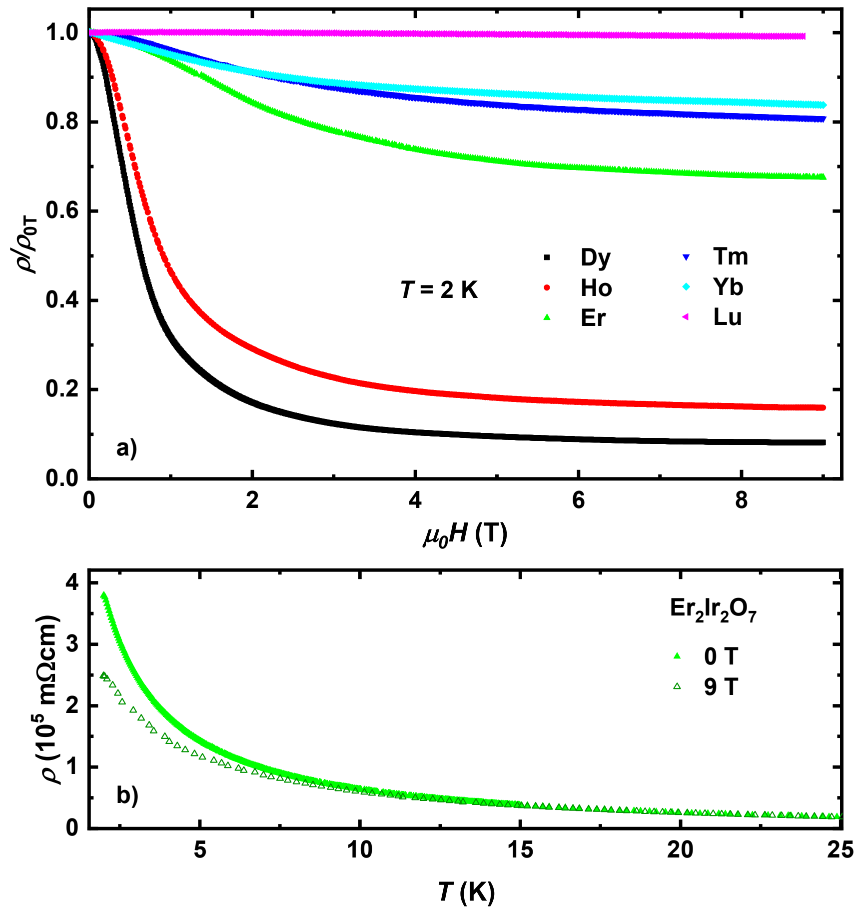

Fig. 4.18: a) Relative magnetoresistivity of heavy-rare-earth $A_2Ir_2O_7$ iridates (A = Dy – Lu), measured at a constant temperature of 2 K. All data are smoothed for better readability. b) Comparison between the electrical resistivity of $Er_2Ir_2O_7$ without/with magnetic field (0 T or 9 T), showing the low-temperature effect of Er magnetism on the magneoresistance. Data published in [110].

the energy level degeneracy is protected by Kramers' theorem, allowing a minimal double degeneracy (all levels at least doublets). In a similar fashion, A = Dy and Ho have slightly different drops while having the same free-ion magnetic moment. In a crystal field, Ho^{3+} energy levels can be singlets, but only doublets are allowed for Dy^{3+} energy levels (see example in the Section *1.1 Magnetic properties of rare-earth A3+ ions*).

No clear hysteresis has been observed in any of our MR measurements in Fig. 4.18a. This is very different from the observations on a $Ho_2Ir_2O_7$ single crystal, where MR hysteresis was seen with magnetic field along <111> but not along <100> crystallographic axes [2]. As our samples are pelletised powders, any anisotropic measurements cannot be replicated, as the anisotropic features are expected to combine into one isotropic information. Therefore, it is possible that in our powder $Ho_2Ir_2O_7$ sample, most grains contributed to no hysteresis and hid the hysteresis that was seen in the single crystal.

4.3.3 Application of high pressure

External pressure was employed to tune the pyrochlore structure (interatomic distances and bond angles), affecting the electrical transport as well as the magnetic properties. Two analogues were chosen for the high-pressure electrical transport experiments. First, the $Lu_2Ir_2O_7$ end-member containing the nonmagnetic Lu^{3+} cation. Magnetic properties of this iridate stem only from Ir magnetism, similarly to the heavily investigated light rare-earth $Eu_2Ir_2O_7$. In comparison, the second investigated member $Er_2Ir_2O_7$ exhibits, in addition to Ir moment, a strong magnetism of Er^{3+} cations (it has also been previously studied in our group; see [13,109]). Electrical resistivity and magnetorestivity measurements of pelletised powder samples were carried out employing the PPMS and CCR instruments with 3 GPa hybrid piston-cylinder pressure cell (see Section *2.4.1 Hybrid piston-cylinder cell*).

As was previously shown, both A = Er and Lu analogues exhibit a semiconductor-insulator transition at intermediately low temperatures, similarly to other heavy rare-earth iridates (Fig. 4.16). The application of external pressure results in both an increase of T^* and a decrease in electrical resistivity for both analogues (see the insets in Fig. 4.19ab). The overall shape of the thermal dependence of resistivity does not change significantly up to 3 GPa of pressure. The decrease in resistivity with pressure is more pronounced at the lowest temperatures; $Lu_2Ir_2O_7$ shows a resistivity decrease of approximately two orders of magnitude at the lowest temperatures (estimated with power-law behaviour for $P \leq 1$ GPa). In previous studies, 6 GPa of pressure was reported to close the insulating gap and induce a metallic state in $Eu_2Ir_2O_7$ [83]. Therefore, more conductive properties with the application of pressure are expected in heavier-rare-earth iridates. Nevertheless, not surprisingly, 3 GPa of pressure is not enough to close the insulator gap for the more insulating (compared to A = Eu) members $Er_2Ir_2O_7$ and $Lu_2Ir_2O_7$. The decrease of electrical resistivity with pressure can be additionally attributed to the powder nature of the samples; the grains become more compacted under high pressure, reducing the electrical resistivity at the grain boundaries.

Inspecting the semiconductor-insulator transition in Fig. 4.19ab closer, it monotonously shifts to higher temperatures with the application of pressure. The broad transition, especially in $Lu_2Ir_2O_7$ data, and its evolution with pressure was effectively tracked using the T^* parameter introduced in Section *4.3.1 Electrical resistivity at ambient pressure*. T^* increases by approximately 20-25 K with the application of 3 GPa of pressure for both studied iridates. T^* for $Lu_2Ir_2O_7$ shows lower values than for $Er_2Ir_2O_7$, which is attributed to the difference in the broadness of the anomalies (T_{Ir} is slightly increasing with A, which should be reflected in the behaviour of T_{MI}). Comparison with the previous report on the pressure evolution of T_{MI} [78] is presented in Fig. 4.19c. Despite the formal inequivalence between T^* and T_{MI}, both can be employed to track the temperature shift of the transition with pressure. Unlike significant differences between the evolutions in A = Sm, Eu, Gd members (decreasing

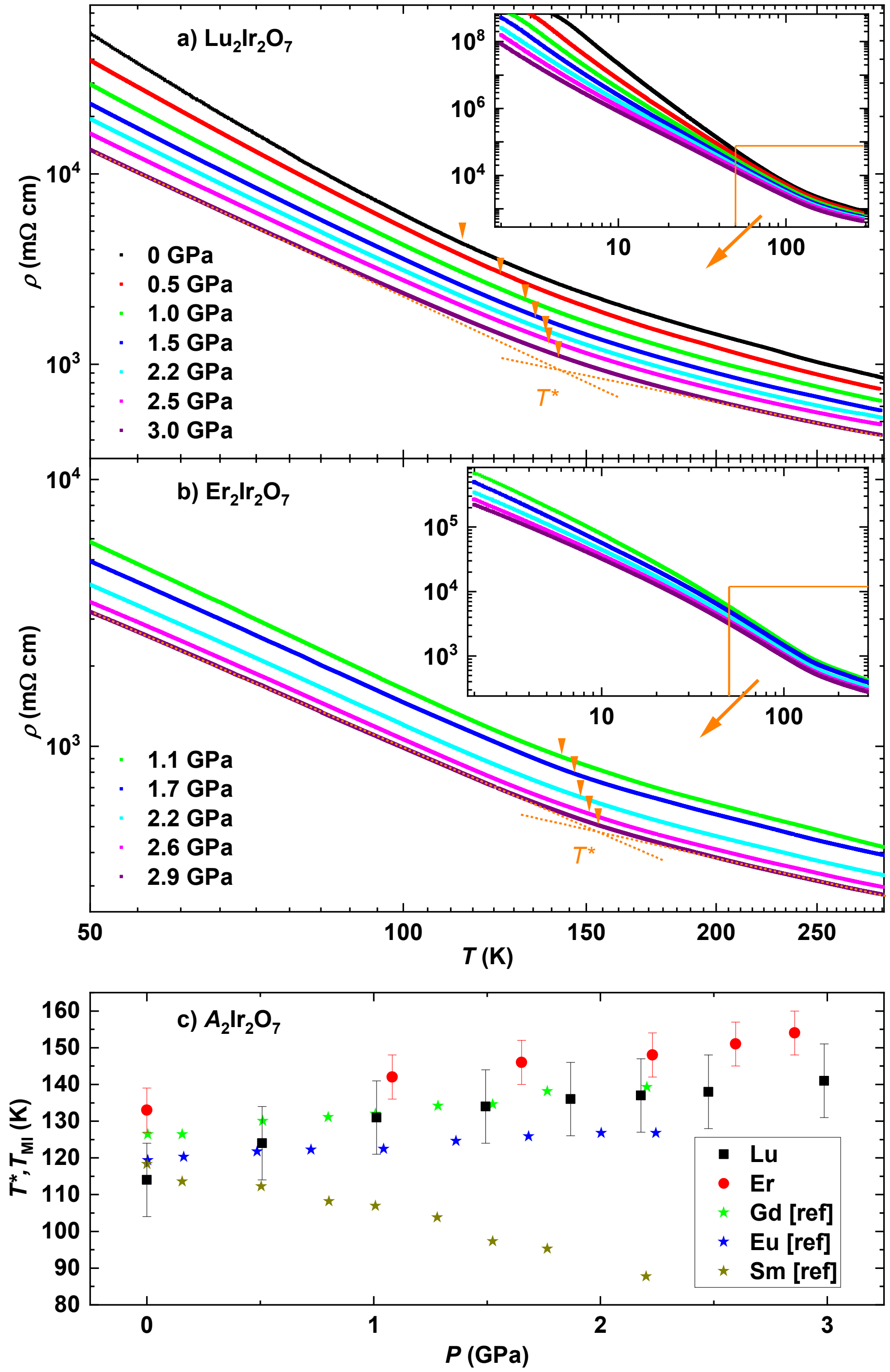

Fig. 4.19: Temperature dependence of electrical resistivity (fully logarithmic scale) of a) $Lu_2Ir_2O_7$ and b) $Er_2Ir_2O_7$ under various pressures up to 3 GPa. The insets show the whole measured temperature region, while the main panels focus on the anomaly at higher temperatures (orange blocks in the insets). The data are smoothed to eliminate the contribution from the solidification of Daphne 7575 upon cooling and the instrumental temperature hysteresis. The arrows depict the temperature T^*, describing the anomaly as an intersection of power-law functions (orange dashed lines). c) Pressure dependence of T^* (our data) compared to T_{MI} from previous results on A = Sm – Gd powder samples [78]. Data published in [130].

for Sm, stagnating for Eu, and increasing for Gd) [78], our A = Er and Lu samples exhibit similar evolution to the A = Gd member. Given the positions of Gd, Er, and Lu in the rare-earth series and keeping in mind the phase diagram (Fig. 3.2), it is possible that a similarly increasing pressure evolution of T_{MI} (T^*) is present for all heavy-rare-earth $A_2Ir_2O_7$ iridates.

As a technical side note, we mention the process of smoothing the data in Fig. 4.19ab. One of the reasons to smooth the data is the instrumental temperature hysteresis observed in the raw PPMS data. The connector mounted on the pressure cell to fit it in the PPMS resulted in smaller thermal conductivity, which created a thermal hysteresis when cooling/heating the cell and sample with a 1 K/min speed. No thermal hysteresis was observed in the CCR data, as the CCR is more accustomed to pressure cells of this type. The second reason is the solidification of the pressure-transmitting medium Daphne 7575 upon cooling (see the phase diagram in [56]). Small anomalies have been observed in the $Er_2Ir_2O_7$ data corresponding exactly to the solidification temperatures of Daphne 7575. This is also the reason why 0.5 GPa data of $Er_2Ir_2O_7$ are not presented, as the solidification occurs at temperatures similar to those of the semiconductor-insulator transition. Interestingly, no solidification anomaly was observed in the $Lu_2Ir_2O_7$ data. This is probably caused by the fact that the A = Er sample was freshly pelletised before the high-pressure experiment; that is, it had no thermal history (untrained sample). In contrast, the A = Lu sample was measured at ambient pressure before it was used for the high-pressure experiment. That is, A = Lu sample was cycled down to 2 K before being exposed to the Daphne oil and high pressures (using the same silver-paste contacts). Therefore, to minimise the anomalous instrumental contribution on electrical resistivity of powder pellets at high pressures, we advise the scientific community to thermally cycle the sample to strengthen the grain integrity and the contacts prior to the application of high pressure.

In addition to thermal measurements, magnetoresistivity was followed at various pressures. The pressure evolution of the relative MR of $Er_2Ir_2O_7$ is presented in Fig. 4.20. Although the overall shape of the MR curve does not change significantly with pressure, small shifts in the absolute value of the MR drop are followed (inset of Fig. 4.20). The evolution is not monotonous, which is unexpected, as all other properties evolve systematically with pressure. It is unclear whether the observed changes are caused by intrinsic properties of the studied material or by instrumental techniques and the powder nature of the sample.

On the other hand, MR of $Lu_2Ir_2O_7$ does not exhibit a significant drop related to the rare-earth magnetism. Here, we follow up on the ambient-pressure MR results and focus solely on the small contribution from Ir magnetism, which is prominent in the $Lu_2Ir_2O_7$ member. MR at the highest measured pressure 3 GPa is presented in Fig. 4.21. These data have the lowest absolute resistivity values and the lowest experimental noise, which makes them the best choice for showcasing the overall MR properties of $Lu_2Ir_2O_7$. In the ZFC regimen at 2 K, the changes in MR are within

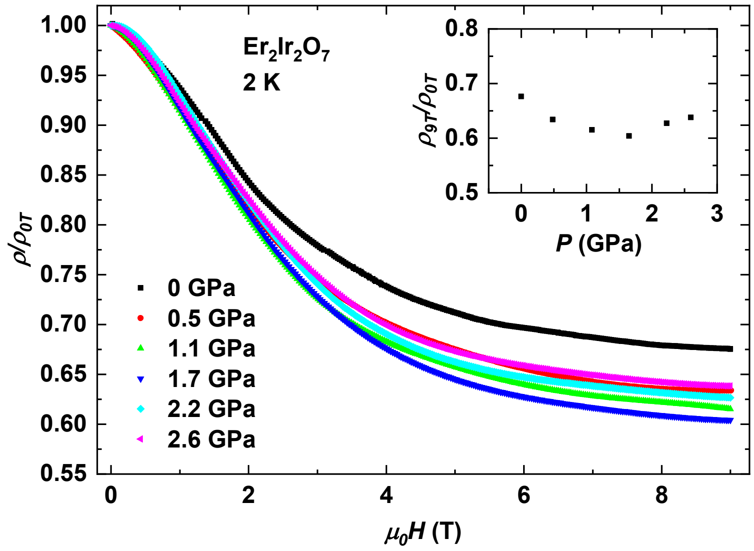

Fig. 4.20: Relative magnetoresistivity of $Er_2Ir_2O_7$ at various pressures up to 3 GPa, measured at 2 K after a ZFC regimen. All data are smoothed for better readability. The inset shows the pressure evolution of the largest drop in MR characterised as the ratio between the 9 T and 0 T values. Data published in [130].

approximately 2% when measured up to a field of 9 T (Fig. 4.21a). These changes are even smaller at higher temperatures and lower pressures. Therefore, they are hardly observable in other analogues with a significant MR drop. Nevertheless, interesting information about the Ir magnetism of $A_2Ir_2O_7$ iridates can be obtained when different FC regimens are employed.

Two important phenomena are followed. The first is the asymmetric shape of the MR measured in the FC regimens (symmetric in the ZFC case). The asymmetric MR is controllable by the cooling field and is characterised by a linear asymmetric contribution. That is, a curve similar to the symmetric ZFC data is obtained by subtracting a linear term from the asymmetric FC data (dashed lines in Fig. 4.21). The second phenomenon is the hysteresis seen at higher temperatures. These two phenomena coexist in the 50 K data (Fig. 4.21b). Similar phenomena were followed in $Eu_2Ir_2O_7$ single crystals [92] and thin films [91] (nonmagnetic Eu^{3+}), although the overall shape of the MR curve is very different in our $Lu_2Ir_2O_7$ data. Importantly, the electrical resistivity in zero field seems to be independent of the cooling field. Therefore, ZFC and FC temperature scans of electrical resistivity do not exhibit the MR phenomena; they behave the same regardless of the cooling field (Fig. 4.19).

Hysteresis in MR is usually explained by the ferromagnetism of the material. An asymmetric MR should not be present without Hall resistivity contribution. The magnetic field was applied parallel to the electrical current, hence, the Hall contribution is negligible in our data. In fact, MR behaviour should always evolve into a symmetric hysteresis in a high enough magnetic field. Only Ir^{4+} is magnetic in $Lu_2Ir_2O_7$, and it orders AFM below ~147 K, thus, no FM contribution is typically expected. However, previous magnetisation results reported a small FM contribution in the AFM phase of several rare-earth iridates [92,100,101]. The probable nature of the FM contribution is explained by robust FM domain walls, discussed in more detail in the following Section *4.4 Antiferromagnetic domain structure*. We explain both MR phenomena by a small FM contribution of these domain interfaces. The hysteresis at higher temperatures is explained by "rotatable" spins at the end of respective AFM domains weakly coupled to the DWs. Their contribution is suppressed at lower temperatures where they gradually freeze, leaving no hysteresis. The asymmetric term is explained as an onset of a hysteresis which is not reachable up to 9 T field. This potential hysteresis (in high enough fields) is created by the "frozen" spins, embedded in the DWs, and protected against magnetic field by a robust AFM domain structure. A similar concept of a robust FM contribution pinned by the AFM phase was previously used also in the case of AFM/FM heterostructures [103,104].

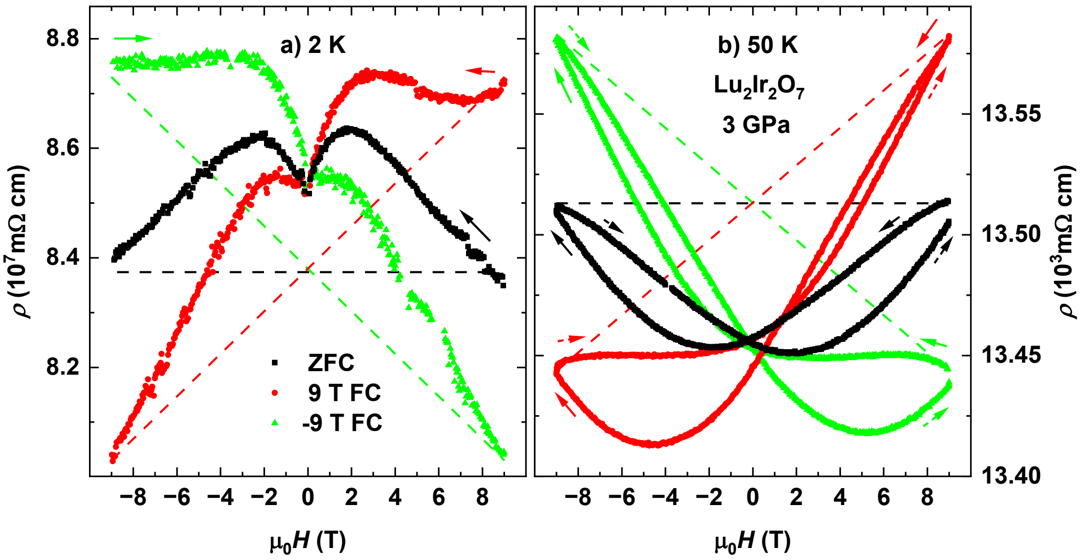

Fig. 4.21: Magnetoresistivity of $Lu_2Ir_2O_7$ at 3 GPa at a constant temperature of a) 2 K and b) 50K. Results from three different cooling regimens are presented (cooling down without field (black), with a 9 T field (red), or with an opposite -9 T field (green)). Arrows represent the field (time) evolution of the experiments (dashed arrows depict the second half of the experiment). The red and green dashed lines represent the asymmetric linear contributions to MR. ZFC data have horizontal dashed lines, i.e., no asymmetric contribution. Data published in [130].

Next, we inspect the pressure evolution of MR. As the absolute values of MR change significantly with pressure (~2 orders of magnitude at 2 K), only the relative MR curves from different pressures can be reasonably compared. Pressure evolution of the 9 T FC relative magnetoresistivity is presented in Fig. 4.22, showcasing the linear asymmetric component of MR at different pressures. The application of pressure evidently increases the asymmetric contribution to MR. For quantitative analysis, we describe the linear asymmetric term using a coefficient α_{MR}. This method was previously used on $Eu_2Ir_2O_7$ thin films [91,93], employing an equation $\rho(\mu_0 H)/\rho(0)$ = (symmetric part) + $\alpha_{MR}\,\mu_0\,H$. This technique effectively divides the MR data into a symmetric and linear asymmetric term. Results of the α_{MR} determination are presented in Fig. 4.22bc for data from 2 K and 50 K. As the low-pressure data from 2 K were measured at the limits of the experimental apparatus, the error bars are significantly larger. Furthermore, in this case, the samples were locally heated by the electrical current; therefore, the values of α_{MR} can be slightly underestimated. Both the 2 K and 50 K data show a monotonous increase of α_{MR} with pressure, while both the slope and the absolute values are significantly higher for the data at 2 K. Our results are compared to the ambient pressure α_{MR} of $Eu_2Ir_2O_7$ thin films [91], which show values reasonably similar to our data after extrapolation to ambient pressure. The linear asymmetric term quantified by α_{MR} can be understood as being directly connected to the magnitude of the FM contribution which caused it. Thus, it makes sense that similarly to α_{MR}, the FM component is smaller at higher temperatures. Additionally, the FM contribution is accordingly expected to increase at elevated pressures.

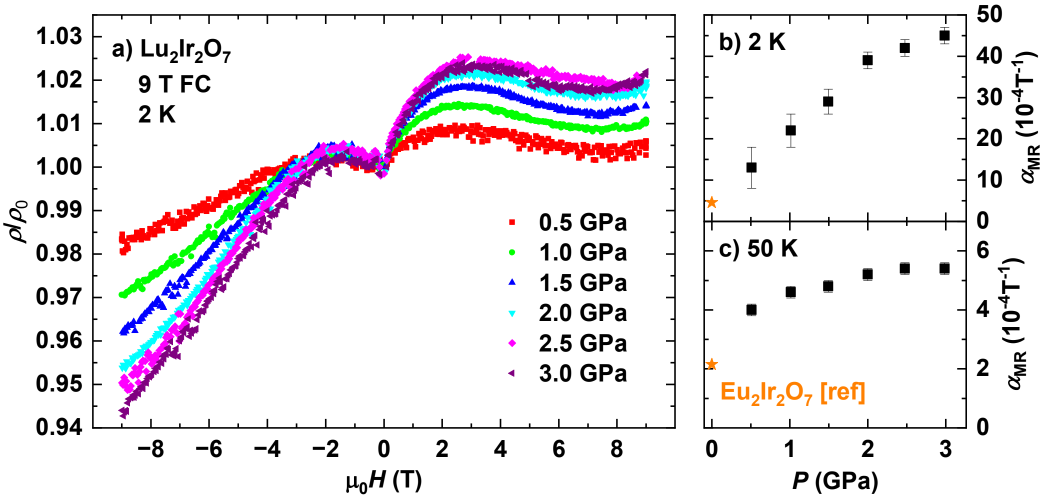

Fig. 4.22: a) Relative magnetoresistivity of $Lu_2Ir_2O_7$ at several pressures up to 3 GPa. Data were measured at 2 K after a 9 T FC regimen. Pressure evolution of the linear asymmetric term in a) is characterised by α_{MR}, measured b) at 2 K and c) at 50K. Ambient-pressure reference data of α_{MR} measured on $Eu_2Ir_2O_7$ thin films [91] are included for comparison. Data published in [130].

Finally, we briefly mention an AC magnetic susceptibility study done concomitantly with the high-pressure electrical transport measurement of $Er_2Ir_2O_7$. That is, in one high-pressure experiment (one pressure cell), both electrical resistivity and AC magnetic susceptibility of $Er_2Ir_2O_7$ were measured (see Section *2.3.4 AC magnetic susceptibility*). We attempted to follow a magnetic response from the Ir sublattice, or alternatively, from Er sublattice (short range correlations, as Er sublattice does not order at the measured temperatures down to 2 K). No particularly relevant developments (considering the MR data discussed above) have been observed in the data (Fig. 4.23). The temperature dependence of both real and imaginary part of the AC magnetic susceptibility did not change significantly when varying frequency of the AC field between 10-9900 Hz at any constant pressure. In the same manner, no significant changes were observed when applying pressures up to ~3 GPa. Specifically, although small changes in absolute values were present, plotting all data together as relative changes of AC susceptibility revealed approximately the same behaviour for every frequency and pressure. A broad shoulder is seen at low temperatures in all datasets. However, without any dependence on frequency or pressure, it is difficult to describe its origin based simply on its shape and temperature. The thermal hysteresis visible in Fig. 4.23a is instrumental in nature (similarly to electrical resistivity data, where it was smoothed during the analysis), as all measurements were carried out in a temperature cycle of 300 K → 2 K→ 300 K and the pressure cell had a large heat capacity compared to its thermal conductivity.

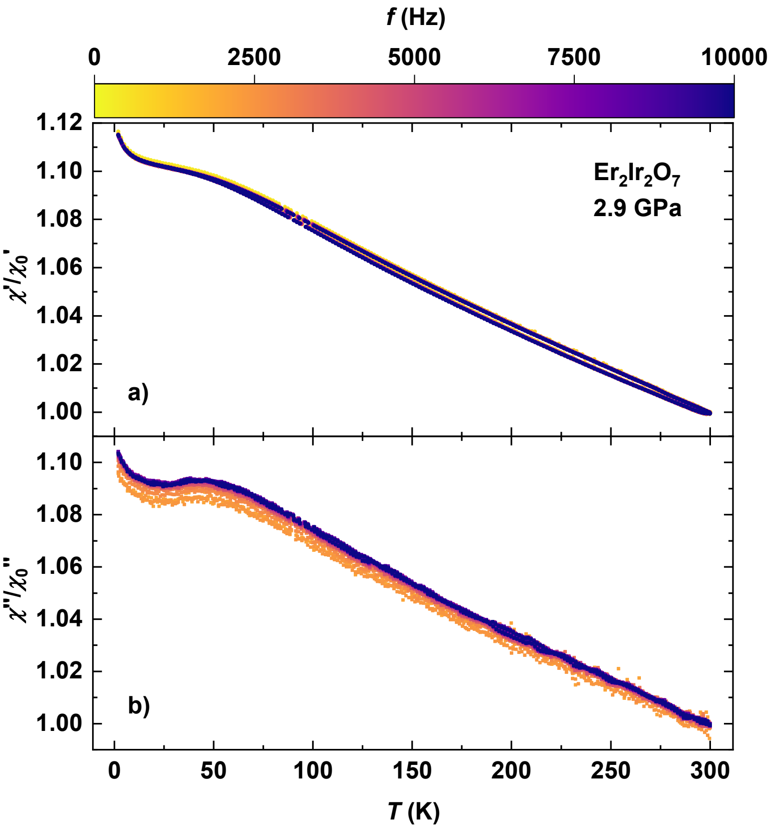

Fig. 4.23: Temperature and frequency dependance of a) the real part and b) the imaginary part of the AC magnetic susceptibility of $Er_2Ir_2O_7$ under 2.9 GPa of pressure. Relative values are presented. 30 different frequencies have been measured during the temperature sweep, in a range from 10 Hz to 9900 Hz.

4.3.4 Phase transitions

The AFM and metal-insulator transitions in $A_2Ir_2O_7$ compounds have been repeatedly reported to occur concomitantly (at/around the same temperature) [32,71,77,81]. There are, however, significant differences between the shape of the anomalies in, e.g., electrical resistivity or specific heat data of light- and heavy-rare-earth $A_2Ir_2O_7$ iridates (more studies done on light-rare-earth members). To understand the nature of these transitions and their interconnections, we focus on the shape of the transitions in different temperature-dependent experiments. As the temperatures of these anomalies can be sample dependent, it is difficult to compare results of different techniques and different scientific groups. Consistency is maintained in measuring the same sample using different methods. A comparison between the magnetic susceptibility, specific heat, and electrical resistivity data of the $Dy_2Ir_2O_7$ powder sample (from the same batch) is presented in Fig. 4.24.

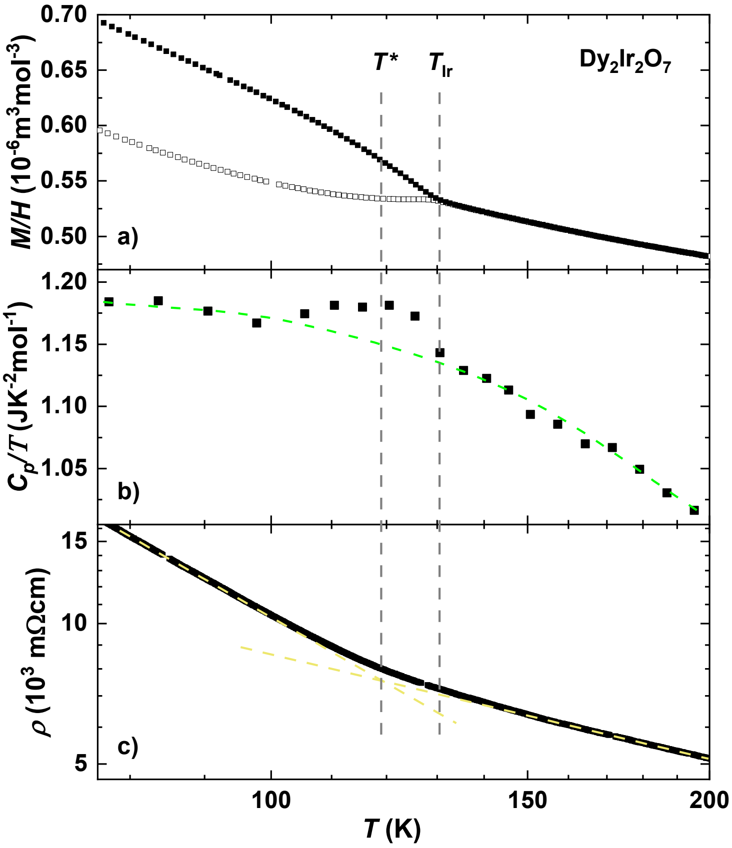

Fig. 4.24: Anomalies of the $Dy_2Ir_2O_7$ powder sample measured with temperature-dependent a) magnetic susceptibility, b) specific heat, and c) electrical resistivity. The AFM order at T_{Ir} results in a bifurcation in magnetisation. At slightly lower temperatures, the broad bump in specific heat and a broad change of slope in electrical resistivity are centred around T^*. The magnetic susceptibility and specific data were previously published by our group in [97]. Electical resistivity data published in [110].

The AFM ordering temperature T_{Ir}, confirmed in multiple analogues by neutron diffraction experiments, is directly connected to the bifurcation in magnetisation. A certain FM contribution is created upon the formation of the AFM ordering, controlled by the cooling field and responsible for the bifurcation in magnetization (see Section *4.4 Antiferromagnetic domain structure*). The heat capacity anomaly has its onset approximately at T_{Ir}. No thermal hysteresis has been observed, pointing to the second-order transition. Normally, a magnetic anomaly in specific heat has an asymmetric shape; the critical temperature is determined as the inflection point right below the onset. However, the anomaly in Fig. 4.24 does not have a regular sharp shape. Similarly broad shapes were seen in other heavy-rare-earth members. Comparing the shape of the specific-heat anomaly with the results on other $A_2Ir_2O_7$ members, the anomaly seems sharper for lighter-*A* analogues [32] than for heavier-*A* members [55]. Finally, the semiconductor-insulator transition of heavy-rare-earth members is characterised by a change of slope of electrical resistivity which has a similar broadness and position as the anomaly in specific heat. In lighter-*A* members, the metal-insulator transition is determined more easily thanks to its sharpness. It seems that there is a connection between the anomalies in specific heat and electrical resistivity related to their sharpness/broadness. T^* marks approximately the middle of the anomaly in specific heat and electrical resistivity.

4.4 Antiferromagnetic domain structure

In the final section of the results, we move from structural properties and conductivity of powder samples under pressure to magnetic properties of $A_2Ir_2O_7$ single crystals. More specifically, DC magnetisation experiments were performed employing the MPMS instrument (Section *2.3.3 DC magnetisation*) on $Er_2Ir_2O_7$ and $Lu_2Ir_2O_7$ crystals. Moving from powder samples to single crystals enables us to also study the anisotropic magnetic properties of materials needed to elucidate, e.g., the origin of the FC-dependent magnetic response observed in magnetoresistivity measurements (Section *4.3.3 Application of high pressure*). Masses of the measured single crystals were 0.14 mg for $Lu_2Ir_2O_7$ and 0.09 mg for $Er_2Ir_2O_7$. Although some other samples had a larger mass, we selected clean samples (without nucleation of smaller grains on their surfaces) with distinguishable facets for the measurements, guaranteeing the quality of measured data and crystals' alignment in applied magnetic field.

4.4.1 Cooling-field-driven magnetisation

Similarly to the high-pressure electrical resistivity experiments, we focus on the same two members of the rare-earth series, $Er_2Ir_2O_7$ and $Lu_2Ir_2O_7$. With the same concept, we follow solely the response of Ir magnetism in $Lu_2Ir_2O_7$, whereas an additional contribution and interaction with magnetic Er^{3+} cations form the magnetic properties of $Er_2Ir_2O_7$. Both analogues exhibit a bifurcation between ZFC and FC magnetic susceptibility at the AFM ordering temperature T_{Ir} (Fig. 4.25ab). T_{Ir} has been estimated as the onset of the bifurcation, resulting in $T_{\mathrm{Ir}} = 128(3)$ K for the $Lu_2Ir_2O_7$ sample and

T_{Ir} = 120(6) K for the $Er_2Ir_2O_7$ crystal. Slightly higher values have been determined for our powder samples [13,98] (Table 4.5). In many cases, difficulties related to sample growth and Ir (or rare-earth) off-stoichiometries result in shifted AFM ordering temperatures [2,81,92].

The field dependence of magnetisation reveals a slightly anisotropic behaviour (Fig. 4.25cd). Although a saturation trend is followed, the 7 T magnetic field is not sufficiently strong to reach magnetic saturation; a further increase of magnetisation is expected in higher magnetic fields. The magnetisation reached at 7 T is much lower than the free-ion saturation value (1 μ_B for Ir^{4+} and 9 μ_B for Er^{3+}, i.e., twice as much per formal unit if one uses Fig. 4.25cd data for comparison). Specifically, approximately one third of the predicted value is reached. In fact, smaller magnetisation values are very common in these materials; that is, not to reach the free-ion saturation moment but rather to saturate at about one half of the estimated value. This is caused by the geometrical frustration of the pyrochlore structure and the

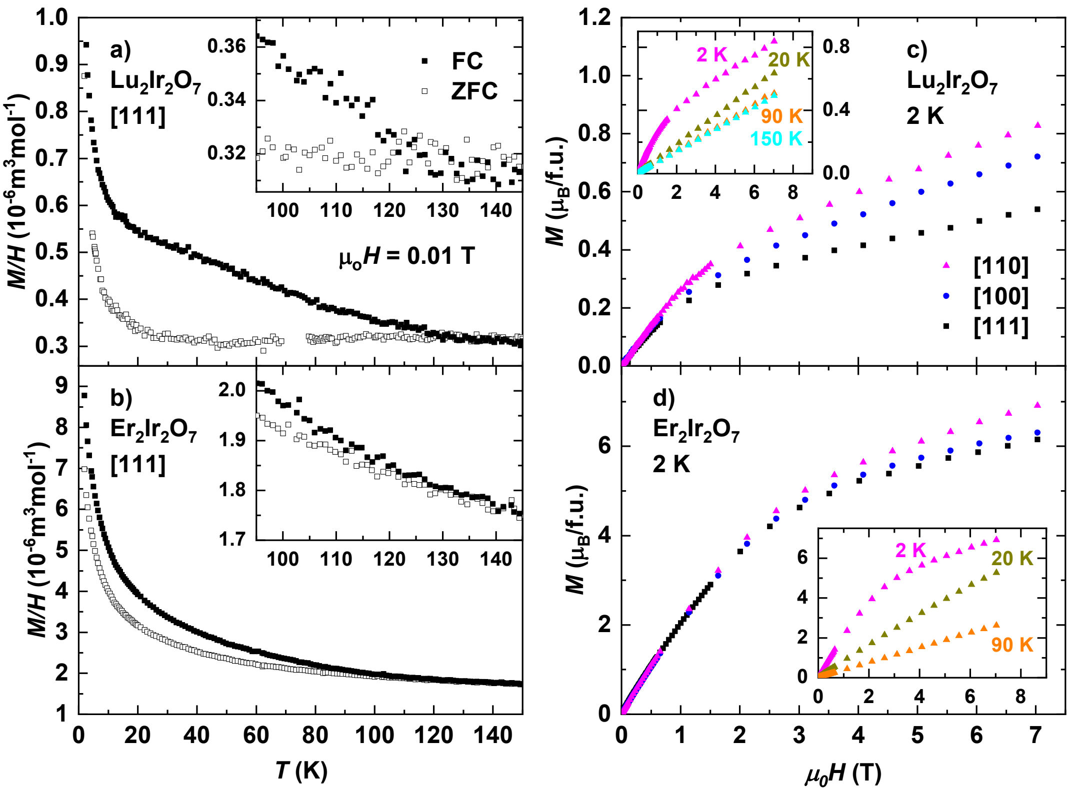

Fig. 4.25: Magnetisation characterisation of $Lu_2Ir_2O_7$ (top panels) and $Er_2Ir_2O_7$ (bottom panels) single crystals. a)-b) Temperature-dependent magnetic susceptibility along the [111] direction shows a bifurcation between the ZFC and 0.01 T FC regimens. The insets show a close-up view of the onset of the bifurcation. c)-d) Field-dependent magnetisation data measured at 2 K along the three main crystallographic directions. The insets portrait measurements along the [110] direction at different temperatures. Data published in [111].

anisotropy of the local magnetic moments [2,71,97]. Inspecting the magnetisation slope at 7 T, one-half saturation can eventually be reached in higher fields. Alternatively, the lower magnetic moment might be attributed to the Pb contamination of samples introduced during the synthesis process (Section *4.1.2 Single crystals*).

The magnetic anisotropy in both $Er_2Ir_2O_7$ and $Lu_2Ir_2O_7$ was revealed to be similar; that is, the highest magnetisation value was observed with a magnetic field applied along the [110] crystallographic direction and the lowest value along the [111] direction. A = Lu single crystal exhibits larger relative anisotropy, although the maximum difference between [110] and [111] magnetization is about ~0.3 μ_B compared to ~1 μ_B for A = Er iridate. Of course, the anisotropy is not related solely to the Ir sublattice; the molecular field of Ir influences the Er cations, which contribute to the total magnetisation. Although the Er sublattice is not ordered at 2 K (it orders with an easy-plane arrangement below 0.6 K [71]), its magnetic correlations are significant at this temperature. A naive explanation of the anisotropy is connected to the AIAO order of the Ir sublattice. As all Ir magnetic moments point along one of the <111> directions, it is difficult to rotate the spins by the [111] magnetic field. On the other hand, two out of four spins in each tetrahedron are aligned perpendicular to the [110] crystallographic direction, making them more susceptible to the magnetic field along that direction. The insets in Fig. 4.25cd show isothermal magnetisation at several temperatures. At temperatures $T \geq 20$ K, almost linear behaviour is followed up to 7 T, compared to the saturating tendency at 2 K.

The bifurcation between the ZFC and FC magnetic susceptibility is usually seen in FM phases or in short-range-ordered magnetic phases (such as spin ice or spin glass). The latter case is related to frequency-dependent transitions. In the case of $A_2Ir_2O_7$ iridates with confirmed long-range AFM order, the bifurcation is attributed to a small FM contribution present in the AFM phase. Specifically, the formation of the AFM domain structure can create pinned uncompensated Ir moments responsible for this FM contribution. In this section, we describe three approaches capable of investigating the aforementioned small FM contribution.

The first approach is to compare the field dependencies of magnetisation measured on ZFC and FC samples. That is, ZFC, FC, and -FC regimens are compared. After (zero-)field-cooling the samples, field sweep cycling 0 T → 7 T → -7 T → 0.2 T was performed. At first glance, all regimens produce basically the same behaviour, showing no hysteresis (main panels of Fig. 4.26). However, upon closer inspection (presented insets), a small shift between the data is observed. ZFC regimen produces a state with zero net magnetisation at zero applied field. In comparison, 7 T FC regimen creates a state with a positive nonzero magnetic signal in zero applied field (remanent magnetisation). Similarly, the opposite cooling field (-7 T FC) creates a negative magnetic signal with the same magnitude. We denote this vertical shift between ZFC and FC regimens as M_{sh}. Within all measurements, the magnetic field of ±7 T was not strong enough to fully disturb this FM contribution. That is, once the sample was cooled in 7 T, magnetisation always showed a constant positive M_{sh} (red data in

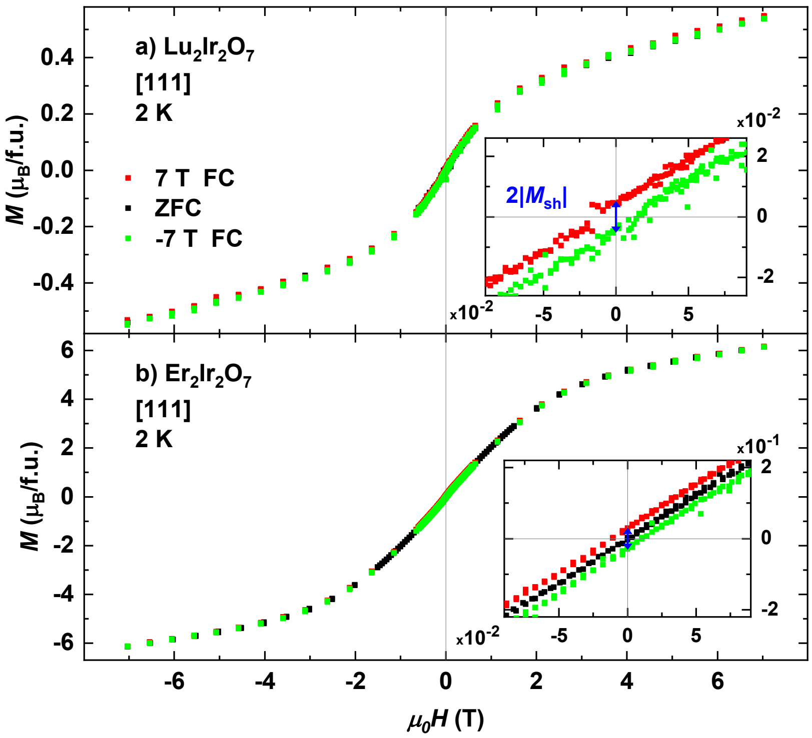

Fig. 4.26: Field-dependent magnetisation of a) $Lu_2Ir_2O_7$ and b) $Er_2Ir_2O_7$ single crystals at 2 K along the [111] direction. Three cooling regimens were followed. The insets show the low-field region, emphasising the small shift in magnetisation denoted as M_{sh}. Data published in [111].

Fig. 4.26) even after applying the opposite -7 T field at 2 K. As the FC and -FC regimens produced opposite magnetic signals with the same magnitude, the difference between the FC and -FC data is approximately $2|M_{sh}|$ (inset of Fig. 4.26a). M_{sh} characterises the small (yet robust) FM component embedded in the AFM phase. For both studied crystals, the magnitude of M_{sh} is around 2 orders of magnitude smaller than the 7 T field-induced magnetisation. With increasing temperature, M_{sh} decreases (Fig. 4.28). Besides the robust vertical shift in magnetisation, no hysteresis has been observed in the data. This means that the FM contribution is not (significantly) impacted by a magnetic field of 7 T.

To investigate M_{sh} not only in zero field, but also in applied field, we subtracted the magnetisation from the FC and -FC regimens in Fig. 4.26. Results of $2|M_{sh}|$ along the three crystallographic directions and at both 2 K and 20 K are presented in Fig. 4.27. Although the overall quality of the subtracted data is heavily impeded by instrumental noise, clear and consistently similar tendencies are seen along all measured directions. Thus, the first observation is that the behaviour of the FM component M_{sh} is isotropic. All data from the $Lu_2Ir_2O_7$ measurement show an approximately constant M_{sh} in the applied field. That is, the difference between curves in Fig. 4.26a is indeed a constant vertical shift in magnetisation, seemingly unaffected by the applied field. A slightly smaller M_{sh} (but still robust against field) is seen at

20 K. A very similar behaviour is observed at 20 K for $Er_2Ir_2O_7$. However, a clear suppression of 2|M_{sh}| with applied field is observed at 2 K (Fig. 4.27bdf). Both FC and -FC curves slowly approach the ZFC curve in higher fields in Fig. 4.26b. This phenomenon is attributed to the Er moments and interactions between them, which are most active at the lowest temperatures. At 2 K, a significant part of the magnetic signal M_{sh} is predicted to originate from Er moments influenced by the Ir molecular field. However, unlike Ir spins pinned by the AFM domain structure, Er spins can be rotated by a field of 7 T. At 20 K, the contribution of Er magnetism to M_{sh} is comparable to Ir magnetism, therefore no significant evolution with field is followed. Importantly, suppression of M_{sh} for $Er_2Ir_2O_7$ in high field is reversible; removing the field results in the return of the same M_{sh}.

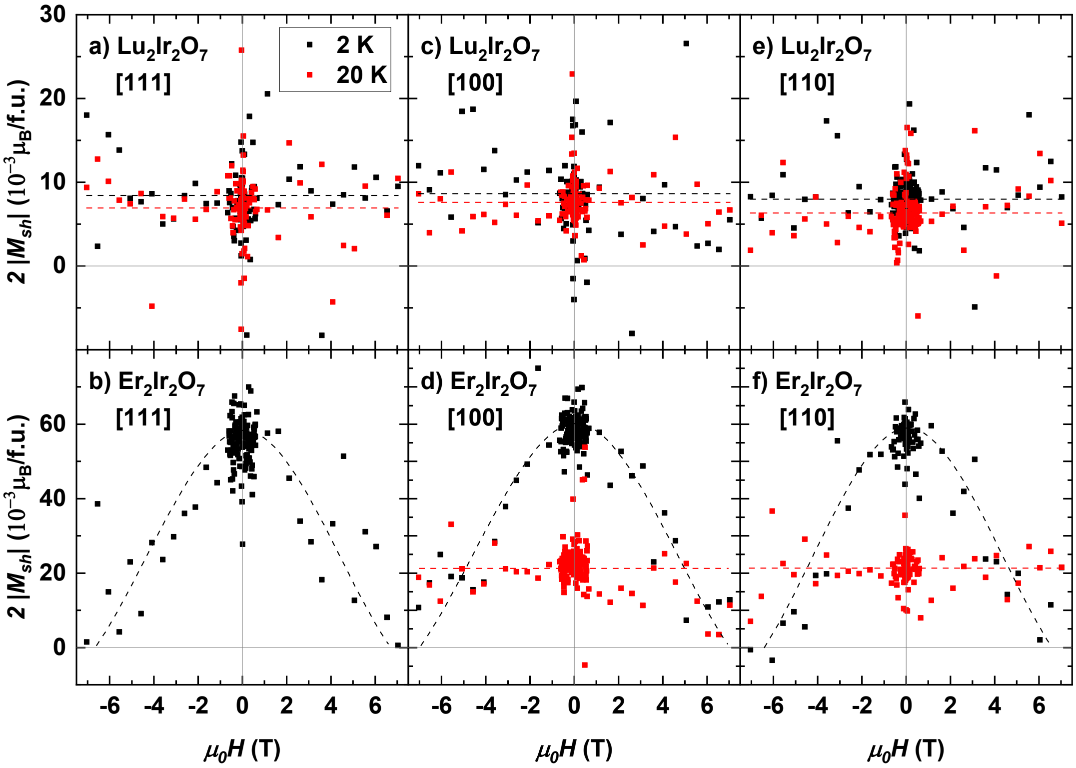

Fig. 4.27: Field dependence of the vertical shift in magnetisation between the 7 T FC and -7 T FC regimens (subtraction of data in Fig. 4.26). The top panels show the results from $Lu_2Ir_2O_7$ single crystals and the bottom panels show results from $Er_2Ir_2O_7$ single crystals. Data at 2 K and 20 K are presented for the three main crystallographic axes. Dashed curves are guides to the eye. Data published in [111].

The second approach to studying the FM contribution is to perform temperature scans of the remanent magnetisation (M_{sh}). The measurement protocol is presented in Fig. 4.28b. First, the magnetic field is applied at a temperature reasonably above T_{Ir} (150 K for our measurements). Then the sample is field-cooled to 2 K, and the magnetic field is removed. Finally, the magnetic signal from the sample is measured in a zero field during heating. M_{sh} is highest at low temperatures and monotonously decreases upon heating, completely vanishing at T_{Ir} (Fig. 4.28ab). The thermal dependence of M_{sh} is in agreement with the values of M_{sh} determined from isothermal measurements at 2 K, 20 K, 50 K, and 90 K (2 K data in Fig. 4.26). Yet again, M_{sh} behaves isotropically for both A = Lu and Er members. Lu_2Ir_2O7 exhibits lower M_{sh} values than $Er_2Ir_2O_7$ in the whole temperature region. The largest difference between the two is observed at the lowest temperatures. Whereas A = Lu data show moderate change below ~20 K, A = Er data exhibit a rapid increase of M_{sh} down to 2 K. As mentioned previously, the magnetic contribution of the Er sublattice to total magnetic signal becomes prominent at these low temperatures. Of course, the influence of the Ir molecular field on the Er sublattice is present even at higher temperatures (M_{sh} above 20 K is still considerably higher for the A = Er analogue, although the difference diminishes with increasing temperature). Importantly, the strength of the cooling field affects the magnitude of M_{sh}. As seen in Fig. 4.28c, a larger cooling field induces a higher M_{sh}, although the overall shape remains unchanged.

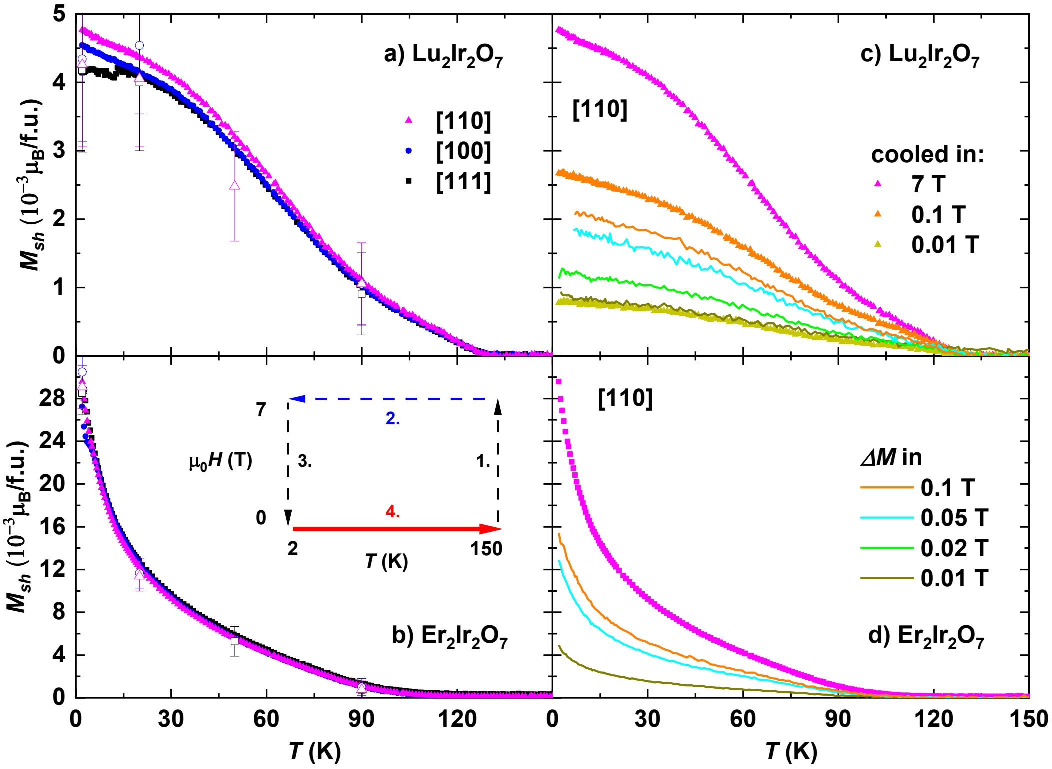

Fig. 4.28: Temperature dependence of FM signals measured along the main crystallographic axes for $Lu_2Ir_2O_7$ (top panels) and $Er_2Ir_2O_7$ (bottom panels) single crystals. a)-b) Residual magnetisation M_{sh}. The measurements follow the protocol illustrated in panel b) (7 T FC). c)-d) M_{sh} from several FC regimens is compared to the difference in bifurcation (see Fig. 4.29) denoted as ΔM. Data published in [111].

The third approach is to study the bifurcation of the ZFC-FC magnetisation. Instead of plotting the data as magnetic suspectibility, inspecting the magnitude of the bifurcation by subtracting the ZFC and FC magnetisation is useful. We denote this difference as *ΔM* and compare it to M_{sh} in Fig. 4.28cd. Similarly to M_{sh}, a higher cooling field induces a larger *ΔM* signal. For both studied analogues, the shape of M_{sh} and *ΔM* is identical. The magnitudes are comparable in most cases and fit perfectly for the 0.01 T FC datasets of $Lu_2Ir_2O_7$. Therefore, we attribute the ZFC-FC bifurcation to the same FM contribution followed by two aforementioned approaches.

Typically, the temperature dependence of magnetic susceptibility is analysed. In the paramagnetic phase of investigated materials, all low-field magnetic susceptibility data collapse into the same curve. In the AFM phase, the bifurcation in magnetic susceptibility monotonously closes with higher applied field. However, this is misleading, as the magnetisation responsible for the bifurcation (*ΔM)* actually increases with the applied field. Therefore, to analyse the FM contribution responsible for the bifurcation, it is useful to look at the magnetisation values instead of susceptibility and subtract the ZFC-FC difference *ΔM*.

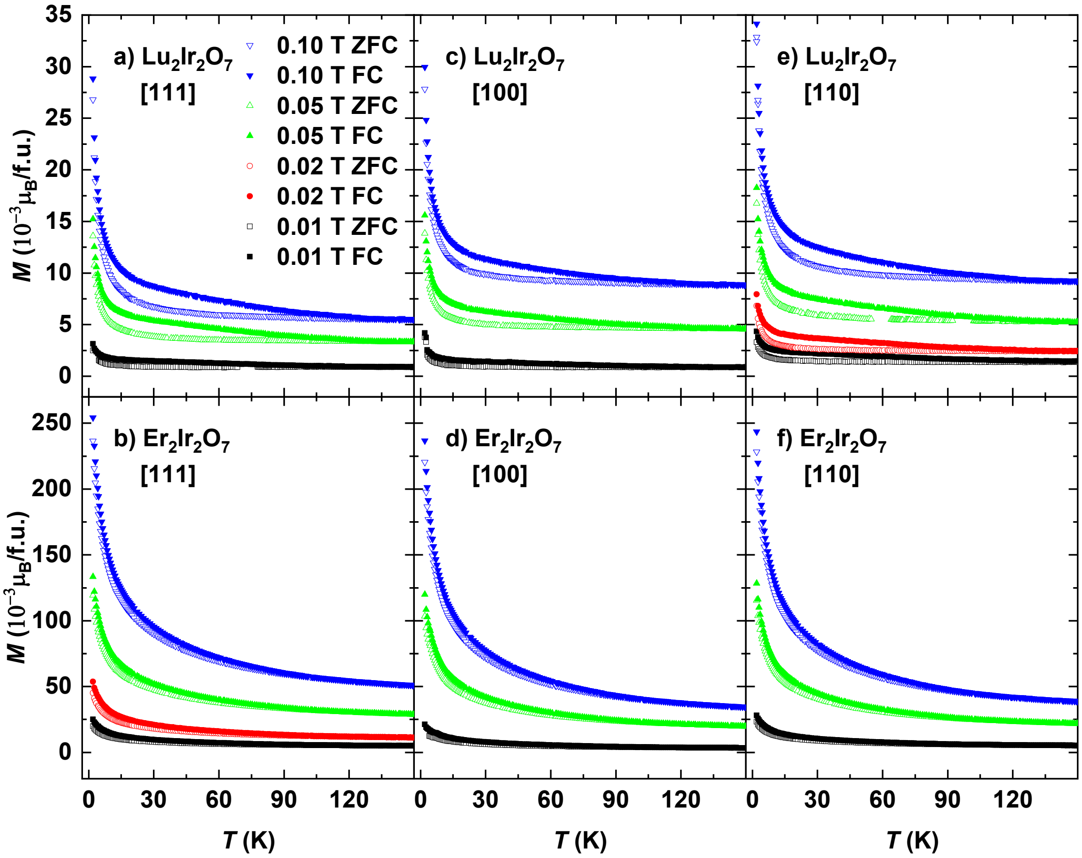

Fig. 4.29: All temperature-dependent magnetisation measurements on the $Lu_2Ir_2O_7$ (top panels) and $Er_2Ir_2O_7$ (bottom panels) single crystals. The magnetisation signal measured in the applied field of 0.01 T, 0.02 T, 0.05 T, and 0.1 T after ZFC and FC protocol (recalculated to Bohr magnetons per formal unit). Magnetic field is applied along a)-b) [111], c)-d) [100], and e)-f) [110] directions. Data published in [111].

Overall, all measured magnetisation curves displayed similar behaviour along all three main crystallographic directions and using cooling fields from 0.01 T to 0.1 T (Fig. 4.29). In all cases, the bifurcation between ZFC and FC magnetisation was observed at approximately the same temperature. Or rather, the error of determining T_{Ir} from the onset of the bifurcation is greater than the changes of T_{Ir} with magnetic field. Similarly, even when cooling down in 2 T magnetic field, no clear shift of the bifurcation temperature in $Lu_2Ir_2O_7$ was observed (Fig. 4.30). Therefore, approximately the same T_{Ir} is expected for the case of zero magnetic field.

Inverse magnetic susceptibility was investigated to determine the effective magnetic moment in the paramagnetic phase. Unfortunately, the small single crystals of $Er_2Ir_2O_7$ and $Lu_2Ir_2O_7$ (results above) displayed a weak magnetic signal at higher temperatures compared to the diamagnetic response of the sample environment. Therefore, to increase the magnetic signal from the samples, sets of multiple single crystals (glued together) were measured at once. They weighted 7.68 mg for $Lu_2Ir_2O_7$ and 3.43 mg for $Er_2Ir_2O_7$, increasing the mass by more than one order of magnitude compared to individual crystals. As individual single crystals were not oriented with respect to each other and generally of worse overall quality (crystals from the same batch also containing crystal clusters), the measured sample is considered quasi-polycrystalline.

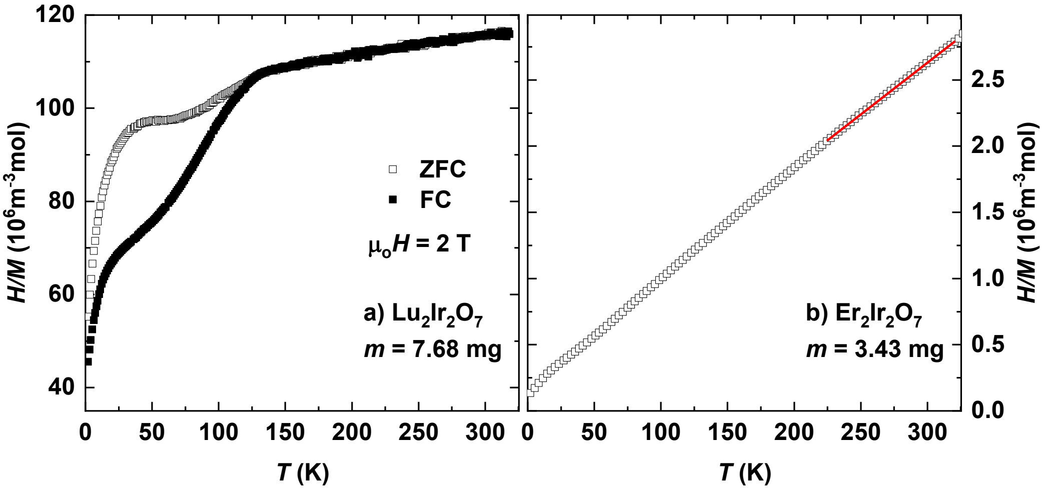

Fig. 4.30: Temperature dependence of inverse magnetic susceptibility of a) $Lu_2Ir_2O_7$ and b) $Er_2Ir_2O_7$. A mixture of multiple randomly-oriented single crystals of the same type was measured at once to obtain a higher measurement mass. Magnetisation in 2 T field was measured in ZFC and FC regimens. The red line represents the Curie-Weiss fit of the high-temperature region. Data published in [111].

The strategy was successful for the $Er_2Ir_2O_7$ analogue, which exhibited linear behaviour of inverse susceptibility in a wide temperature range (Fig. 4.30b). The high-temperature region (red line) was fitted by the Curie-Weiss law, resulting in the Curie-Weiss temperature $\theta_{\mathrm{CW}} = -36.4$ K and the effective magnetic moment $\mu_{\mathrm{eff}} = 9.0\ \mu_{\mathrm{B}}$.

Based on the free-ion model, estimated values of the effective moment are 1.73 μ_B for Ir^{4+} and 9.58 μ_B for Er^{3+}. The fitted effective moment is smaller than expected, however, comparable to our results on CsCl-flux-grown powder sample with $\mu_{eff} = 9.12$ μ_B and $\theta_{CW} = -26$ K [13,55]. Therefore, even in the case of a set of single crystals with lesser quality, the nonmagnetic lead substitution is not large enough to significantly affect the absolute magnetisation signal of $Er_2Ir_2O_7$. On the other hand, despite the larger mass of the $Lu_2Ir_2O_7$ sample, the magnetic signal from Ir was still comparable to the signal of the sample environment at high temperatures (Fig. 4.30a). Thus, the high-temperature region could not be reasonably modelled using the Curie-Weiss law. The ZFC-FC bifurcation is also significant for $Lu_2Ir_2O_7$ in 2 T field.

4.4.2 Domain wall model in single-crystal $A_2Ir_2O_7$

In the last section of the results, we focus on the theoretical explanation of the measured FM contribution inside the AFM bulk of $A_2Ir_2O_7$ iridates. For most analogues of the rare-earth series, long-range AFM AIAO magnetic structure has been determined (*A* = Nd, Sm, Eu, Tb, Yb, Lu) [9,10,74,76,94,95]. Most probably, both $Er_2Ir_2O_7$ and $Lu_2Ir_2O_7$ samples possess the same AIAO order below their bifurcation temperature. However, the picture becomes complicated after considering a possible AFM domain structure. Besides the all-in-all-out (AIAO) order, an analogous all-out-all-in (AOAI) order must be considered. The AIAO and AOAI types are equally energetically favourable and bound by time-reversal symmetry. Therefore, the bulk AFM structure of iridates is considered to accommodate a finite set of AIAO and AOAI domains.

Focussing on two neighbouring AIAO and AOAI domains, a certain amount of uncompensated net magnetisation is expected to be created at the interface between these domains (see simple examples in Fig. 4.31 and Fig. 4.32). These uncompensated moments inside the domain walls are considered pinned (frozen) by the surrounding AFM domains. We connect these interfaces to the FM contribution observed in the magnetisation and magnetoresistivity data of the investigated iridates (Fig. 4.26 and Fig. 4.21). That is, we explain the existence of the FM contribution as the net magnetisation of the uncompensated moments of the DWs pinned by the AFM domains. The formation of the AFM domain structure when cooling through T_{Ir} is crucial for forming the FM contribution. In the case of the ZFC regimen, the system orders without any preference to magnetic orientation, as no field is present. As a result, domains are created at random, including the domain walls. The net magnetisation created by the random individual DWs is therefore expected to sum up into a zero FM contribution, in accordance with our data. On the other hand, during the field-cooled regimen, the domain structure is created while energetically favouring the uncompensated moment along the applied field. As a result, the small FM contribution is pinned and nonzero along the cooling field. The symmetrically opposite net magnetisation is created in the -FC regimen. Once the domain structure is established at T_{Ir}, altering it by an applied field at lower temperatures becomes progressively more difficult.

In general, there are theoretically countless ways of forming these DWs, from simple cases of planar DWs to cases with complex shapes, moments, and thicknesses. Additionally, in real material, defects in the structure must be considered, especially as nucleation centres during the creation of the domain structure. Here, we introduce instances of the DWs in a very simplified manner. We consider only DWs with a simple planar shape containing one or two layers of Ir tetrahedra. With these restrictions, it is possible to create DWs along the three main crystallographic planes,

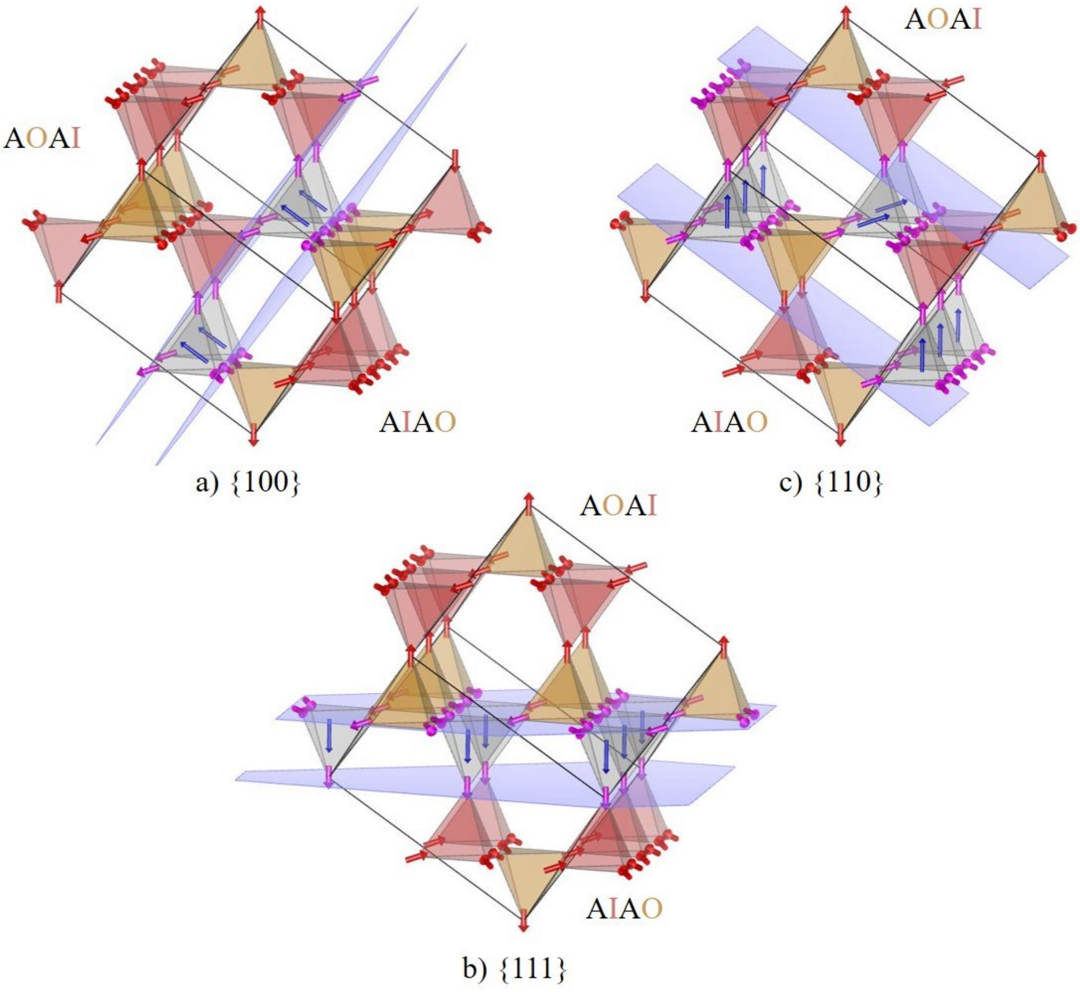

a) {100}

c) {110}

b) {111}

Fig. 4.31: Illustrations of the magnetic domain walls trapped between AIAO and AOAI AFM domains in $A_2Ir_2O_7$ iridates (purely the Ir sublattice). Only the most basic examples are presented, characterising domain walls with the three main planar orientations (for simplicity, notation of equivalent planes {100}, {111}, and {110} is used) with net magnetisation perpendicular to the DW. Tetrahedra with all spins pointing in and all spins pointing out are red and yellow, respectively. The grey tetrahedra inside the DWs (characterised by blue planes) have an uncompensated magnetic moment depicted by blue arrows. Spins contributing to uncompensated magnetic moments are depicted by pink arrows, in comparison to the red arrows depicting spins inside the AIAO/AOAI domains. Illustration published in [111].

with the net magnetisation perpendicular to the DW plane. Uncompensated moments directed along <100> can be created by Ir tetrahedra with the 2-in-2-out order (Fig. 4.31a). Similarly, one layer of 3-in-1-out (or 3-out-1-in) tetrahedra creates net magnetisation along <111> in Fig. 4.31b. Using only Ising spins, there is no way of producing an uncompensated moment along <110> using one Ir tetrahedron. Hence, we use a combination of 3-in-1-out tetrahedra in two layers to create the desirable net magnetisation direction (Fig. 4.31c). We point out the seemingly fragile construction of the monolayer DWs. For example, the {111} DW (Fig. 4.31b) can be moved to the next layer of tetrahedra below the current one if all the spins on the bottom of the layer are flipped upward. This results not only in the shift of the DW, but also in a complete flip of the created net magnetisation (pointing upward instead of downward). Thus, much flexibility is present during the formation of the DWs. Importantly, once the domain walls are constructed, flipping the entire layer of spins becomes very difficult.

Using the same approach, we also attempt to describe the cases with net magnetisation parallel to the DW plane. This is a trickier problem, as the antisymmetry connected to the uncompensated moments cannot be used to cross from the AIAO to the AOAI domain naturally. Instead, antisymmetry both parallel and perpendicular to the DW must be introduced, which can be done only with competing moments in the DW, such as in the case of Fig. 4.31c. That is, uncompensated moments with the same direction (case of Fig. 4.31ab) seem no longer applicable to this problem. Using two competing layers of 3-in-1-out (3-out-1-in) tetrahedra, it is possible to form net magnetisation along <100> and <110> directions which are concomitantly parallel to the DW plane (Fig. 4.32). However, in these cases, the net magnetisation points in

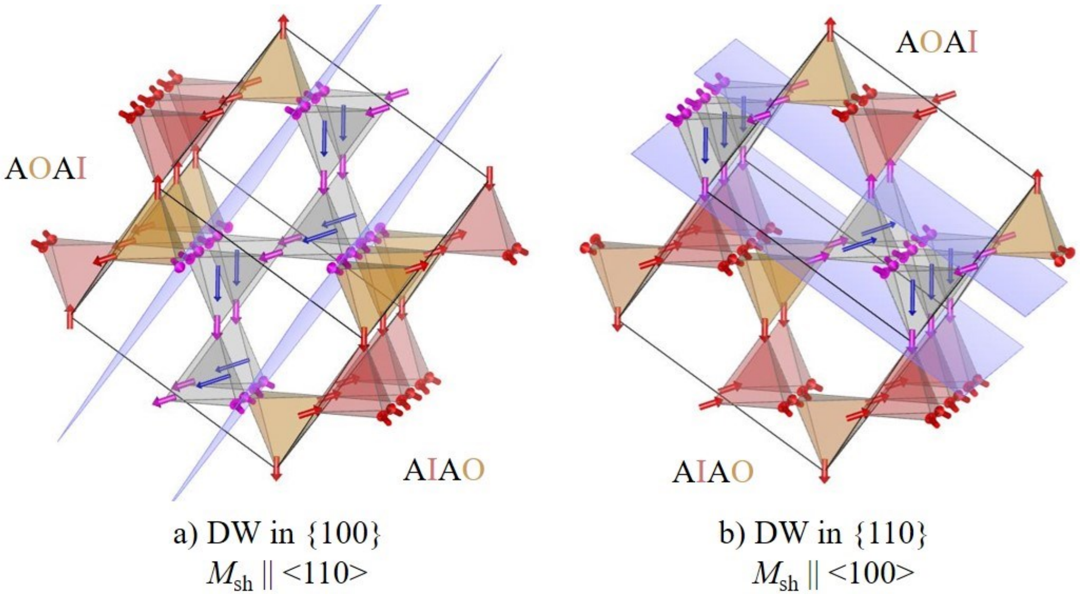

a) DW in {100}
$M_{\mathrm{sh}} \parallel$ <110>

b) DW in {110}
$M_{\mathrm{sh}} \parallel$ <100>

Fig. 4.32: Illustrations of the magnetic DWs with net magnetisation parallel to the DW plane. a) The DW is characterised by the {100} planes, while the net magnetisation points along <110>. b) The DW is defined by the {110} planes and has a net magnetisation along <100>. The notation is the same as in Fig. 4.31.

<100> while the DW plane is {110}, or vice versa. We could not find any examples (similarly simple as the examples above) limited to two layers of tetrahedra which would follow the same net magnetisation and crystallographic plane. Moreover, net magnetisation along <111> seems even more troublesome to model parallel to its DW due to its three-fold symmetry compared to the <100> and <110> cases. The domain structure is most-likely composed of not only simple DWs with perpendicular net magnetisation (Fig. 4.31), but of other types of DWs as well. However, these alternative DWs have an increasingly higher complexity.

Finally, we connect the theoretical models presented in Fig. 4.31 to our experimental data. As the contribution of Er^{3+} cations is too complex to predict, we restrict the following calculations to the Ir sublattice and connect it to the data from $Lu_2Ir_2O_7$ only. First, we estimate the total net magnetisation signal produced by each of the presented model DWs. A single unit cell of the pyrochlore structure contains 16 Ir^{4+} cations which form a total of 8 tetrahedra. For simplicity, the spin of a single Ir^{4+} cation will be used as the unit in the following calculations. Each Ir^{4+} cation contributes 0.5 of magnetic moment to each of the two tetrahedra it is a part of. In total, each Ir tetrahedron, if fully polarised, holds a maximum moment of 2. As the net magnetisation of planar DWs depends on their size, we calculate the magnetisation per DW area. The total uncompensated moment created by a single DW with an area of a^2 (lattice parameter a) is calculated with an intuitive equation $M_{hkl} = n_{hkl}m_{hkl}$. Here, n_{hkl} is the concentration of tetrahedra in the (*hkl*) plane DW (number of tetrahedra per the area of a^2). m_{hkl} is the uncompensated magnetic moment of a single tetrahedron pointing along the [*hkl*] direction.

1) DW characterised by {100} planes. This case represents the simplest DW out of the three examples presented in Fig. 4.31. The thickness of the DW is $d_{100} = a/4$. When a single DW is crossing the unit cell, two out of eight tetrahedra in the unit cell are inside the DW. Therefore, per the area of a^2, only two tetrahedra form the DW ($n_{100} = 2$). Each of these tetrahedra contributes to the net magnetisation, ordered with the 2-in-2-out type. Each of the four spins on one uncompensated tetrahedron is oriented with the same angle to the perpendicular <100> direction. The projection of each spin equals to $\frac{1}{\sqrt{3}}$, which results in a moment $m_{100} = \frac{1}{\sqrt{3}}4\frac{1}{2} = \frac{2}{\sqrt{3}}$. Thus, the net magnetisation of the DW per area a^2 is $M_{100} = 2\frac{2}{\sqrt{3}} = \frac{4}{\sqrt{3}}$.

2) DW characterised by {111} planes. This case also utilises only a single layer of uncompensated tetrahedra (Fig. 4.31b). In comparison to the first calculation, the four moments in question are arranged in the 3-in-1-out (or alternatively 3-out-1-in) order. The thickness of the studied DW is $d_{111} = \frac{\sqrt{3}}{6}a$ (like the previous case, this is determined based on the orientation of the tetrahedra inside the unit cell). The {111} DW is thicker and has a higher concentration of tetrahedra per area than the {100} DW. Rather, we can simply use the fact that the concentration of tetrahedra in a volume is constant. Therefore, the concentration per area is linearly proportional to the thickness of the DW. Consequently, the larger thickness leads to a greater

concentration $n_{111} = \frac{d_{111}}{d_{100}} n_{100} = \frac{4}{\sqrt{3}}$. For a tetrahedron with uncompensated moment along the <111>, one of the four spins is parallel with a maximum contribution of 0.5. The rest are oriented with the same angle to the relevant <111>, having a projection of 1/6. Together, they result in $m_{111} = 1$, which means a total net magnetisation of $M_{111} = \frac{4}{\sqrt{3}} 1 = \frac{4}{\sqrt{3}}$ per a^2.

3) Lastly, the DW characterised by {110} planes. This case is more complex than the examples above, as a single tetrahedron cannot possess an uncompensated moment along <110>. Instead, two layers of tetrahedra with competing magnetic moments are employed (Fig. 3c). However, only half of the tetrahedra inside the DW have an uncompensated moment. Bearing this in mind, the calculation can be simplified by instead imagining only one layer composed of only uncompensated tetrahedra. Such a monolayer has a thickness of $d_{110} = \sqrt{2}a/4$. Once again, we can calculate the concentration proportionally to the first example. Out of the three examples, this domain wall is the thickest and hence has the highest concentration: $n_{110} = \frac{d_{110}}{d_{100}} n_{100} = 2\sqrt{2}$. Similarly to the {111} DW, the 3-in-1-out (3-out-1-in) order is present. However, we have to bear in mind the competition between the tetrahedra. Half of the tetrahedra have uncompensated moment pointing along the same direction, competing with the second half of the tetrahedra, ultimately creating a net magnetisation along the desired <110>. Therefore, every tetrahedron has a reduced moment following a projection $m_{110} = \frac{\sqrt{2}}{\sqrt{3}} m_{111} = \frac{\sqrt{2}}{\sqrt{3}}$. Once again, the total moment equals to $M_{110} = 2\sqrt{2}\ \frac{\sqrt{2}}{\sqrt{3}} = \frac{4}{\sqrt{3}}$ per a^2.

All three DW examples, despite having different thickness, magnetic moment per tetrahedron, or competing magnetisation, result in the same net magnetisation $\frac{4}{\sqrt{3}}$ Ir^{4+} moments per a^2. With a naive assumption that the FC regimens create only the types of DWs presented in Fig. 4.31, the calculations above support the idea of an isotropic FM component. Such a picture agrees very well with our experimental observation of M_{sh}, which showed only minimal anisotropy (Fig. 4.28). Considering also more complex DWs does not lead to similarly simple results. Even the examples presented in Fig. 4.32 result in different net magnetisation. Specifically, the first DW type (in {100} with M_{sh} || <110>) creates a total moment of $2n_{100} \frac{\sqrt{2}}{\sqrt{3}} m_{111} = 4\frac{\sqrt{2}}{\sqrt{3}}$, which is bigger than that of the previous three DWs. On the other hand, the second DW type (in {110} with M_{sh} || <100>) includes only one layer of tetrahedra, resulting in two-times smaller contribution $n_{110} \frac{1}{\sqrt{3}} m_{111} = 2\frac{\sqrt{2}}{\sqrt{3}}$, which is even smaller than that of the previous three DWs. Making any assumptions based on these more complex DWs is too ambitious for the current work. We limit further calculations to the three simple DWs types instead.

Knowledge of the net magnetisation produced by one DW can be used to estimate the number and size of DWs in the system, which is related to the number and size of the AFM domains. As all three presented simple types of DWs produce the same net magnetisation, we use the simplest example, the {100} DW, for further calculations. Being restricted to crude estimations, we introduce an unrealistic assumption: only DWs of this one type exist in the material. Nevertheless, even a very crude estimation of the domains' dimensions is useful. In the case of a single {100} DW crossing each unit cell in the material, two out of eight tetrahedra produce an uncompensated moment of $\frac{4}{\sqrt{3}}$ compared to the maximum (fully saturated) value of 16 Ir^{4+} magnetic moments. That is, a net magnetisation of approximately 14.4% of the full saturation is expected. In our data, the net magnetisation M_{sh} of $Lu_2Ir_2O_7$ reaches approximately 0.0023 μ_B/Ir^{4+} at temperatures near 0 K (Fig. 4.28a). The saturated Ir^{4+} moment of 1 μ_B is used, which is the predicted value for the free Ir^{4+} cation. Thus, the measured M_{sh} amounts to approximately 0.23% of the predicted saturated magnetisation. Taking into account only planar DWs perpendicular to the [100] direction, approximately every 63rd unit cell needs to host a DW to create the total net magnetisation measured in our data. The distance between these DWs (characterising the thickness of plate-like domains) is then estimated to be ~0.064 μm. We use the lattice parameter a = 10.1215 Å (single crystal diffraction) for this calculation. Understandably, wide plate-like AFM domains are not expected to be formed in the bulk. Assuming similar net magnetisation can be created in DWs parallel to the cooling field, cubic domains with dimensions of ~0.19x0.19x0.19 μm^3 are expected.

5. Discussion and prospects

Following the flow of the thesis, we start this chapter by discussing the structural properties of the $A_2Ir_2O_7$ iridates. These compounds proved to introduce a stable playground for investigating properties tightly connected with fine-tuning the pyrochlore structure. The only two free parameters (a and x_{48f}) of pyrochlore structure are tuneable by chemical and external pressure, significantly varying the electrical transport and magnetic properties of the material; not only related to the Ir sublattice, but also the rare-earth sublattice. Importantly, the pyrochlore structure was shown to be stable throughout the entire rare-earth series (A = Pr – Lu) and robust under pressures of at least 20 GPa. Increasing the atomic number of A decreases the lattice parameter a almost linearly. In contrast, a nontrivial increase of x_{48f} is followed. Applying external pressure decreases the lattice parameter a, while x_{48f} is not affected significantly. Detailed knowledge of compressibility, directly connected to structural parameters, is essential to compare chemical and external pressure. Unfortunately, we note a significant sample dependence of the $A_2Ir_2O_7$ properties studied throughout recent years by multiple groups. In this work, the investigated structural properties were obtained on CsCl-flux-grown powder samples; high consistency is expected when comparing results on these compounds synthesised by our scientific group. That is, samples from the same batch or produced by the same synthesis method were studied by multiple methods, and their properties were discussed in this thesis and several articles [13,55,97,98,109,110,117,118,130]. In contrast, inconsistencies, especially in absolute values of the physical properties, are unavoidable when comparing respective results, including our polycrystalline and single-crystalline data. Nevertheless, the trends followed in our data are consistent and expected to be qualitatively the same in all $A_2Ir_2O_7$ samples, irrespective of the synthesis method.

One of the main focusses of this work is the investigation of the metal-insulator (MIT), or rather, semiconductor-insulator transition in these materials. The precise nature of this transition and its connection to the AFM order and crystal structure are elusive. As we have shown in the Section *4.3.1 Electrical resistivity at ambient pressure*, none of the known models describe the data unambiguously; standard Mott or Slater behaviour is not well followed. A very similar situation was observed in $Cd_2Os_2O_7$ osmate, which crystallises in the same pyrochlore structure and reveals a concomitant MIT and AIAO AFM transition [31]. In these compounds, the nature of the MIT was described adapting the Slater mechanism, but not in a standard sense. One explanation uses a Lifshitz transition induced by the AIAO order [131], and the other parallels the Slater picture, but without Brillouin-zone folding [29]. Returning to $A_2Ir_2O_7$ iridates, the angle-resolved photoemission study on $Nd_2Ir_2O_7$ proposed an intriguing explanation; a continuous crossover from a Slater-like insulator just below T_{Ir} to a Mott-like insulator at the lowest temperatures [132].

Three main observations in our electrical transport data address the nature of the semiconductor-insulator transition. First, the observed transition is broad and continuous. The Slater model predicts a continuous character of the transition [28], whereas the Mott model expects a first-order transition, which typically results in a more abrupt change in electrical resistivity [31]. Second, the anomaly in electrical resistivity is always observed at/below the anomaly in magnetisation. Although the temperatures of the anomalies are difficult to pinpoint precisely, the bottom line is that T^* is not observed above T_{Ir} for any of the analogues. This observation agrees with all the publications about $A_2Ir_2O_7$ known to us. Furthermore, we highlight multiple chemical substitution studies of $Eu_2Ir_2O_7$, focused on investigating the Weyl semimetal state [79,80,133]. In all three studies, chemical substitution seemingly decouples the MIT and AFM order; T_{MI} is suppressed more than T_{Ir}, displaying a clear $T_{\mathrm{MI}} < T_{\mathrm{Ir}}$ behaviour. In the Slater model, the AFM order induces the MIT and, therefore, manifests at higher temperature ($T_{\mathrm{MI}} \leq T_{\mathrm{Ir}}$) [28]. On the contrary, the AFM order is created in the insulating state within the Mott model, typically far below the MIT ($T_{\mathrm{MI}} \geq T_{\mathrm{Ir}}$) [31]. Third, the studied heavy-rare-earth iridates behave as narrow-band semiconductors/insulators in the proximity of T_{Ir} (or T^*). Based on the activation law, the magnitude of the insulating gap size (~10^1 meV) is comparable to the temperature of the AFM transition (~10^2 K) for all studied analogues. This also favours the Slater model, as typical Mott insulators display charge gaps much larger than the associated transition temperatures [81]. All observations rule out the typical Mott insulator behaviour and agree with the Slater insulator model. Although creating a commensurate AFM order is one of the prerequisites of the Slater mechanism, the AIAO type of order present in $A_2Ir_2O_7$ iridates has a zero propagation vector. That is, the elementary unit cell is the same for both the crystal and magnetic structure. Without the periodic perturbation of the magnetic ions' potential, a standard Slater insulator cannot be formed.

All in all, typical Mott and Slater mechanisms are not fully applicable for explaining the MIT in the $A_2Ir_2O_7$ iridates. Nevertheless, multiple observations prefer the Slater mechanism. Thus, we propose a Slater-type mechanism on the pyrochlore lattice without Brillouin-zone folding, similar to the one used for the $Cd_2Os_2O_7$ analogue [29], to be responsible for the in the $A_2Ir_2O_7$ iridates. Potentially, a Slater-Mott crossover is present upon further cooling of the sample, as was proposed for the case of $Nd_2Ir_2O_7$ [132], but we cannot confirm or deny this claim based on our data. The case of heavy-rare-earth iridates seems more complicated due to the fact that these materials are already semiconducting in the paramagnetic state. The idea of a semiconductor-insulator transition is obscure and hardly discussed in the literature, as both semiconductors and insulators possess an energy gap. Therefore, it is difficult to determine a gap opening in a system which already has a gap. It is also noteworthy that distinguishing between the Slater and Mott mechanisms is a notoriously complex matter, which is illustrated by the example of the scientific dispute over the properties of $SrIrO_4$ [33,34]. In addition, the effects of domain walls also contribute to the complexity of the electrical transport properties ([29] and Section *4.4 Antiferromagnetic domain structure*).

Concomitantly with the AFM ordering of Ir moments, a slight structural anomaly was previously observed in the temperature evolution of XRD patterns and

Raman spectra of $Eu_2Ir_2O_7$ [69,76]. It has been proposed that the Ir-O-Ir bond angle and Ir-O bond length are important for stabilizing the AFM structure, which then stabilises the insulating phase [69]. However, only the monotonous behaviour of the x_{48f} parameter was followed in our temperature-dependent XRD data (Fig. 4.8). Although the fact that the larger x_{48f} (smaller Ir-O-Ir bond angle) favours the insulating state agrees with both our data and the results of Das et al. [69], the lack of observable anomalies in our x_{48f} data makes us sceptical about the local structural changes at T_{Ir}.

In our structural studies, we confirmed a monotonous contraction of the lattice parameter a and a monotonous increase of x_{48f} with an increasing atomic number of A. Therefore, systematics in the electrical resistivity data are expected when changing the rare-earth ion. However, sample dependence must be critically considered; that is, any off-stoichiometry, different shape factors, or the structural integrity of the powder pellets (grain distribution). Comparing multiple electrical resistivity studies, it is clear that sample quality and properties play a major role in the electrical transport properties of rare-earth $A_2Ir_2O_7$ iridates. A similar behaviour of electrical resistivity was observed in the A = Yb and Lu members synthesised by solid-state reaction [10,126] compared to our flux-grown samples. However, A = Dy and Ho samples grown by the solid-state reaction method [32] exhibited a far more insulating behaviour than our samples. Powders prepared using the one-shot wet chemical synthesis method exhibited electrical transport properties comparable to our data [77]. The most significant differences are observed between the powder and single-crystal electrical transport properties. The electrical resistivity of single crystals tends to be very sample-dependent. For example, $Dy_2Ir_2O_7$ single crystals grown by hydrothermal synthesis show an increase of electrical resistivity from ambient temperature down to 4 K of approximately 10 orders of magnitude [82]. On the other hand, $Ho_2Ir_2O_7$ single crystals grown by the KF flux method show an increase within only one order of magnitude [2]. These results are very different from our data of A = Dy and Ho members, which both exhibit an increase of about 4-5 orders of magnitude. As all of our powder samples were prepared by the same flux synthesis method, the systematics within the $A_2Ir_2O_7$ series are more reliable than comparing samples grown by different methods and groups. Any possible differences in the physical properties of our samples thus originate from their (slight) off-stoichiometry or the weight percentage of minority phases in their volume.

We can compare the impact of the chemical and external pressure on physical properties of rare-earth iridates discussing our $Er_2Ir_2O_7$ results. The pressure of 3 GPa increased T^* by more than 20 K in $Er_2Ir_2O_7$ (Fig. 4.19). If the AFM order and semiconductor-insulator transition are tied, the pressure dependence of T_{Ir} is expected to display a similar increase. Based on the compressibility data in Fig. 4.12, external pressure of 3 GPa reduces the volume of $Er_2Ir_2O_7$ by approximately 1.5%, which corresponds to the ambient-pressure volume of $Yb_2Ir_2O_7$. Thus, substituting Er by Yb in $Er_2Ir_2O_7$ has a similar effect on the lattice parameter a as the application of 3 GPa of pressure. However, based on previous magnetisation measurements, $Yb_2Ir_2O_7$ has T_{Ir} only about 3 K higher than $Er_2Ir_2O_7$ (Table 4.5). A clear inequivalence of chemical and external pressure is observed. Similarly, opposite effects of chemical and external pressure were observed in $Sm_2Ir_2O_7$ [73]. Assuming that the magnetic and electrical anomalies are affected mainly by the structure, not the magnetism of rare-earth ions, this observation highlights the importance of the x_{48f} parameter. After all, with the same lattice parameter a in both $Er_2Ir_2O_7$ under pressure and $Yb_2Ir_2O_7$ at ambient pressure, x_{48f} (not changing with applied external pressure) characterises the only difference in their crystal structures.

The $Er_2Ir_2O_7$ and $Lu_2Ir_2O_7$ samples showed an increasing T^* with external pressure (Fig. 4.19). We assume the semiconductor-insulator transition is caused by the AFM ordering, and as a consequence, T_{Ir} also increases with pressure. This is in agreement with the increase of T_{Ir} with pressure up to 2 GPa in the A = Eu member [134]. The AIAO order exists in these materials mainly due to electron correlation (Hubbard model) U/t and local Ising spin anisotropy [73]. Upon the application of pressure, the 5d bandwidth increases, the electron hopping strength t increases, and thus U/t decreases, suppressing the AFM state. This argument was used to explain the decrease in T_{MI} with pressure in $Sm_2Ir_2O_7$ [73]. On the other hand, x_{48f} influences the distortion of the oxygen cages and therefore the local Ising spin anisotropy. Increasing the atomic number of A reduces the lattice parameter a and increases T_{Ir}, which disagrees with the suppression of T_{Ir} due to reduced U/t. It seems that the stronger Ising anisotropy caused by the change of x_{48f} affects the magnetism more than the change of lattice parameter a. That is, increasing x_{48f} enhances the AFM phase. However, how does one explain the enhancement of magnetism with pressure seen in the A = Eu, Gd, Er, and Lu analogues in Fig. 4.19?

Based on our structural studies, x_{48f} does not change significantly with external pressure (Fig. 4.13), at least compared to chemical pressure. This only leaves the effect of the lattice parameter a, which supposedly suppresses the AFM state with pressure [73]. A theoretical study of $A_2Ir_2O_7$ iridates shows a calculation of the Neél temperature dependent on the Coulomb repulsion U [135]. Interestingly, for high U, the insulator phase is predicted to have a maximum T_{Ir}, which then decreases for even higher U. We speculate that the heavy-rare-earth iridates reside in this region of higher U, which explains the increase in T^* (T_{Ir}) with pressure. This also means a further application of pressure is expected to reach a maximum of T_{Ir}, followed by a steeper suppression of the AFM phase, similar to the behaviour observed in $Eu_2Ir_2O_7$ [134]. Such a picture is consistent with the crossover from the decreasing behaviour with pressure in light-rare-earth iridates to the increasing behaviour in A = Eu and heavier iridates. Despite heavy-rare-earth analogues crossing the theoretical maximum of T_{Ir} when the atomic number of A is increased (chemical pressure), the effect of Ising spin anisotropy overshadows this evolution, resulting in the monotonous increase of T_{Ir}.

Magnetoresistivity of the $Lu_2Ir_2O_7$ sample revealed an asymmetric linear contribution, ascribed to the FM net moment on the AIAO-AOAI interfaces. Magnitude of this contribution (represented by the coefficient α_{MR}) increases with applied external pressure (Fig. 4.22). Similarly to the increase of T^* with pressure, the increase of α_{MR} is the consequence of the enhancement of the AFM phase. That is, AFM state with higher T_{Ir} results in greater net magnetisation when cooled down, which creates larger asymmetric contribution to MR. Although we do not follow the pressure dependence of T_{Ir} directly, its increase with pressure is indirectly determined by the increase of both α_{MR} and T^*.

In addition to magnetisation and magnetoresistivity experiments capable of investigating the magnetic DW signal in $A_2Ir_2O_7$ iridates, there have been a few studies focused on investigating these DWs directly. In $Nd_2Ir_2O_7$, the increased electrical resistivity of DWs (compared to the AFM insulating bulk) was used to scan the DWs with microwave impedance microscopy [106]. The existence of DWs was also confirmed in $Cd_2Os_2O_7$ by employing resonant magnetic microdiffraction [107] and in $Eu_2Ir_2O_7$ using microscale Hall bars [108]. The dimensions of the AFM domains were estimated to be approximately in orders of micrometres (iridates [106,108]) or dozens of micrometres (osmates [107]). In comparison, our calculations estimate a domain size of ~0.19x0.19x0.19 μm^3 for $Lu_2Ir_2O_7$ (one order of magnitude smaller dimensions compared to previous results). In addition, our calculation employs the free-ion saturated Ir moment of 1 μ_B, which is probably larger than the real magnetic moment of Ir in the pyrochlore structure. Smaller magnetic moment of Ir would need to be compensated by even more DWs (smaller domains) to produce the measured signal of M_{sh} (observed in Fig. 4.28). A possible explanation for these differences is that the DWs are more twisted and convoluted in real material, with higher thickness and higher uncompensated moment per DW area, at least compared to our simple single-layer model DWs.

The magnetic signal of the domain walls M_{sh} with approximately the same magnitude as our data was previously observed in $Eu_2Ir_2O_7$ single crystal [92]. Several times smaller M_{sh} was revealed for A = Eu and Lu polycrystals [100,136]. Although having similar M_{sh} for both A = Eu and Lu single crystals makes sense, since both are characterised by only magnetic Ir^{4+} ions and a pyrochlore structure with similar structural parameters, we point out the high off-stoichiometry dependence of the bifurcation in ZFC-FC magnetisation in $A_2Ir_2O_7$ iridates [e.g. 81,92,136]. The magnitude of M_{sh} is directly tied to the bifurcation in ZFC-FC magnetisation (Fig. 4.28). With the stoichiometry playing a significant role in deciding the M_{sh} magnitude, we cannot reasonably ascertain whether the single-crystallinity of the sample enhances or suppressed M_{sh}. It is clear, however, that the ferromagnetic DWs can thrive even in polycrystalline iridate samples. A clear asymmetric magnetoresistance of the $Lu_2Ir_2O_7$ powder sample supports this claim (Fig. 4.21).

Although most publications on the magnetisation of $A_2Ir_2O_7$ iridates lean towards the domain wall model, concerns of off-stoichiometry gave rise to another interpretation of the small FM contribution. It was explained by the so-called FM droplets [100,136]. The magnetic impurities were considered; that is, the presence of nonmagnetic Ir ions (with either 3+ or 5+ valence) in the lattice. This model seems unlikely, considering multiple previous off-stoichiometry-focussed publications; deliberately introducing off-stoichiometry suppresses the ZFC-FC bifurcation in multiple publications [80,81,84,92,133], whereas we are aware of only two publications reporting an opposite trend [136,137]. Moreover, a single nonmagnetic impurity would be "pinned" in the same way in an AIAO domain, or point in the opposite direction in an AOAI domain. This scenario is more difficult to control by cooling field and it would promote anisotropy of magnetic properties, which disagrees with our data (Fig. 4.28). On the other hand, we note one significant inconsistency of the domain wall model. All magnetisation studies of iridates (including this study) promote the fact that a higher cooling field (FC sample) produces a larger FM component [e.g. 91,92,100]. According to the DW model, this means more DWs (or thicker ones) are created by higher cooling field. This is, however, inconsistent with the fact that higher cooling field created fewer yet larger domains in $Nd_2Ir_2O_7$; to the point of almost a single-domain structure for applied cooling field of 7 T [106]. Although the DW model is currently the most reasonable model for interpreting the magnetic phenomena of $A_2Ir_2O_7$ iridates, we cannot exclude a better model will arise in the near future.

Finally, we discuss the future prospects, focussing on the topic of $A_2Ir_2O_7$ iridates. Regarding the structural studies, we believe that not much more can be investigated about these compounds' compressibility (lattice parameter), as our study covers most of the systematics of the rare-earth series. However, a greater understanding of the behaviour of x_{48f} is essential for understanding the subtle structural connections to the AFM ordering and in turn to conductive properties. It is concerning that our data show no anomaly in x_{48f} despite the appearance of an anomaly in a previous report on $Eu_2Ir_2O_7$ [69]. Electrical resistivity measurements at ambient pressure complete the basic picture of the electrical transport properties of $A_2Ir_2O_7$ iridates. However, it would be highly desirable to apply external pressure higher than 3 GPa to see if a maximum of T_{Ir} (T*) can be discovered for the heaviest members and confirm the theory of heavy-rare-earth iridates residing in the high-U region. Either magnetisation or MR experiment should prove efficient in determining T_{Ir}. Alternatively, the temperature dependence of resistivity and T* can indirectly follow T_{Ir}. It would also be interesting to test on iridates a similar experiment done by Feng et al. on $Cd_2Ir_2O_7$ [29] to filter out the MR contribution from DWs and obtain temperature dependence of the bulk Hall coefficient. Angle-resolved photoemission spectroscopy measurements are also desirable to shed light on the band structure of $A_2Ir_2O_7$ iridates around T_{Ir}, similarly to the results in [132]. Although the domain wall model explains most of the anomalous magnetic properties of $A_2Ir_2O_7$ iridates, it is crucial to resolve the issue of seemingly larger domain formation in a higher cooling field compared to the associated increasing M_{sh}. For this reason, microscopic measurements capable of mapping and distinguishing between individual domains and DWs are essential. Of course, for all these future experiments, it is crucial to have high-quality crystals (preferably single crystals) because it is clear that off-stoichiometry can greatly affect their properties. Therefore, the creation of a uniform and consistent preparation route for $A_2Ir_2O_7$ iridate single crystals would greatly benefit the scientific community.

6. Conclusions

The structural, magnetic, and electron transport properties of rare-earth $A_2Ir_2O_7$ iridates have been thoroughly investigated at low temperatures, in high magnetic fields, and under high external pressure. Structural and electrical transport properties were studied on CsCl-flux-grown polycrystalline samples. Magnetisation experiments were also performed on PbF_2-flux-grown single crystals.

The pyrochlore structure was revealed to be stable down to 4 K (or 25 K) and up to 20 GPa of pressure for all investigated members. In addition, based on the range of the covered rare-earth analogues (A = Pr, Sm, Dy, Ho, Er, Tm, Yb, and Lu), we conclude that the pyrochlore structure stability holds for the whole rare-earth series. Compressibility data allow systematic comparisons of external and chemical pressure that apply to both past and future studies. The second free structural parameter x_{48f}, characterising the local distortion of the pyrochlore structure, increases with both cooling and chemical pressure (increasing the atomic number of A), but stagnates with the external pressure application.

Electrical resistivity measurements at ambient pressure revealed a broad transition from a semiconducting to an insulating state for the studied heavy-rare-earth iridates (A = Dy, Ho, Er, Tm, Yb, and Lu). The data were analysed in the frame of the Arrhenius, Mott, power-law, and Slater models. The present narrow gap in the electron structure is believed to be induced by the AIAO antiferromagnetic ordering of the Ir sublattice in the framework of the Slater mechanism without Brillouin-zone folding. Applying high external pressure on A = Er and Lu members showed a systematic shift of the semiconductor-insulator transition to higher temperatures. The magnetoresistivity of $Lu_2Ir_2O_7$ displayed a linear asymmetric contribution controlled by the cooling field. The magnitude of this contribution, discussed as being connected to the AFM domain structure, monotonously increases with the application of pressure. Heavy-rare-earth iridates were proposed to reside in the high-U region, where pressure initially enhances the AFM insulating state. A maximum of T_{Ir} followed by a suppression of the AFM insulating phase is expected at higher pressures.

Both A = Er and Lu single crystals revealed a small FM signal in the AFM phase. Three approaches of investigating this FM contribution were presented and followed experimentally. The domain wall model was employed to explain the nature of the FM signal, controllable by cooling field and extremely robust against applied magnetic field at low temperatures. The results, including the almost isotropic behaviour of the FM contribution, were collaborated by calculating the size of the related moments and the number of the most basic types of domain interfaces in the investigated sample. The calculated dimensions of the AFM domains in $Lu_2Ir_2O_7$ are approximately one order of magnitude smaller than the previous experimental values revealed in the independently synthesised A = Nd and Eu single crystals.

Bibliography

[1] X. Liu, J.-W. Kim, Y. Wang, M. Terilli, X. Jia, M. Kareev, S. Peng, F. Wen, T.-Ch. Wu, H. Chen, W. Hu, M. H. Upton, J. Kim, Y. Choi, D. Haskel, H. Weng, P. J. Ryan, Y. Cao, Y. Qi, J. Guo, and J. Chakhalian, Chiral Spin-Liquid-Like State in Pyrochlore Iridate Thin Films, arXiv:2403.06170 (2024).

[2] M. J. Pearce, K. Götze, A. Szabó, T. S. Sikkenk, M. R. Lees, A. T. Boothroyd, D. Prabhakaran, C. Castelnovo, and P. A. Goddard, Magnetic Monopole Density and Antiferromagnetic Domain Control in Spin-Ice Iridates, *Nat. Commun.* **13**, 444 (2022).

[3] J. S. Gardner, M. J. P. Gingras, and J. E. Greedan, Magnetic Pyrochlore Oxides, *Rev. Mod. Phys.* **82**, 53 (2010).

[4] J. E. Greedan, Frustrated Rare Earth Magnetism: Spin Glasses, Spin Liquids and Spin Ices in Pyrochlore Oxides, *J. Alloys Compd.* **408–412**, 444-455 (2006).

[5] K. Ueda, H. Ishizuka, M. Kriener, S. Kitou, D. Maryenko, M. Kawamura, T. Arima, M. Kawasaki, and Y. Tokura, Experimental Signatures of a Versatile Weyl Semimetal in a Pyrochlore Iridate with Spin-Ice-like Magnetic Orders, *Phys. Rev. B* **105**, L161102 (2022).

[6] H.-M. Guo and M. Franz, Three-dimensional Topological Insulators on the Pyrochlore Lattice, *Phys. Rev. Lett.* **103**, 206805 (2009).

[7] X. Wan, A. M. Turner, A. Vishwanath, and S. Y. Savrasov, Topological Semimetal and Fermi-Arc Surface States in the Electronic Structure of Pyrochlore Iridates, *Phys. Rev. B* **83**, 205101 (2011).

[8] D. Pesin and L. Balents, Mott Physics and Band Topology in Materials with Strong Spin–Orbit Interaction, *Nature Phys.* **6**, 376 (2010).

[9] H. Guo, C. Ritter, and A. C. Komarek, Magnetic Structure of $Tb_2Ir_2O_7$ Determined by Powder Neutron Diffraction, *Phys. Rev. B* **96**, 144415 (2017).

[10] H. Jacobsen, C.D. Dashwood, E. Lhotel, D. Khalyavin, P. Manuel, R. Stewart, D. Prabhakaran, D.F. McMorrow, and A.T. Boothroyd, Strong Quantum Fluctuations from Competition between Magnetic Phases in a Pyrochlore Iridate, *Phys. Rev. B* **101**, 104404 (2020).

[11] U. V. Valiev, J. B. Gruber, and G. W. Burdick, Magnetooptical Spectroscopy of the Rare-Earth Compounds: Development and Application, Scientific Research Publishing, Inc., pp. 9-35 (2012).

[12] E. U. Condon and G. H. Shortley, The Theory of Atomic Spectra, *Cambridge Univ. Press*, New York, 1935.

[13] K. Vlášková, P. Proschek, M. Diviš, D. Le, R. H. Colman, and M. Klicpera, Magnetic Properties and Crystal Field Splitting of the Rare-Earth Pyrochlore $Er_2Ir_2O_7$, *Phys. Rev. B* **102**, 054428 (2020).

[14] J. Jensen and A. R. Mackintosh, Rare Earth Magnetism: Structures and Excitations, *Oxford University Press* (1991).

[15] J. Song, G. Fabbris, W. Bi, D. Haskel, and J. S. Schilling, Pressure-Induced Superconductivity in Elemental Ytterbium Metal, *Phys. Rev. Lett.* **121**, 037004 (2018).

[16] W. Witczak-Krempa, G. Chen, Y. B. Kim, and L. Balents, Correlated Quantum Phenomena in the Strong Spin-Orbit Regime, *Annu. Rev. Condens. Matter Phys.* **5**, 57 (2014).

[17] M. Kotani, On the Magnetic Moment of Complex Ions. (I) *J. Phys. Soc. Jpn.* **4**, 293–297 (1949)

[18] Q. Zhao, F. Han, C. C. Stoumpos, T.-H. Han, H. Li, and J. F. Mitchell, New Insulating Antiferromagnetic Quaternary Iridates $MLa_{10}Ir_4O_{24}$ (M = Sr, Ba). *Sci. Rep.* **5**, 11705 (2015).

[19] M. C. Shapiro, S. C. Riggs, M. B. Stone, C. R. de la Cruz, S. Chi, A. A. Podlesnyak, and I. R. Fisher, Structure and Magnetic Properties of the Pyrochlore Iridate $Y_2Ir_2O_7$, *Phys. Rev. B* **85**, 214434 (2012).

[20] B. J. Kim, H. Jin, S. J. Moon, J.-Y. Kim, B.-G. Park, C. S. Leem, Jaejun Yu, T.W. Noh, C. Kim, S.-J. Oh, J.-H. Park, V. Durairaj, G. Cao, and E. Rotenberg, Novel J_{eff}=1/2 Mott State Induced by Relativistic Spin-Orbit Coupling in Sr_2IrO_4, *Phys. Rev. Lett.* **101**, 076402 (2008).

[21] S. J. Moon, H. Jin, K.W. Kim, W. S. Choi, Y. S. Lee, J. Yu, G. Cao, A. Sumi, H. Funakubo, C. Bernhard, and T.W. Noh, Dimensionality-Controlled Insulator-Metal Transition and Correlated Metallic State in 5*d* Transition Metal Oxides $Sr_{n+1}Ir_nO_{3n+1}$ (n = 1, 2, and ∞), *Phys. Rev. Lett.* **101**, 226402 (2008).

[22] S. Jia, S.-Y. Xu, and M. Z. Hasan, Weyl Semimetals, Fermi Arcs and Chiral Anomalies, *Nature Mater.* **15**, 1140 (2016).

[23] L. Balents, Spin Liquids in Frustrated Magnets, *Nature* **464**, 199 (2010).

[24] N. F. Mott, Conduction in Non-crystalline Materials, *J. Exp. Theor. Phys.* **19:160**, 835-852 (1969).

[25] A. L. Efros and B. I. Shklovskii, Coulomb Gap and Low Temperature Conductivity of Disordered Systems, *J. Phys. C: Solid State Phys.* **8**, L49 (1975).

[26] M. Imada, A. Fujimori, and Y. Tokura, Metal-Insulator Transitions, *Rev. Mod. Phys.* **70**, 1039 (1998).

[27] D. P. Arovas, E. Berg, S. A. Kivelson, and S. Raghu, The Hubbard Model, *Annu. Rev. Condens. Matter Phys.* **13**, 239 (2022).

[28] J. C. Slater, Magnetic Effects and the Hartree-Fock Equation, *Phys. Rev.* **82**, 538 (1951).

[29] Y. Feng, Y. Wang, D.M. Silevitch, S. E. Cooper, D. Mandrus, Patrick A. Lee, and T. F. Rosenbaum, A Continuous Metal-Insulator Transition Driven by Spin Correlations, *Nat. Commun.* **12**, 2779 (2021).

[30] S. Calder, V. O. Garlea, D. F. McMorrow, M. D. Lumsden, M. B. Stone, J. C. Lang, J.-W. Kim, J. A. Schlueter, Y. G. Shi, K. Yamaura, Y. S. Sun, Y. Tsujimoto, and A. D. Christianson, Magnetically Driven Metal-Insulator Transition in $NaOsO_3$, *Phys. Rev. Lett.* **108**, 257209 (2012).

[31] D. Mandrus, J. R. Thompson, R. Gaal, L. Forro, J. C. Bryan, B. C. Chakoumakos, L. M. Woods, B. C. Sales, R. S. Fishman, and V. Keppens, Continuous Metal-Insulator Transition in the Pyrochlore $Cd_2Os_2O_7$, *Phys. Rev. B* **63**, 195104 (2001).

[32] K. Matsuhira, M. Wakeshima, Y. Hinatsu, and S. Takagi, Metal–Insulator Transitions in Pyrochlore Oxides $Ln_2Ir_2O_7$, *J. Phys. Soc. Jpn.* **80** 094701 (2011).

[33] R. Arita, J. Kuneš, P. Augustinský, A. V. Kozhevnikov, A. G. Eguiluz, and M. Imada, Mott versus Slater-Type Metal-Insulator Transition in Sr_2IrO_4 and Ba_2IrO_4, *JPS Conf. Proc.* **3**, 013023 (2014).

[34] C. Martins, M. Aichhorn, L. Vaugier, and S. Biermann, Reduced Effective Spin-Orbital Degeneracy and Spin-Orbital Ordering in Paramagnetic Transition-Metal Oxides: Sr_2IrO_4 versus Sr_2RhO_4, *Phys. Rev. Lett.* **107**, 266404 (2011).

[35] J. Des Cloizeaux, Transition entre états métalliques et isolants pour un gaz d'électrons. Application aux Bandes d'Impuretés et aux Antiferromagnétiques, *J. Phys. Radium* **20**, 606 (1959).

[36] T. Sheahen, Rules for the Energy Gap and Critical Field of Superconductors, *Phys. Rev.* **149**, 368 (1966).

[37] D. P. Kozlenko, N. T. Dang, S. E. Kichanov, L. T. P. Thao, A. V. Rutkauskas, E. V. Lukin, B. N. Savenko, N. Tran, D. T. Khan, L. V. Truong-Son, L. H. Khiem, B. W. Lee, T. L. Phan, N. L. Phan, N. Truong-Tho, N. N. Hieu, T. A. Tran, and M. H. Phan, High Pressure Enhanced Magnetic Ordering and Magnetostructural Coupling in the Geometrically Frustrated Spinel Mn_3O_4, *Phys. Rev. B* **105**, 094430 (2022).

[38] D. Staško, J. Valenta, M. Kratochvílová, J. Prchal, P. Proschek, and M Klicpera, Pressure Induced Superconductivity in a $CeRhSi_3$ Single Crystal - the High Pressure Study, *J. Phys.: Condens. Matter* **33**, 035602 (2021).

[39] J. F. Nye, Physical Properties of Crystals, *Oxford University Press* (1957).

[40] M. Eremets, High Pressure Experimental Methods, *Oxford University Press* (1996).

[41] F. Murnaghan, Finite Deformations of an Elastic Solid, *Am. J. Math.* **59**, 235-260 (1937).

[42] F. Birch, Finite Elastic Strain of Cubic Crystals, *Phys. Rev.* **71**, 809-824 (1947).

[43] P. Vinet, J. Ferrante, J. R. Smith, and J. H. Rose, A Universal Equation of State for Solids, *J. Phys. C: Solid State Phys.* **19**, L467 (1986).

[44] R.G. Berman, Internally-consistent Thermodynamic Data for Minerals in the System Na_2O-K_2O-CaO-MgO-FeO-Fe_2O_3-Al_2O_3-SiO_2-TiO_2-H_2O-CO_2, *J. Petrol.* **29(2)**, 445-522 (1988).

[45] F. Sayetat, P. Fertey, and M. Kessler, An Easy Method for the Determination of Debye Temperature from Thermal Expansion Analyses, *J. Appl. Cryst.* **31**, 121-127 (1998).

[46] https://mgml.eu

[47] H. J. Scheel and T. Fukuda, Crystal Growth Technology, John Wiley and Sons Ltd, The Atrium, Southern Gate, Chichester (2003).

[48] V. Valvoda, M. Polcarová, and P. Lukáč, Základy Strukturní Analýzy, *Praha : Karolinum*, (1992).

[49] J. Rodríguez-Carvajal, Recent Advances in Magnetic Structure Determination by Neutron Powder Diffraction, *Phys. B: Condens. Matter* **192**, 55-69 (1993).

[50] A.A. Coelho, TOPAS and TOPAS-Academic: an Optimization Program Integrating Computer Algebra and Crystallographic Objects Written in C++, *J. Appl. Cryst.* **51**, 210-218 (2018).

[51] https://clip4.sourceforge.net

[52] CrysAlisPRO, Oxford Diffraction /Agilent Technologies UK Ltd, Yarnton, England.

[53] L. Palatinus and G. Chapuis, SUPERFLIP – a Computer Program for the Solution of Crystal Structures by Charge Flipping in Arbitrary Dimensions, *J. Appl. Cryst.* **40**, 786 (2007).

[54] V. Petříček, L. Palatinus, J. Plášil, and M. Dušek, Jana2020 - Jana2020 – a New Version of the Crystallographic Computing System Jana, *Z. Kristallogr. Cryst. Mater.* **238**(7-8), 271-282. (2023).

[55] M. Klicpera, K. Vlášková, and M. Diviš, Characterization and Magnetic Properties of Heavy Rare-Earth $A_2Ir_2O_7$ Pyrochlore Iridates, the Case of $Tm_2Ir_2O_7$, *J. Phys. Chem. C* **124**, 20367-20376 (2020).

[56] D. Staško, J. Prchal, M. Klicpera, S. Aoki, and K. Murata, Pressure Media for High Pressure Experiments, Daphne Oil 7000 series, *High Press. Res.* **40(4)**, 525-536 (2020).

[57] https://www.esrf.fr/home/UsersAndScience/support-and-infrastructure/support-labs/SampleEnvironment/high-pressure-laboratory/sess-hp-loan-pool-dacs.html

[58] A. Dewaele, M. Torrent, P. Loubeyre, and M. Mezouar, Compression Curves of Transition Metals in the Mbar Range: Experiments and Projector Augmented-Wave Calculations, *Phys. Rev. B* **78**, 104102 (2008).

[59] S. Klotz, J.-C. Chervin, P. Munsch, and G. Le Marchand, Hydrostatic Limits of 11 Pressure Transmitting Media, *J. Phys. D: Appl. Phys.* **42** 075413 (2009).

[60] D. M. Többens and S. Zander, KMC-2: an X-ray Beamline with Dedicated Diffraction and XAS Endstations at BESSY II, *JLSRF* **2**, A49 (2016).

[61] A. Fitch, C. Dejoie, E. Covacci, G. Confalonieri, O. Grendal, L. Claustre, P. Guillou, J. Kieffer, W. d. Nolf, S. Petitdemange, M. Ruat, and Y. Watier, ID22 – the High-resolution Powder-diffraction Beamline at ESRF, *J. Synchrotron Radiat.* **30**, 1003-1012 (2023).

[62] J.-L. Hodeau, P. Bordet, M. Anne, A. Prat, A. N. Fitch, E. Dooryhee, G. Vaughan, and A. Freund, Nine Crystal Multi-Analyser Stage For High-Resolution Powder Diffraction between 6 and 40 keV, *Proc. SPIE* **3448**, 353 (1998).

[63] M. Merlini and M. Hanfland, Single-Crystal Diffraction at Megabar Conditions by Synchrotron Radiation, *High Press. Res.* **33(3)**, 511-522 (2013).

[64] S. Anzellini, A. K. Kleppe, D. Daisenberger, M. T. Wharmby, R. Giampaoli, S. Boccato, M. A. Baron, F. Miozzi, D. S. Keeble, A. Ross, S. Gurney, J. Thompson, G. Knap, M. Booth, L. Hudson, D. Hawkins, M. J. Walter, and H. Wilhelm, Laser-Heating System for High-Pressure X-Ray Diffraction at the Extreme Conditions Beamline I15 at Diamond Light Source, *J. Synchrotron Radiat.* **25**, 1860-1868 (2018).

[65] C. Prescher and V.B. Prakapenka, DIOPTAS: a Program for Reduction of Two-Dimensional X-Ray Diffraction Data and Data Exploration, *High Press. Res.* **35:3**, 223–230 (2015).

[66] C. R. Wiebe and A. M. Hallas, Frustration under Pressure: Exotic Magnetism in New Pyrochlore Oxides, *APL Materials* **3**, 041519 (2015).

[67] K. Momma and F. Izumi, VESTA 3 for Three-Dimensional Visualization of Crystal, Volumetric and Morphology Data, *J. Appl. Crystallogr.* **44**, 1272-1276 (2011).

[68] J. Shamblin, M. Feygenson, J. Neuefeind, C. L. Tracy, F. Zhang, S. Finkeldei, D. Bosbach, H. Zhou, R. C. Ewing, and M. Lang, Probing Disorder in Isometric Pyrochlore and Related Complex Oxides, *Nature Mater.* **15**, 507 (2016).

[69] M. Das, S. Bhowal, J. Sannigrahi, A. Bandyopadhyay, A. Banerjee, G. Cibin, D. Khalyavin, N. Banerjee, D. Adroja, I. Dasgupta, and S. Majumdar, Interplay between Structural, Magnetic, and Electronic States in the Pyrochlore Iridate $Eu_2Ir_2O_7$, *Phys. Rev. B* **105**, 134421 (2022).

[70] Y. Tokiwa, J. J. Ishikawa, S. Nakatsuji, and P. Gegenwart, Quantum Criticality in a Metallic Spin Liquid, *Nature Mater.* **13**, 356-359 (2014).

[71] E. Lefrançois, V. Simonet, R. Ballou, E. Lhotel, A. Hadj-Azzem, S. Kodjikian, P. Lejay, P. Manuel, D. Khalyavin, and L.C. Chapon, Anisotropy-Tuned Magnetic Order in Pyrochlore Iridates, *Phys. Rev. Lett.* **114**, 247202 (2015).

[72] E. Lefrançois, V. Cathelin, E. Lhotel, J. Robert, P. Lejay, C. V. Colin, B. Canals, F. Damay, J. Ollivier, B. Fåk, L. C. Chapon, R. Ballou, and V. Simonet, Fragmentation in Spin Ice from Magnetic Charge Injection, *Nat. Commun.* **8**, 209 (2017).

[73] Y. Wang, T. F. Rosenbaum, D. Prabhakaran, A. T. Boothroyd, and Y. Feng, Approaching the Quantum Critical Point in a Highly Correlated All-in–All-out Antiferromagnet, *Phys. Rev. B* **101**, 220404(R) (2020).

[74] H. Guo, C. Ritter, and A. C. Komarek, Direct Determination of the Spin Structure Of $Nd_2Ir_2O_7$ by Means of Neutron Diffraction, *Phys. Rev. B* **94**, 161102(R) (2016).

[75] Rosalin, K. A. Irshad, B. Joseph, P. Telang, S. Singh, D. V. S. Muthu, and A. K. Sood, Pressure-Induced Phase Transition in Pyrochlore Iridates $(Sm_{1-x}Bi_x)_2Ir_2O_7$ (x = 0, 0.02, and 0.10): Raman and X-Ray Diffraction Studies, arXiv:2405.07607 (2024).

[76] K. Ueda, R. Kaneko, Subedi, M. Minola, B.J. Kim, J. Fujioka, Y. Tokura, and B. Keimer, Phonon Anomalies in Pyrochlore Iridates Studied by Raman Spectroscopy, *Phys. Rev. B* **100**, 115157 (2019).

[77] H.S. Rajeev, P. Telang, and S. Singh, One-shot Wet Chemical Synthesis and Physical Properties of Pyrochlore Iridates $A_2Ir_2O_7$, (A = Sm, Gd, Dy and Er), *Solid State Commun.* **312**, 113863 (2020).

[78] W. Liu, H. Han, L. Ma, L. Pi, L. Zhang, and Y. Zhang, Different Pressure Effects in $A_2Ir_2O_7$ (A =Gd, Eu, and Sm), *J. Alloys Compd.* **741**, 182–187 (2018).

[79] Y. Wu, M. Li, X. Li, and J. Xie, Evolution of Structural, Magnetic, and Electrical Transport Properties in Ru-doped Pyrochlore Iridate $Eu_2Ir_2O_7$, *J. Low Temp. Phys.* **202**, 48–58 (2021).

[80] A. Banerjee, J. Sannigrahi, S. Giri, and S. Majumdar, Observation of Non-Fermi Liquid Behaviour in Hole-Doped $Eu_2Ir_2O_7$, *Phys. Rev. B* **96**, 224426 (2017).

[81] J.J. Ishikawa, E.C.T. O'Farrell, and S. Nakatsuji, Continuous Transition between Antiferromagnetic Insulator and Paramagnetic Metal in the Pyrochlore Iridate $Eu_2Ir_2O_7$, *Phys. Rev. B* **85**, 245109 (2012).

[82] A.W. Sleight and A.P. Ramirez, Disappearance of the Metal-Insulator Transition in Iridate Pyrochlores on Approaching the Ideal $R_2Ir_2O_7$ Stoichiometry, *Solid State Commun.* **275**, 12–15 (2018).

[83] F. F. Tafti, J. J. Ishikawa, A. McCollam, S. Nakatsuji, and S. R. Julian, Pressure-Tuned Insulator to Metal Transition In $Eu_2Ir_2O_7$, *Phys. Rev. B* **85**, 205104 (2012).

[84] P. Telang, K. Mishra, G. Prando, A.K. Sood, and S. Singh, Anomalous Lattice Contraction and Emergent Electronic Phases in Bi-doped $Eu_2Ir_2O_7$, *Phys. Rev. B* **99**, 201112 (2019).

[85] M. Sakata, T. Kagayama, K. Shimizu, K. Matsuhira, S. Takagi, M. Wakeshima, and Y. Hinatsu, Suppression of Metal-Insulator Transition at High Pressure and

Pressure-Induced Magnetic Ordering in Pyrochlore Oxide $Nd_2Ir_2O_7$, *Phys. Rev. B* **83**, 041102(R) (2011).

[86] K. Ueda, J. Fujioka, C. Terakura, and Y. Tokura, Pressure and Magnetic Field Effects on Metal-Insulator Transitions of Bulk and Domain Wall States in Pyrochlore Iridates, *Phys. Rev. B* **92**, 121110(R) (2015).

[87] Z. Tian, Y. Kohama, T. Tomita, H. Ishizuka, T. H. Hsieh, J. J. Ishikawa, K. Kindo, L. Balents, and S. Nakatsuji, Field-Induced Quantum Metal–Insulator Transition in the Pyrochlore Iridate $Nd_2Ir_2O_7$, *Nature Phys.* **12**, 134 (2015).

[88] K. Ueda, J. Fujioka, Y. Takahashi, T. Suzuki, S. Ishiwata, Y. Taguchi, M. Kawasaki, and Y. Tokura, Anomalous Domain-Wall Conductance in Pyrochlore-Type $Nd_2Ir_2O_7$ on the Verge of the Metal-Insulator Transition, *Phys. Rev. B* **89**, 075127 (2014).

[89] M. J. Coak, K. Götze, T. Northam De La Fuente, C. Castelnovo, J. P. Tidey, J. Singleton, A. T. Boothroyd, D. Prabhakaran, and P. A. Goddard, Magnetotransport of $Sm_2Ir_2O_7$ across the Pressure-Induced Quantum-Critical Phase Boundary, *Npj Quantum Mater.* **9**:17 (2024).

[90] M. Ghosh, S. G. Bhat, A. Pal, and P. S. A. Kumar, Tuning the Semimetallic Charge Transport in the Weyl Semimetal Candidate $Eu_2Ir_2O_7$ (111) Epitaxial Thin Film with an All-in-All-out Spin Structure, *J. Phys.: Condens. Matter* **34**, 165701 (2022).

[91] T. C. Fujita, Y. Kozuka, M. Uchida, A. Tsukazaki, T. Arima, and M. Kawasaki, Odd-Parity Magnetoresistance in Pyrochlore Iridate Thin Films with Broken Time-Reversal Symmetry, *Sci. Rep.* **5**:9711 (2015).

[92] L. Xu, G. Gong, C. Zhao, X. Song, S. Yuan, and Z. Tian, Asymmetric Magnetization Reversal Behaviours Driven by Exchange Coupling between All-in-All-out Magnetic Domains and Domain Walls in a $Eu_2Ir_2O_7$ Single Crystal, *J. Phys. Chem. C* **124**, 22656 (2020).

[93] T. C. Fujita, M. Uchida, Y. Kozuka, W. Sano, A. Tsukazaki, T. Arima, and M. Kawasaki, All-in-All-out Magnetic Domain Wall Conduction in a Pyrochlore Iridate Heterointerface, *Phys. Rev. B* **93**, 064419 (2016).

[94] H. Sagayama, D. Uematsu, T. Arima, K. Sugimoto, J.J. Ishikawa, E. O'Farrell, and S. Nakatsuji, Determination of Long-Range All-In-All-Out Ordering of Ir^{4+} Moments in a Pyrochlore Iridate $Eu_2Ir_2O_7$ by Resonant X-Ray Diffraction, *Phys. Rev. B* **87**, 100403 (R) (2013).

[95] C. Donnerer, M. Rahn, M. Moretti Sala, J. Vale, D. Pincini, J. Strempfer, M. Krisch, D. Prabhakaran, A. Boothroyd, and D. McMorrow, All-In–All-Out Magnetic Order and Propagating Spin Waves in $Sm_2Ir_2O_7$, *Phys. Rev. Lett.* **117**, 037201 (2016).

[96] V. Cathelin, E. Lefrançois, J. Robert, P.C. Guruciaga, C. Paulsen, D. Prabhakaran, P. Lejay, F. Damay, J. Ollivier, B. Fåk, L.C. Chapon, R. Ballou, V. Simonet, P.C.W.

Holdsworth, and E. Lhotel, Fragmented Monopole Crystal, Dimer Entropy, and Coulomb Interactions in $Dy_2Ir_2O_7$, *Phys. Rev. Research* **2**, 032073(R) (2020).

[97] K. Vlášková, M. Diviš, and M. Klicpera, The Magnetic Behaviour of $Dy_2Ir_2O_7$ - Beyond the Mean Field Approximation, *J. Magn. Magn. Mater.* **538**, 168220 (2021).

[98] M. Klicpera, K. Vlášková, and M. Diviš, Low-Temperature Properties of Pyrochlore $Lu_2Ir_2O_7$, *J. Magn. Magn. Mater.* **506**, 166793 (2020).

[99] S. Ezairi, A. Elouafi, F. Lmai, and A. Tizliouine, Structural, Magnetic and Magnetocaloric Effect of Pyrochlore Iridate $Er_2Ir_2O_7$, *Phys. Scr.* **98**, 065803 (2023).

[100] W. C. Yang, W. K. Zhu, H. D. Zhou, L. Ling, E. S. Choi, M. Lee, Y. Losovyj, C.-K. Lu, and S. X. Zhang, Robust Pinning of Magnetic Moments in Pyrochlore Iridates, *Phys. Rev. B* **96**, 094437 (2017).

[101] N. Taira, M. Wakeshima, and Y. Hinatsu, Magnetic Properties of Iridium Pyrochlores $R_2Ir_2O_7$(R = Y, Sm, Eu and Lu), *J. Phys.: Condens. Matter* **13**, 5527 (2001).

[102] H. T. Hirose, J. Yamaura, and Z. Hiroi, Robust Ferromagnetism Carried by Antiferromagnetic Domain Walls, *Sci. Rep.* **7**:42440 (2017).

[103] W. Zhang, L. Li, P. Lu, M. Fan, Q. Su, F. Khatkhatay, A. Chen, Q. Jia, X. Zhang, J. L. MacManus-Driscoll, and H. Wang, Perpendicular Exchange-Biased Magnetotransport at the Vertical Heterointerfaces in $La_{0.7}Sr_{0.3}MnO_3$:NiO Nanocomposites, *ACS Appl. Mater. Interfaces* **7**, 21646 (2015).

[104] J. Wu, J. S. Park, W. Kim, E. Arenholz, M. Liberati, A. Scholl, Y. Z. Wu, C. Hwang, and Z. Q. Qiu, Direct Measurement of Rotatable and Frozen CoO Spins in Exchange Bias System Of CoO/Fe/Ag(001), *Phys. Rev. Lett.* **104**, 217204 (2010).

[105] T. Arima, Time-Reversal Symmetry Breaking and Consequent Physical Responses Induced by All-In-All-Out Type Magnetic Order on the Pyrochlore Lattice, *J. Phys. Soc. Jpn.* **82**, 013705 (2013).

[106] E. Y. Ma, Y.-T. Cui, K. Ueda, S. Tang, K. Chen, N. Tamura, P. M. Wu, J. Fujioka, Y. Tokura, and Z.-X. Shen, Mobile Metallic Domain Walls in an All-in-All-out Magnetic Insulator, *Science* **350**, 538 (2015).

[107] S. Tardif, S. Takeshita, H. Ohsumi, J. Yamaura, D. Okuyama, Z. Hiroi, M. Takata, and T. Arima, All-In–All-Out Magnetic Domains: X-Ray Diffraction Imaging and Magnetic Field Control, *Phys. Rev. Lett.* **114**, 147205 (2015).

[108] T. C. Fujita, M. Uchida, Y. Kozuka, S. Ogawa, A. Tsukazaki, T. Arima, and M. Kawasaki, All-in-All-out Magnetic Domain Size in Pyrochlore Iridate Thin Films as Probed by Local Magnetotransport, *Appl. Phys. Lett.* **108**, 022402 (2016).

[109] K. Vlášková, R. H. Colman, and M. Klicpera, Synthesis of $Er_2Ir_2O_7$ Pyrochlore Iridate by Solid-State-Reaction and CsCl Flux Method, *Mater. Chem. Phys.* **258**, 123868 (2021).

[110] D. Staško, K. Vlášková, P. Proschek, and M. Klicpera; Conductive Properties of Heavy-Rare-Earth $A_2Ir_2O_7$ Iridates Synthesized by the CsCl-flux Method; *J. Phys. Chem. Solids* **176**, 111268 (2023).

[111] D. Staško, F. Hájek, K. Vlášková, J. Kaštil, M. Henriques, and M. Klicpera, Robust Pinned Magnetisation in $A_2Ir_2O_7$ Iridates, the Case of $Er_2Ir_2O_7$ and $Lu_2Ir_2O_7$ Flux-Grown Single Crystals, *Sci. Rep.* **14**, 21773 (2024).

[112] Y. Shirako, X. Wang, Y. Tsujimoto, K. Tanaka, Y. Guo, Y. Matsushita, Y. Nemoto, Y. Katsuya, Y. Shi, D. Mori, H. Kojitani, K. Yamaura, Y. Inaguma, and M. Akaogi, Synthesis, Crystal Structure, and Electronic Properties of High-Pressure PdF2-Type Oxides MO_2 (M = Ru, Rh, Os, Ir, Pt), *Inorg. Chem.* **53**, 11616 (2014).

[113] O. Greis, R. Ziel, B. Breidenstein, A. Haase, and T. Petzel, The Crystal Structure of the Low-Temperature A-Type Modification of Pr_2O_3 from X-Ray Powder and Electron Single Crystal Diffraction, *J. Alloys Compd.* **216**, 255 (1995).

[114] A. Pavlik III, S. V. Ushakov, A. Navrotsky, C. J. Benmore, and R. J. K. Weber, Structure and Thermal Expansion of Lu_2O_3 and Yb_2O_3 up to the Melting Points, *J. Nucl. Mater.* **495**, 385 (2017).

[115] A. di Biase, C. Castellano, G. Confalonieri, P. Fumagalli, S. Tumiati, D. Ceresoli, and M. Scavini, Emerging Disorder in $Gd_2(Ti_{1-x}Zr_x)_2O_7$ Pyrochlores Matrices for Radioactive Waste Disposal: Symmetry Lowering versus Defect Clustering, *J. Mater. Chem. A* **11**, 24203 (2023).

[116] W. I. F. David, M. O. Jones, D. H. Gregory, C. M. Jewell, S. R. Johnson, A. Walton, and P. P. Edwards, A Mechanism for Non-Stoichiometry in the Lithium Amide/Lithium Imide Hydrogen Storage Reaction, *J. Am. Chem. Soc.* **129**, 1594 (2007).

[117] D. Staško, K. Vlášková, A. Kancko, D. M. Többens, D. Daisenberger, G. Garbarino, R. H. Colman, and M. Klicpera, Robustness of the Pyrochlore Structure in Rare-Earth $A_2Ir_2O_7$ Iridates and Pressure-Induced Structural Transformation in IrO_2, *Ceram. Int.* **50**, 35657 (2024).

[118] M. Klicpera, K. Vlášková, D. Staško, T. Guidi, I. Puente Orench, and M. Diviš, Neutron Scattering Study of the $Tm_2Ir_2O_7$ Pyrochlore Iridate, *Phys. Rev. B* **106**, 094408 (2022).

[119] B.S. Hulbert, S.J. McCormack, K.-P. Tseng, and W.M. Kriven, Thermal Expansion and Phase Transformation in the Rare Earth Di-titanate ($R_2Ti_2O_7$) System, *Acta Crystallogr. B* **77**, 397 (2021).

[120] J.M. Farmer, L.A. Boatner, B.C. Chakoumakos, M.-H. Du, M.J. Lance, C.J. Rawn, and J.C. Bryan, Structural and Crystal Chemical Properties of Rare-Earth Titanate Pyrochlores, *J. Alloys Compd.* **605,** 63 (2014).

[121] J.P. Clancy, H. Gretarsson, E.K.H. Lee, D. Tian, J. Kim, M.H. Upton, D. Casa, T. Gog, Z. Islam, B.-G. Jeon, K.H. Kim, S. Desgreniers, Y.B. Kim, S.J. Julian, and

Y.- J. Kim, X-ray Scattering Study of Pyrochlore Iridates: Crystal Structure, Electronic, and Magnetic Excitations, *Phys. Rev. B* **94,** 024408 (2016).

[122] H. Li, N. Li, Y. Li, Q. Tao, Y. Zhao, H. Zhu, Y. Ma, P. Zhu, and X. Wang, Pressure-Induced Disordering and Phase Transformations in $Eu_2Zr_2O_7$ Pyrochlore, *High Press. Res.* **37**, 256 (2017).

[123] A. Thomas, P. Telang, D. Rout, K. Mishra, A. Pal, D. V. S. Muthu, P. S. A. Kumar, S. Singh, and A. K. Sood, Anomalous Pressure Dependence of Phonon Line Widths in Metallic Pyrochlore Iridates $(Eu_{1-x}Bi_x)_2Ir_2O_7$: Crossover from Incoherent to Coherent Metal, *Pramana – J. Phys.* **97**, 138 (2023).

[124] B. Zohuri, Physics of Cryogenics, 494 (chapter 15) (2018).

[125] J.N. Millican, R.T. Macaluso, S. Nakatsuji, Y. Machida, Y. Maeno, and J.Y. Chan, Crystal Growth and Structure of $R_2Ir_2O_7$ (R = Pr, Eu) Using Molten KF, *Mater. Res. Bull.* **42,** 928–934 (2007).

[126] S. M. Disseler, C. Dhital, A. Amato, S. R. Giblin, C. de la Cruz, S. D. Wilson, and M. J. Graf, Magnetic Order in the Pyrochlore Iridates $A_2Ir_2O_7$ (A = Y, Yb), *Phys. Rev. B* **86**, 014428 (2012).

[127] D. Kumar, S. Y. Chen, M. K. Lee, C. M. N. Kumar, R. Aldus, and L. J. Chang, Low Temperature Magnetic Properties of Frustrated Pyrochlore Ferromagnet $Ho_2Ir_2O_7$, *J. Phys.: Conf. Ser.* **828**, 012008 (2017).

[128] Ya. I. Rodionov and S. V. Syzranov, Conductivity of a Weyl Semimetal with Donor and Acceptor Impurities, *Phys. Rev. B* **91**, 195107 (2015).

[129] P. G. LaBarre, L. Dong, J. Trinh, T. Siegrist, and A. P. Ramirez, Evidence for Undoped Weyl Semimetal Charge Transport in $Y_2Ir_2O_7$, *J. Phys.: Condens. Matter* **32**, 02LT01 (2019).

[130] D. Staško, P. Proschek, J. Prchal, and M. Klicpera, Pressure-Tuned Magnetism and Conductivity in Pyrochlore Iridates $Lu_2Ir_2O_7$ and $Er_2Ir_2O_7$, arXiv:2408.01278 (2024).

[131] Z. Hiroi, J. Yamaura, T. Hirose, I. Nagashima, and Y. Okamoto. Lifshitz Metal–Insulator Transition Induced by the All-In/All-Out Magnetic Order in the Pyrochlore Oxide $Cd_2Os_2O_7$, *APL Mater.* **3**, 041501 (2015).

[132] M. Nakayama, Takeshi Kondo, Z. Tian, J. J. Ishikawa, M. Halim, C. Bareille, W. Malaeb, K. Kuroda, T. Tomita, S. Ideta, K. Tanaka, M. Matsunami, S. Kimura, N. Inami, K. Ono, H. Kumigashira, L. Balents, S. Nakatsuji, and S. Shin, Slater to Mott Crossover in the Metal to Insulator Transition of $Nd_2Ir_2O_7$, *Phys. Rev. Lett.* **117**, 056403 (2016).

[133] E. Zoghlin, Z. Porter, S. Britner, S. Husremovic, Y. Choi, D. Haskel, G. Laurita, and S. D. Wilson, Mapping the Structural, Magnetic and Electronic Behavior of $(Eu_{1-x}Ca_x)_2Ir_2O_7$ Across a Metal–Insulator Transition, *J. Phys.: Condens. Matter* **33**, 055601 (2020).

[134] G. Prando, R. Dally, W. Schottenhamel, Z. Guguchia, S.-H. Baek, R. Aeschlimann, A. U. B. Wolter, S. D. Wilson, B. Büchner, and M. J. Graf, Influence of Hydrostatic Pressure on the Bulk Magnetic Properties of $Eu_2Ir_2O_7$, *Phys. Rev. B* **93**, 104422 (2016).

[135] H. Shinaoka, S. Hoshino, M. Troyer, and P. Werner, Phase Diagram of Pyrochlore Iridates: All-in–All-out Magnetic Ordering and Non-Fermi-Liquid Properties, *Phys. Rev. Lett.* **115**, 156401 (2015).

[136] S. Mondal, M. Modak, B. Maji, S. K. Mandal, B. Ghosh, S. Saha, M. Sardar, and S. Banerjee, Evolution of Magnetic and Transport Properties in the Cu-Doped Pyrochlore Iridate $Eu_2(Ir_{1-x}Cu_x)_2O_7$, *Phys. Rev. B* **105**, 155113 (2022).

[137] W. K. Zhu, M. Wang, B. Seradjeh, F. Yang, and S. X. Zhang, Enhanced Weak Ferromagnetism and Conductivity in Hole-Doped Pyrochlore Iridate $Y_2Ir_2O_7$, *Phys. Rev. B* **90**, 054419 (2014).

List of Figures

List of Tables

List of Abbreviations

AC – alternating current
AFM – antiferromagnetic
AIAO – all-in-all-out
AOAI – all-out-all-in
BSE – backscattered electron
CCR – close-cycle refrigerator
CLIP – Cologne Laue Indexation Program
CEF – crystal electric field
DC – direct current
DW – domain wall
EDX – energy dispersive X-ray analysis
EoS – equation of state
ESRF – European Synchrotron Radiation Facility
FC – field-cooled
FM – ferromagnetic
FWHM – full width at half maximum
MGML – Materials Growth & Measurement Laboratory
MPMS – magnetic property measurement system
MR – magnetoresistivity
PPMS – physical property measurement system
RIXS – resonant inelastic X-ray scattering
RSO – reciprocating sample option
RXD – resonant X-ray diffraction
SE – secondary electrons
SEM – scanning electron microscope
SOC – spin-orbit coupling
SQUID – superconducting quantum interference device
TSCI – thermally screened charged impurities
VRH – variable-range hopping
XPS – X-ray photoelectron spectroscopy
XRD – X-ray diffraction
XRF – X-ray fluorescence
ZFC – zero-field-cooled

List of publications

The following list contains publications tied to the theme of the presented thesis. That is, only publications related to the $A_2B_2O_7$ oxides are included. Other publications (three as main author and two as co-author) can be found at the Web of Science portal.

1. D. Staško, P. Proschek, J. Prchal, and M. Klicpera, Pressure-Tuned Magnetism and Conductivity in Pyrochlore Iridates $Lu_2Ir_2O_7$ and $Er_2Ir_2O_7$, arXiv:2408.01278 (2024).
2. D. Staško, F. Hájek, K. Vlášková, J. Kaštil, M. Henriques, and M. Klicpera, Robust Pinned Magnetisation in $A_2Ir_2O_7$ Iridates, the Case of $Er_2Ir_2O_7$ and $Lu_2Ir_2O_7$ Flux-Grown Single Crystals, *Sci. Rep.* **14**, 21773 (2024).
3. D. Staško, K. Vlášková, A. Kancko, D. M. Többens, D. Daisenberger, G. Garbarino, R. H. Colman, and M. Klicpera, Robustness of the Pyrochlore Structure in Rare-Earth $A_2Ir_2O_7$ Iridates and Pressure-Induced Structural Transformation in IrO_2, *Ceram. Int.* **50**, 35657 (2024).
4. D. Staško, K. Vlášková, D. Vojtasová, F. Hájek, P. Král, R.H. Colman, and M. Klicpera, The Synthesis of the Rare Earth $A_2Zr_2O_7$ Single Crystals by Simplified Laser-Heated Floating Hot Zone and Pedestal Methods, *Mater. Today Chem.* **39**, 102153 (2024).
5. D. Vojtasova, D. Staško, F. Hájek, R. H. Colman, and M. Klicpera, Low-Temperature Properties of Magnetically Frustrated Rare-Earth Zirconates $A_2Zr_2O_7$, *J. Phys.: Condens. Matter* **36** 325805 (2024).
6. M. Klicpera, D. Staško, K. Vlášková, F. Hájek, D. Vojtasová, J. Zelenka, and R.H. Colman, Magnetic Frustration in Rare-Earth Zirconates $A_2Zr_2O_7$, the Case of Laser Heated Pedestal Method Synthesised A = Er, Tm, Yb, and Lu Single Crystals, *J. Alloys Compd.* **978**, 173440 (2024).
7. D. Staško, K. Vlášková, P. Proschek, and M. Klicpera, Conductive Properties of Heavy-Rare-Earth $A_2Ir_2O_7$ Iridates Synthesized by the CsCl-Flux Method, *J. Phys. Chem. Solids* **176**, 111268 (2023).
8. M. Klicpera, K. Vlášková, D. Staško, T. Guidi, I. Puente Orench, and M. Diviš, Neutron Scattering Study of the $Tm_2Ir_2O_7$ Pyrochlore Iridate, *Phys. Rev. B* **106**, 094408 (2022).